

High compositional resolution characterization of multi-component macromolecular systems

Submitted in partial fulfillment of the requirements for
the degree of:

Doctor of Philosophy

in

Chemical Engineering

Deyu Yang

B.S., Chemical Engineering, The Pennsylvania State University

Carnegie Mellon University

Pittsburgh, PA

April 2022

© [Deyu Yang], 2022

All Rights Reserved

Acknowledgments

“It’s not who you are that holds you back, it’s who you think you’re not”.

-- Denis Waitley

Still can’t believe that the five years of my Ph.D. life almost reaches an end. It has been a challenging but invaluable experience for me. The meaning of these five years to me is hard to be described. It provides me the second opportunity to know, accept and embrace myself. Besides the knowledge that I’ve gained through this journey, the confidence that I gained gives me the courage to face the challenges in the future of my life.

I would first like to thank my advisor, Prof. Lynn Walker. I am very grateful to have an advisor who has continuously provided guidance over the past five years. She not only provides incredible mentorship for my academic research but always provides strong support when I am encountering problems. Under her guidance, I have become an independent researcher and have the skills and confidence to approach more challenging problems. I would like to thank Prof. Kelly Schultz and Dr. Maryam Daviran for their kind support and collaboration on microrheology analysis in this work. I would like to thank all my colleagues and friends in and outside the chemical engineering department for helping me in my research work and my life. It was great to have you all go on this five-year journey. I’d also like to thank my thesis committee, Prof. Shelley Anna, Prof. Frederick Lanni, and Prof. Anne Robinson for their feedback and continuous support on this thesis. In addition,

I gratefully acknowledge the Department of Chemical Engineering at CMU for the funding of this thesis work.

I would like to thank my parents and my sister. Thank you all for your encouragement and support, which means everything to me. I love you all. Dad and mom, thank you so much for providing me with this opportunity to achieve my goal. Zaowa, thank you for being the one that always gives me the sweetest smile through the video when I am depressed. Finally, I'd like to express my appreciation to my boyfriend, Johnny. Thank you for making the decision to move to Pittsburgh and accompany me through my Ph.D. journey. I don't know if I could have done this without you. Thank you for being the one that always got my back.

Abstract

Biopharmaceutical proteins have attracted increasing interest and been developed for treatment of various diseases due to their low toxicity, high affinity, and high efficacy. Subcutaneous injection, the most common delivery route for therapeutic proteins, requires high protein concentration formulations due to limited injection volume, resulting in challenges in manufacture, delivery, and stability of the drug products. Limited availability hinders the effective characterization of the physical properties of therapeutic proteins, especially during the early stage of development, where a large number of candidate formulations across a huge compositional space need to be screened. In this thesis, a droplet-based microfluidic device is innovated by incorporating a variety of sensing methods to quantify different physical properties of the concentrated protein solutions accurately and efficiently over a wide range of process-relevant parameters. Multiple particle tracking microrheology, birefringence, and turbidity are applied as the sensing methods to investigate viscosity, crystalline phase transitions, and phase separation of the protein solutions, respectively. The microfluidic technique provides data with high compositional resolution, and only requires a small sample volume. This work has demonstrated the potential of the developed novel technique to rapidly screen candidate formulations and provide guidance to facilitate the design of protein formulations to achieve desired properties. This technique can also be potentially applied as a complementary approach for computational methods to predict behaviors of high concentration formulations and facilitate understanding of the underlying mechanisms.

Table of Contents

Chapter 1. Introduction	1
Chapter 2. Materials and Methods	6
2.1 Materials	6
2.2 Fabrication of microfluidic device	6
2.3 Droplet generation and concentration measurements in shrinking Droplets	7
2.4 Multiple particle tracking microrheology	11
2.5 Microscopy	15
2.6 Reference	17
Chapter 3. Droplet-based microfluidic tool to quantify viscosity of concentrating protein solutions	18
3.1 Introduction	18
3.2 Materials and Methods	21
3.2.1 Materials	21
3.2.2 Microscopy	21
3.2.3 Multiple particle tracking microrheology	22
3.2.4 Validation of MPT and results obtained in the microfluidic device	22
3.3 Approach	23
3.3.1 Concentration measured in shrinking droplets	23
3.3.2 Concentration-dependence of viscosity measured in shrinking droplets	24
3.3.3 Design space of the device	27
3.4 Results	29
3.4.1 Validation of MPT in a glass sample chamber	29
3.4.2 Validation of MPT in microfluidic droplets	31
3.4.3 Viscosity measurements of PEG in shrinking droplets	33
3.4.4 Viscosity measurements of proteins in shrinking droplets	35
3.5 Discussion	38
3.6 Conclusions	40
3.7 Reference	42

Chapter 4: Systematic quantification of the effects of pH and ionic strength on the viscosity of highly concentrated BSA solutions	46
4.1 Introduction	46
4.2 Materials and Methods	49
4.2.1 Materials	49
4.2.2 Preparation of BSA solutions.....	49
4.2.3 Quantification of viscosity vs. concentration of BSA solutions in the microfluidic device	50
4.2.4 Microscopy	51
4.2.5 Zeta potential measurements.....	51
4.3 Results and Discussions	52
4.4 Conclusions	61
4.5 Reference.....	63
Chapter 5: Synergistic effects of multiple excipients on reducing viscosity of concentrated antibody solutions.....	66
5.1 Introduction	66
5.2 Materials and methods	67
5.2.1 Materials	67
5.2.2 Preparation of BGG solutions.....	68
5.2.3 Approach for measuring protein solution viscosity vs. concentration	69
5.2.4 Measurements of initial protein concentrations.....	70
5.3 Results	71
5.4 Discussion	80
5.5 Conclusions	83
5.6 Reference.....	84
Chapter 6: Quantifying the effects of additives on the phase transition of lyotropic liquid crystals with high composition resolution	87
6.1 Introduction	87
6.1.1 Lyotropic Chromonic Liquid Crystals (LCLCs).....	88
6.2 Materials and Methods	90
6.2.1 Materials	90

6.2.2	Microfluidic shrinking droplets	91
6.2.3	Theory of Gray-Level Co-Occurrence Matrix	94
6.3	Results and Discussions	95
6.3.1	Observation of birefringence in the microfluidic device	95
6.3.2	Macroscopic experiments	97
6.3.3	Quantification of colloidal effects on the I to I+N transition	98
6.3.4	Potential of image analysis for identification of phase transitions	106
6.4	Conclusions:	118
6.5	Reference.....	119
Chapter 7: Quantification of phase separation of a globular protein induced by polyethylene glycol		124
7.1	Introduction	124
7.2	Materials and Methods	126
7.2.1	Materials	126
7.2.2	Methods.....	127
7.3	Results	128
7.4	Discussion	135
7.5	Conclusions	137
7.6	Reference.....	138
Chapter 8: Conclusions		141

List of Figures

- Figure 2.1** Top view of the microfluidic device and a droplet trap (top). Schematic of the side view of the device (bottom) shows that water slowly diffuses out the droplet and concentration increases. The grayscale image on the top left indicates the produced 40 droplets. 8
- Figure 2.2** Measured droplet diameter and calculated solute concentration as a function of time for a typical droplet. 10
- Figure 2.3** MSD for 84wt% glycerol at 40 fps with various exposure time. Subdiffusion and superdiffusion are observed as the exposure time increase from 5 ms to 20ms, especially at short lag time. $\sigma = 10$ ms provides diffusive motion... 15
- Figure 3.1** Viscosities are measured along the increasing concentration in shrinking droplets. a) Droplet diameters are tracked as a function of time for all 40 drops by scanning the device in the zig-zag direction (shown by the inset) every 1 or 2 hours. The corresponding solute concentrations are shown as the filled blue triangles. Viscosities are measured during the dehydration process. The corresponding solute concentrations calculated based on the linear-extrapolated diameter are represented by the red crosses. Each cluster represents one viscosity scan, which takes approximately 40 min. b) The variation in solute concentration (red crosses) and viscosity (green squares) as a function of drop position during one viscosity scan. c) Viscosity as a function of concentration with high composition resolution by replotting data provided in b)..... 25
- Figure 3.2** Unity plot of viscosities measured by multiple particle tracking (MPT) versus viscosities measured by viscometer of glycerol solutions at varying concentrations. The diagonal dotted line represents slope of 1. The filled orange triangles and blue circles represent results using 0.26 μm and 0.50 μm probes for MPT respectively. The inset shows the mean-squared displacement curves for 1 μm probe particles for glycerol at various concentrations. 29
- Figure 3.3** Unity plot of viscosities measured inside the droplets versus viscosities measured in the glass chamber for glycerol (blue circles), BSA (red triangles), and lysozyme (green squares) at varying concentrations. The diagonal dashed line represents a slope of 1 and the two dotted lines represent $\pm 10\%$ deviation. The open and filled symbols represent measurements in the droplet taken at initial loading and results obtained from the shrinking droplets, respectively..... 32
- Figure 3.4** Viscosity of concentrating 4 kg/mol (filled squares) and 100 kg/mol (filled triangles) PEG solutions are quantified inside shrinking droplets using MPT. For 100 kg/mol PEG, two devices (red and yellow filled triangles) are used with loading concentrations indicated by the arrows. The black crosses are bulk measurements for 100 kg/mol PEG. The open symbols indicate results obtained from Natalia et al. (2011). Each symbol represents a specific molecular weight. The

top two dotted lines show the microrheology resolution for 0.26 μm and 0.50 μm probes, respectively..... 33

Figure 3.5 Concentration-dependence of viscosity for BSA (circles) and lysozyme (diamonds) are quantified in the microfluidic device. For each protein, multiple devices are used to cover the entire concentration range from 50 to 400 mg/ml. Each color represents one device, with the loading concentration indicated by the arrow. The two bold dotted lines represent the best-fit to the Krieger-Dougherty model for each protein. The top two dotted lines show the microrheology resolution for 0.26 μm and 0.50 μm probes, respectively..... 35

Figure 4.1 The viscosity of BSA solution as a function of BSA concentration at pH 6.6 (a), pH 5.0 (b) and pH 3.9 (c) with various ionic strengths. Each symbol represents a constant ratio of ionic strength to BSA concentration, ξ . The circles, squares, diamonds, triangles, and inverted triangles represent ξ of 0, 0.06, 0.3, 0.6, and 0.8, respectively. 53

Figure 4.2 Viscosity of BSA solution as a function BSA concentration and ionic strength at pH 6.6. The shaded area represents the surface plot generated based on the three data sets. The shaded rectangle in a) shows the plane cut of constant BSA concentration at 350 mg/mL, and in b) shows the plane cut of constant viscosity of 50cP. The red dotted line represents a) iso-concentration line and b) iso-viscosity line, which are drawn to guide the eyes. 54

Figure 4.3 Viscosity of BSA as a function of ionic strength at pH 6.6 (red circles), 5.0 (blue diamonds), and 3.9 (green squares) at 350 mg/mL obtained from the plane cuts of constant BSA concentration. The dotted lines represent iso-concentration lines and are drawn to guide the eyes. 56

Figure 4.4 Concentration of BSA as a function of ionic strength at pH 6.6 (red circles), 5.0 (blue diamonds) , and 3.9 (green squares) at 50 cP obtained from the plane cuts of constant viscosity. The dotted lines represent iso-viscosity lines and are drawn to guide the eyes..... 57

Figure 4.5 Zeta potential of BSA solution as a function of pH at 15mM ionic strength..... 58

Figure 4.6 Viscosity of BSA as a function of BSA concentration at pH 5.0 (diamonds) and pH 3.9 (squares) with ξ of 0.8. The filled and open symbols represent the BSA solution with and without caffeine, respectively. BSA is in the stable heart-like N-form and partially expanded F-form at pH 5.0 and 3.9, respectively. 61

Figure 5.1 Concentration dependence of viscosity for BGG solutions at pH 7 (a) and pH 10 (b). Circles represent the control case with no additives. Squares, diamonds and triangles represent BGG with ArgHCl, caffeine and with both ArgHCl and caffeine, respectively. Each symbol represent one droplet dehydration experiment with a constant value of ξ 71

Figure 5.2 Viscosity of BGG as a function of BGG concentration and ξ at pH 7 (a) and pH 10 (b). Different types of symbols represent the excipients same as denoted in Figure 5.1. The light green shaded area represents the surface plot generated based on the continuous data points. The shaded rectangle indicates the plane cut at the BGG concentration of 280 mg/mL as an example and the dashed red line shows the iso-concentration line, which is drawn to guide the eyes.	73
Figure 5.3 Viscosity of BGG versus type of excipients at BGG concentrations of 280 mg/mL (orange), 330 mg/mL (gray) and 340 mg/mL (yellow) at pH 7 (a) and pH 10 (b).	74
Figure 5.4 The degree of change in viscosity as a function of BGG concentration at pH 7 (a) and pH 10 (b). Squares, diamonds and triangles represent ArgHCl, caffeine, and ArgHCl with caffeine, respectively.	75
Figure 5.5 Viscosity of BGG as a function of BGG concentration and ξ at pH 7 (a) and pH 10 (b). Different types of symbols represent the additives same as denoted in Figure 5.1. The light green shaded area represents the surface plot generated based on the continuous data points. The shaded rectangle indicates the plane cut at 50 cP. The dashed red line shows the iso-viscosity line, which is drawn to guide the eyes.	76
Figure 5.6 BGG concentration versus type of excipients at a constant viscosity of 50 cP for pH 7 (crossed blue) and pH 10 (green).	77
Figure 5.7 Viscosity-concentration curves for BGG with ArgHCl (squares) and both ArgHCl and caffeine (triangles) at pH 7, which are fitted to the exponential function of $\eta = a \exp(bC)$ represented by the solid lines, where C is the BGG concentration in mg/mL, η is viscosity, and a and b are the fitted parameters. The red circle indicates the deviation from the exponential function at low BGG concentrations.	79
Figure 6.1 Chemical structure of SSY.	91
Figure 6.2 a) and b) show the measured droplet diameter and calculated SSY concentration, respectively, for a typical droplet. The dotted red line represent the linear fit. Gray shaded area indicate the measurements with less confidence due to the deviation from the pancake shape.	93
Figure 6.3 Representative dehydration process of a droplet containing dilute sunset yellow aqueous solution captured under the polarizing microscope with polarizers crossed in the microfluidic device. Dashed circles outline the representative droplet for clarity. White bars are equivalent to 200 μm . The occurrence of the bright spots, shown as the second image, indicates the onset of isotropic (I) to isotropic + nematic (I+N).	96
Figure 6.4 Schematic of macroscopic experiment. SSY at various concentrations are loaded into the 1mm capillary tubes, which ends are sealed with epoxy glue to	

prevent water evaporation. The tubes are observed under the crossed-polarized microscope. A clear visual difference is observed for samples that are isotropic and birefringent, which appear to be dark and tinted red, respectively. 98

Figure 6.5 $CI + N$ as a function of molar ratio of salt to SSY for two types of salts: NaCl and $MgCl_2$, which are represented by the circles and squares, respectively. The triangle on the left axis represents $CI + N$ without salts. The dotted lines are drawn to guide the eyes. The inset illustrates $CI + N$ as a function of Debye length. The arrow indicates the increase in the salt concentration. 100

Figure 6.6 Phase diagram of SSY, PEG and water mixtures established via the microfluidic experiments. The filled squares, circles, and diamonds represent the solute concentrations at phase transition for 600 g/mol, 4000 g/mol, and 10000 g/mol PEG, respectively. Each dotted black line represents one droplet shrinking experiment and the slope indicates a constant molar ratio (ξ) of SSY to PEG. Open circles indicate the initial solute concentrations for SSY with 4000 g/mol PEG. The colored shaded areas represent the concentration intervals where phase transitions occur obtained from Park H.S. *et al* (2011). The insets shows the phase transition concentration, $CI + N$, as a function of $MW^{1/2}$ of PEG for ξ of 27 (squares) and 43 (circles). 101

Figure 6.7 Phase diagram of SSY with Ludox-AM (squares) and SSY with Ludox-TMA (circles) at various molar ratios of SSY to Ludox (ξ). The vertical dashed line and the bold dashed line represent the boundaries for I to I+N phase transition and gelation, respectively. The dotted dashed line separates the ξ with or without gelation, which is drawn to guide eyes. Image 1-3 show a geled droplet, a geled droplet at I to I+N phase and a droplet at I+N phase without gelation, respectively. 105

Figure 6.8 Dehydration sequence of a typical droplet containing SSY solution with Ludox-AM (top row) and Ludox-TMA (bottom row) at $\xi = 30$. The dashed lines outline the droplets for clarity. White bars are equivalent to 200 μm 106

Figure 6.9 Optical textures of SSY, SSY/ salts, and SSY/ PEG with various ξ during the dehydration process for a representative droplet. Dotted lines outline the droplets for clarity. The arrow points in the direction of increasing time and solute concentrations. 108

Figure 6.10 Computed parameters from the textures of pure SSY as a function of SSY concentration. The asterisks indicate the concentrations for phase transitions identified by image analysis. The 5 vertical dotted lines show the phase transitions identified by human eye. The corresponding polarizing images are indicated as inset A-E, respectively. 110

Figure 6.11 Computed parameters from the textures of pure SSY as a function of SSY concentration for 26 droplets. The asterisks indicate the concentrations for phase transitions identified by image analysis. Inset indicates the distribution of

peak concentrations between SSY concentrations of 0.9 to 1.3M as highlighted by the dashed rectangles. 112

Figure 6.12 Computed statistical parameters from the textures for SSY with PEG: a) $\xi = 43$, b) $\xi = 6$. In b), the insets illustrate the zoom in of the circled regions. Image 1-3 show the transition of PEG crystallization, which induces the change in the magnitude of all five parameter at approximately 0.68M to 0.70M. 116

Figure 7.1 A typical dehydration process of a droplet containing dilute BSA with PEG obtained through the bright field microscope in the microfluidic device. White bars are equivalent to 200 μm . The droplet shrinks in size and the concentration of solute increases. The first observation of the occurrence of turbidity (image 2) indicates the onset of transition. Turbidity increases through the shrinking process. 128

Figure 7.2 Ratio of I_{center} to $I_{\text{background}}$ as a function of BSA concentration for BSA with 1500 g/mol PEG at $\xi = 2.1$. Each color represents the dehydration result of one good droplet out of 40. The phase separation concentration for each droplet is defined as the BSA concentration at which the intensity ratio equals 0.9, obtained by linear interpolation of the continuous data. The phase separation concentration is determined as 64.72 ± 0.71 mg/mL by averaging the results of all good droplets. 129

Figure 7.3 a) Phase diagram for BSA and 4 kg/mol PEG created via the microfluidic experiments. Each dashed line represents one dehydration experiment with a constant mass ratio of BSA to PEG, defined as ξ . The squares and circles represent the loading solute concentrations and the concentrations at which optical change occurs. At $\xi = 12.5$, the droplet gelled (open circle). b) Dehydration sequence of a droplet at $\xi = 12.5$. The droplet is gelled (image 3) and no optical change is observed throughout the dehydration process. 131

Figure 7.4 BSA concentration as a function of molecular weight (MW) of PEG at $\xi = 2.1$. The inset shows the dehydration sequence of a typical droplet containing BSA with 100 kg/mol PEG. Small droplets occur and coalesce into larger droplets during the dehydration process. Images 1 and 2 show the microfluidic device for PEG of MWs other than 100 kg/mol and 100 kg/mol PEG, respectively. 132

Figure 7.5 C_t, BSA as a function of C_i, BSA for BSA with 1.5 kg/mol PEG at $\xi = 2.1$. Images 1 and 2 show the frame where the optical change is first observed. 133

Figure 7.6 Comparisons between microfluidic results (circle) and macroscopic experiment (triangles) for BSA with 1.5 kg/mol PEG at $\xi = 2.1$ as an example. All three macroscopic samples show clear single phase solutions as illustrated by the inset. 135

List of Table

Table 5.1 Tabulated parameters obtained from fitting the viscosity-concentration curves to $\eta = a\exp(bC)$	78
Table 6.1 Identified transition concentrations by statistical parameters compared with that determined by literature.	113

Chapter 1. Introduction

Biopharmaceutical proteins have attracted increasing interest and been widely developed for different therapeutics, including use in oncology, infectious diseases, and genetic disorders due to their high specificity and efficacy. [1, 2] Subcutaneous injection is one of the most common routes for delivering protein-based drugs due to its convenience of self-administration and avoidance of the acidic environment of oral delivery. However, subcutaneous injection requires the protein solutions to be formulated at high concentrations, typically >100 mg/mL, due to the limited injection volume (< 1.5 mL). The high concentrations induce challenges in the manufacturing and administration of the therapeutic proteins. [3] High concentrations result in increases in protein-protein interactions that often exacerbate the increase in viscosity, which can exceed the 50 cP limit for subcutaneous injection, and complicate processing steps such as syringe fill, filtration, and pumping. In addition, high concentration formulations increase the tendency of proteins to aggregate, which reduces the stability of proteins, leading to decreased efficacy and undesired side effects. Degradation of the protein-based drug can also be induced by the elevated protein concentrations.

The physical properties of the concentrated protein solutions are sensitive to the formulation conditions, such as protein concentrations, pH, ionic strength, and excipients, which is a complicated multi-component system. Accurate knowledge of properties as a function of composition or formulation is needed for the process design and development of therapeutic proteins. [4, 5] A significant hurdle is the fact that a large sample volume ($> \text{mL}$) is required by the conventional

analytical techniques for measuring the properties, limiting the characterization of a reasonable composition space due to small available amounts of novel proteins. New techniques have been developed with the intent of reducing the sample volume required for measurements, however, only discrete data points are provided with large gaps in understanding the underlying mechanisms and no way to efficiently characterize a new target protein. Extensive studies have been conducted to examine the protein-protein interactions, which are applied to establish theoretical models to predict the behaviors of concentrated proteins. They succeed under certain formulation conditions, but have failed for other systems. To improve the robustness and extend the applicability of the developed models for calculating and predicting protein behaviors over a wide range of formulation parameter space, a large number of experimental data is required for parameter fitting. Recently machine learning has been applied to predict the viscosity of high concentration formulations. However, the uncertainties in the experimental data have a considerable influence on the feature selection and classification accuracy of the developed model.

Therefore, in this thesis, we develop a droplet-based microfluidic approach incorporated with various sensing methods to precisely quantify the different physical properties of the concentrated protein solutions. Aqueous droplets, as the dispersed phase, are generated in the continuous phase oil and are retained in the designed microfluidic traps for long-time observation. Due to water evaporation, droplets shrink in size as time goes by, and the concentration process of the solute is live-monitored. Only a small sample volume ($\sim\mu\text{L}$) is needed to generate data

with high compositional resolution, which can provide useful information on the formulation design for therapeutic proteins. In Chapters 3–5, the droplet-based microfluidic device is combined with multiple particle tracking microrheology (MPT) as the sensing method to quantify the viscosity of concentrated protein solutions over a wide range of composition space. The proof of concept is demonstrated in Chapter 3 by characterizing the concentration dependence of viscosity for two well-studied globular proteins. The design space and feasibility of the approach are thoroughly discussed. Chapter 4 extends the study in Chapter 3 by increasing the number of parameters in the system. The viscosity of a globular protein is systematically quantified as a function of ionic strength and pH besides the protein concentration. In Chapter 5, the microfluidic device with MPT is applied to assess the impact of multiple excipients on the viscosity of concentrated antibody solutions at various concentrations and pH, further expanding the covered parameter space. In chapter 6, the droplet-based microfluidic device is combined with the polarizing microscopy, where birefringence is applied as the sensing method to identify the phase transitions of a lyotropic liquid crystal, which is chosen due to the richness in optical polarization. The phase transitions are accurately quantified using the microfluidic device and the underlying mechanisms are investigated by adding different additives. Standard image analysis techniques are applied to automate the identification process of the phase transitions. This technique can be potentially extended to study the crystallization of protein solutions, which can also be sensed by birefringence. Through Chapters 3-6, the inherent dehydration time scale and the micrometer length scale have negligible

effects on the measured physical properties. In Chapter 7, turbidity is applied as the sensing method to identify the phase separation and precipitation of a globular protein induced by polyethylene glycol. The impact of the time- and length-scale, and the application limit of the microfluidic approach are discussed.

This is the first time that the microfluidic shrinking droplets combine with birefringence and MPT. Successful quantification of the physical properties of the concentrated protein solution demonstrates the potential of the novel approach to provide data with high compositional resolution over process-relevant parameters that are needed for therapeutics formulation development. The tool can be easily implemented due to the simplicity of the technique. Formulation scientists can use this tool to develop and screen the formulations to achieve desired physical properties.

Reference

1. Sauna ZE, Lagassé HAD, Alexaki A, Simhadri VL, Katagiri NH, Jankowski W, Kimchi-Sarfaty C (2017) Recent advances in (therapeutic protein) drug development. *F1000Research*.
2. Buss NAPS, Henderson SJ, McFarlane M, Shenton JM, De Haan L (2012) Monoclonal antibody therapeutics: history and future. *Curr Opin Pharmacol* 12:615–622
3. Shire SJ, Shahrokh Z, Liu J (2004) Challenges in the development of high protein concentration formulations. *J Pharm Sci* 93:1390–1402
4. Yadav S, Shire SJ, Kalonia DS (2010) Factors Affecting the Viscosity in High Concentration Solutions of Different Monoclonal Antibodies. *J Pharm Sci* 99:4812–4829
5. Krishnan S, Pallitto MM, Ricci MS (2010) Development of Formulations for Therapeutic Monoclonal Antibodies and Fc Fusion Proteins. *Formul Process Dev Strateg Manuf Biopharm* 383–427

Chapter 2. Materials and Methods

2.1 *Materials*

Light mineral oil and fluorinated FC-70 oil are used as the continuous phase oils in this work, which are purchased from Fisher Scientific (Hampton, NH), and 3M (St. Paul, MN), respectively. Span-80 is purchased from Sigma-Aldrich, and 008-FluoroSurfactant is purchased from RAN Biotechnologies, Inc. (Beverly, MA), which are added to the mineral oil and FC-70 oil, respectively, for droplets generation. Yellow-green (YG) fluorescently labeled, carboxylated polystyrene probe particles with radius of $0.26 \pm 0.007 \text{ }\mu\text{m}$ and $0.50 \pm 0.020 \text{ }\mu\text{m}$ are purchased from Thermo Fisher Scientific (Waltham, MA), which are used as the tracer particles for the multiple particle tracking measurements. Other materials used in this work will be discussed in their corresponding chapters in detail.

2.2 *Fabrication of microfluidic device*

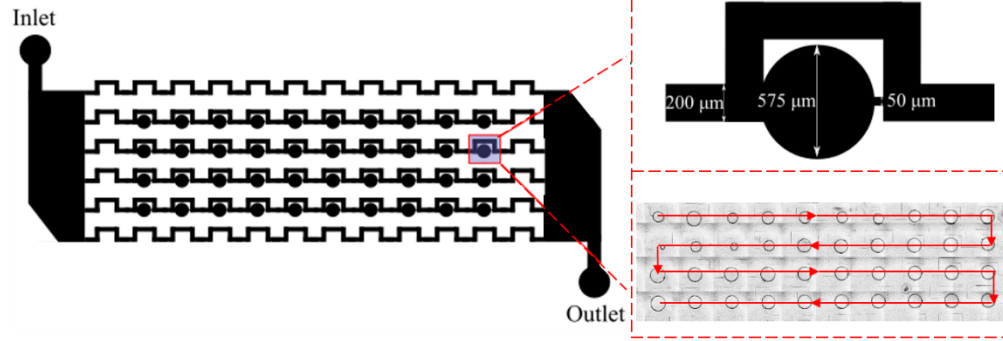
The microfluidic device is made of polydimethylsiloxane (PDMS) and is fabricated based on standard photolithography techniques[1–3]. The design of the device and detailed fabrication procedure are reported previously by our colleagues [1, 4, 5]. PDMS is purchased from Dow Corning (Midland, MI). It is packaged in a two-part kit (Sylgard 184) containing both the base and curing agent. A mold of 100 μm thick droplet traps is made using SU-8 3050 (Microchem Corp., Westborough, MA) on top of a 3-inch silicon wafer. PDMS base is mixed with the curing agent in a 10:1 ratio and 15 g is poured onto the mold. 12 g of the PDMS mixture is poured into a clean petri dish to generate a non-patterned PDMS slab. The two slabs are degassed under vacuum for nearly 15 min to remove bubbles and

are then cured at 60 °C for 2 h. To be mentioned, the mass of the PDMS mixture determines the device thickness, which will affect the dehydration rate of the droplets and the focus of the sample in the droplets. When making the microfluidic device for MPT measurements, approximately 6g of the PDMS mixture is poured onto the surface of a clean plastic petri dish, which is attached to a spin coater. By applying a spin rate of 233 rpm with an acceleration of 500 rpm/s for 1min, a clear PDMS slab of 0.5 mm thickness can be generated, which is thin enough for the working distance of a 60× objective applied for MPT measurements. After cooling to room temperature, both slabs are cut and peeled from the mold and petri dish, respectively. The inlet and outlet are punched on the PDMS device. The two slabs are surface treated via the oxygen plasma chamber (Harrick Plasma Cleaner PDC-32G) for 1min and then are quickly combined together. Then the bonded PDMS device is baked at 180 °C for 1 h. Once cooled, the devices are cleaned with tape and cut into individual devices. 8 devices can be generated each time based on the currently designed mask. The devices are soaked in the continuous phase fluid for 5 days before loading the sample solutions.

2.3 Droplet generation and concentration measurements in shrinking droplets

The top view of the device is shown in Figure 2.1 (top). The device holds 40 nanoliter-sized droplets in an array of traps. Each droplet trap has a diameter of 575 μm , a 200 μm wide bypass channel, and a restriction channel with a width of 50 μm . The depth of the trap is approximately 100 μm across the device. To produce droplets, the device is initially filled with the continuous outer phase fluid,

Top view



Side view

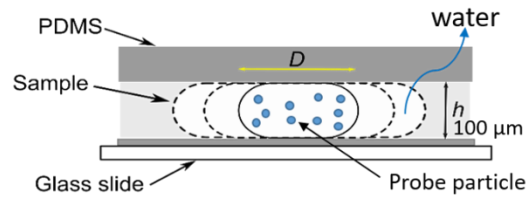


Figure 2.1 Top view of the microfluidic device and a droplet trap (top). A schematic of the side view of the device (bottom) shows that water slowly diffuses out the droplet and concentration increases. The grayscale image on the top-left indicates the produced 40 droplets.

either mineral oil or fluorinated oil (FC-70). 2wt% Span-80 and 008-FluoroSurfactant, the surfactants used to provide proper wetting conditions and lower interfacial tension for droplet production, are added to mineral oil and FC-oil, respectively. Then a roughly $1.5 \mu\text{L}$ slug of the dilute and well mixed aqueous sample solution is injected from the inlet, followed by another slug of the oil phase, which results in droplets of the aqueous dispersion in each trap within a continuum of oil. The grayscale image on the top right illustrates the produced 40 droplets. Surfactant is rinsed with pure continuous phase oil after droplet generation

Each droplet is confined in the trap, exhibiting a pancake shape with a circular projected area as viewed from the top of the device. Eqn. (2.1) is used to

calculate the droplet volume, $V_{pancake}$, in terms of the diameter of the circular projected area, D , and the height of the channel, h [4, 5],

$$V_{pancake} = \frac{4}{3}\pi \left(\frac{h}{2}\right)^3 \left(1 + \frac{3}{2h^2} \left[(D - h) \left(D - \frac{1}{2}(2 - \pi)h\right)\right]\right) \quad . \quad (2.1)$$

Water slowly diffuses out of each droplet first by partitioning into the oil phase and then through the PDMS (shown in Figure 2.1 (bottom)), and the droplet decreases in volume. Previous work has verified that solute remains inside the droplet during droplet shrinking [1]. Therefore, as time goes by, the concentration of solute increases. The dehydration process of each droplet is monitored under a Nikon Ti-U microscope by taking sequential images at a specified time interval. The captured images are analyzed using a MATLAB code developed to fit a circle to the edge of the droplet and determine the droplet diameter at each time point. This diameter is used to calculate the droplet volume (Eqn. (2.1)), which is then converted to the concentration of solute based on mass balance. Therefore, the increasing solute concentration can be accurately tracked inside a droplet. Figure 2.2 illustrates the droplet diameter (left) and solute concentration (right) as a function of time for a representative droplet. The droplet is only allowed to shrink to the point that the diameter is comparable to the trap height, $100 \mu\text{m}$. Below this, the pancake shape is lost, and Eqn. (2.1) is no longer valid. While $D > h$, the diameter of the droplet decreases linearly with time during data acquisition. The linear slope represents the dehydration rate. Since droplets have different locations on the device, they evaporate at different rates. The droplets located on the edge of the device have higher dehydration rates due to a faster water partitioning, while those in the center

have lower rates. The dehydration rates typically range from 0.2 to 0.4 $\frac{\mu m}{min}$.

Therefore, at each time point, droplets have different diameters, which results in variation in solute concentrations. This is an advantage that allows us to cover a

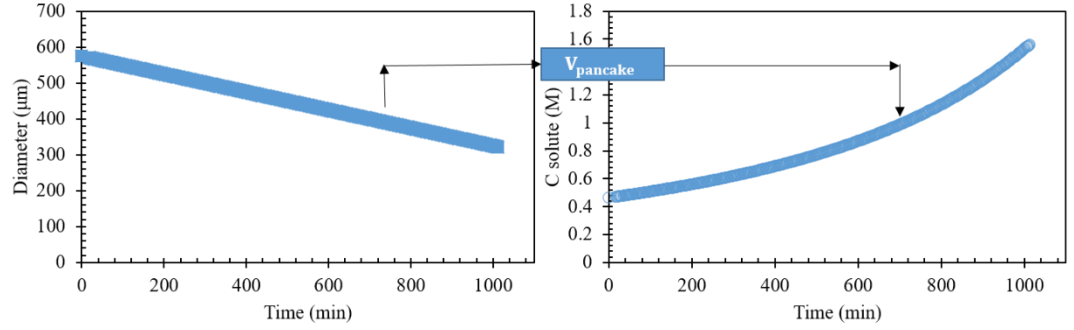


Figure 2.2 Measured droplet diameter and calculated solute concentration as a function of time for a typical droplet.

wide range of concentrations at each time point, which will be discussed specifically in the chapters. Droplets are dehydrated at room temperature ($22 \pm 1^\circ C$).

Overall dehydration rates are controlled by temperature, humidity, and device thickness. A typical time for complete droplet shrinking is approximately 24 -30 h under the current lab conditions, which minimizes concentration gradients inside

the droplet. With a characteristic length, L , of $100 \mu m$ for the drop, the mass transfer

Biot number, $B_i = \frac{k_c}{D} L$ (k_c and D are mass transfer coefficient and mass diffusivity,

respectively), is calculated to be on the order of 10^{-4} under the current dehydration

rates, indicating uniform composition inside the droplet. As the concentration of

solute increases in the shrinking droplet, phase transitions, crystallization, and

gelation can occur. At some point, droplets lose their circular shape, and deviation

from the linearity of diameter vs. time is observed. The elevated solution viscosity

may hinder the water transport and can also cause wetting to the wall of the

channels.

In order to generate good droplets, several parameters need to be considered. First, the capillary number, which is defined as the ratio of viscous forces to the interfacial forces, is essential for droplet production. When viscous forces strongly dominate, the droplets will easily pinch off, but will also be pushed out through the restriction channel and mess the droplet generation. If the interfacial forces dominate strongly, the droplets will be hard to pinch off and will be pulled from the trap, which fails to generate droplets in the trap. A value of capillary number between 10^{-4} and 10^{-2} is desire for generating droplets. [6]

Second, the type of continuous phase oil is chosen based on the properties of the sample solution. In this work, for solutions at acidic and neutral pH, the droplets are generated with light mineral oil as the continuous phase. For solutions at alkaline pH and high ionic strength, inappropriate wetting was observed using mineral oil, therefore, the inert fluorinated FC-oil is applied as the continuous phase oil. Water shows a slightly larger transport rate through fluorinated oil than mineral oil, and both transport rates provide the Biot number on the order of 10^{-4} .

2.4 Multiple particle tracking microrheology

The viscosity of the solution is quantified using multiple particle tracking microrheology (MPT), which is a passive microrheological technique that measures the Brownian motion of the tracer particles embedded in the sample solution. The movement of the probe particles is captured by video microscopy. The location of the particles in each frame is detected with algorithms developed by Crocker and Crier (1996) [7]. Then the positions of probe particles are connected into trajectories and used to calculate the ensemble-averaged mean-squared

displacement (MSD), $\langle \Delta r^2(\tau) \rangle$, which can be obtained using $\langle \Delta r^2(\tau) \rangle = \langle \Delta x^2(\tau) \rangle + \langle \Delta y^2(\tau) \rangle$ for two-dimensional measurements, where τ is the lag time. The ensemble-averaged MSD is related to particle diffusivity, D , by the Stokes-Einstein equation as shown in Eqn. (2.2),

$$\langle \Delta r^2(\tau) \rangle = 2dD\tau^\alpha = \frac{2dk_B T}{6\pi a\eta} \tau^\alpha, \quad (2.2)$$

where d is the dimensionality of the measurement, which in this case is 2, $k_B T$ is the thermal energy, a is the radius of the probe particle, η is the viscosity of the solution, and α is the logarithm slope of the MSD. Viscosity is calculated from the y-intercept of a log-log plot of MSD versus τ . All of the measurements in this work are of diffusive particle motion, $\alpha = 1$.

Several factors need to be considered when performing the MPT measurements. First, the choice of probe particles is essential for MPT experiments. The particles need to avoid mutual interactions and interactions with measured materials. Various surface treatments have been developed to prevent particle interactions, such as introducing surface charges, [8] grafting BSA on the particle surface, [9] and pegylation of the particles.[10][11] In this work, carboxylated, fluorescently labeled polystyrene probe particles are used for MPT measurements. The size of the probe particles needs to be properly chosen to first satisfy the continuum approximation, which requires the particle size to be much larger than the length scale of the measured material. [8] Second, the probes need to have a diameter that can provide enough number of pixels to identify the particle location. In addition, the particle size should not be too large otherwise the particle will easily

sediment to the bottom surface. In this work, the probe particles with radius $0.26 \pm 0.007 \mu\text{m}$ and $0.50 \pm 0.020 \mu\text{m}$ are dispersed in the solution and undergo Brownian motion. Particle concentration is another key parameter need to be considered for MPT experiments. Either $0.26 \mu\text{m}$ or $0.50 \mu\text{m}$ probes are added into each sample with concentrations of 0.036% and 0.072% solids per volume, respectively. The probe concentration is chosen to guarantee that 50-100 probes are in the focal plane to provide enough statistics for accurate MPT measurements and also avoid brightness saturation from the out-of-focus particles. Details of the calculation of the size and concentration of the probe particles will be discussed in Chapter 3.

The second factor is the experimental setup. The camera frame rate and exposure time are chosen to minimize the static and dynamic errors associated with video microscopy particle tracking [12], which affect the accuracy of measured particle trajectories. The static error arises from locating the exact position of a stationary particle, which is limited by the experimental apparatus. While the dynamic error is induced by the particle motion over the time of image acquisition. [12] The static error can be reduced by choosing the right probe concentrations to minimize the background noise from the unfocused probes and improves the signal-to-noise ratio. It can also be reduced by applying the high-magnification objective, which will provide at least 4-5 pixels for the particle diameter. [8, 13] The dynamic error can be minimized by choosing the shortest exposure time at a given frame rate to ensure that $\tau/\sigma \gg 1$. [12] However, decreasing the exposure time will reduce the signal-to-noise ratio, thus increasing the static error. In fact, the static and dynamic error can cancel each other as shown in Eqn. (2.3).

$$\langle \Delta \hat{r}^2(\tau, \sigma) \rangle = 4D \left(\tau - \frac{\sigma}{3} \right) + 2\bar{\varepsilon}^2, \quad (2.3)$$

where $2\bar{\varepsilon}^2$ and $-4D \frac{\sigma}{3}$ represent the contributions from the static and dynamic error, respectively. [8] Based on Eqn 2.3, the static and dynamic errors will be observed in the interpretation of the particle tracking results as they will induce a subdiffusion and superdiffusion in the MSD curve, respectively. The appropriate experimental parameters can be determined by conducting the MPT measurements on a Newtonian solution, glycerol, with various concentrations at different exposure times and frame rates. [14] The deviation of the logarithmic slope from 1 will indicate the presence of error. Glycerol solutions with concentrations from approximately 10 wt% to 90 wt% are characterized at 40 fps with four different exposure times. Figure 2.3 shows an example of 84% glycerol. Subdiffusion, an upward turning of the MSD curve, is observed at $\sigma = 5$ ms, especially at short lag times, indicating the dominance of static error. As σ increases to 15 ms or higher, superdiffusion, a downward turning of the MSD curve, is observed, showing that dynamic error dominates. $\sigma = 10$ ms provides $\alpha=1$, indicating that the static and dynamic errors cancel with each other. The same trend is observed for the other glycerol concentrations. Therefore, in this work, the frame rate and exposure time are identified as 40 fps and 10 ms, respectively. The movement of 50 – 100 in-frame particles is captured under fluorescence microscopy at 2048×2048

resolution for a total of 1200 frames. The measurable range of MPT in the shrinking droplets will be discussed in detail in Chapter 3.

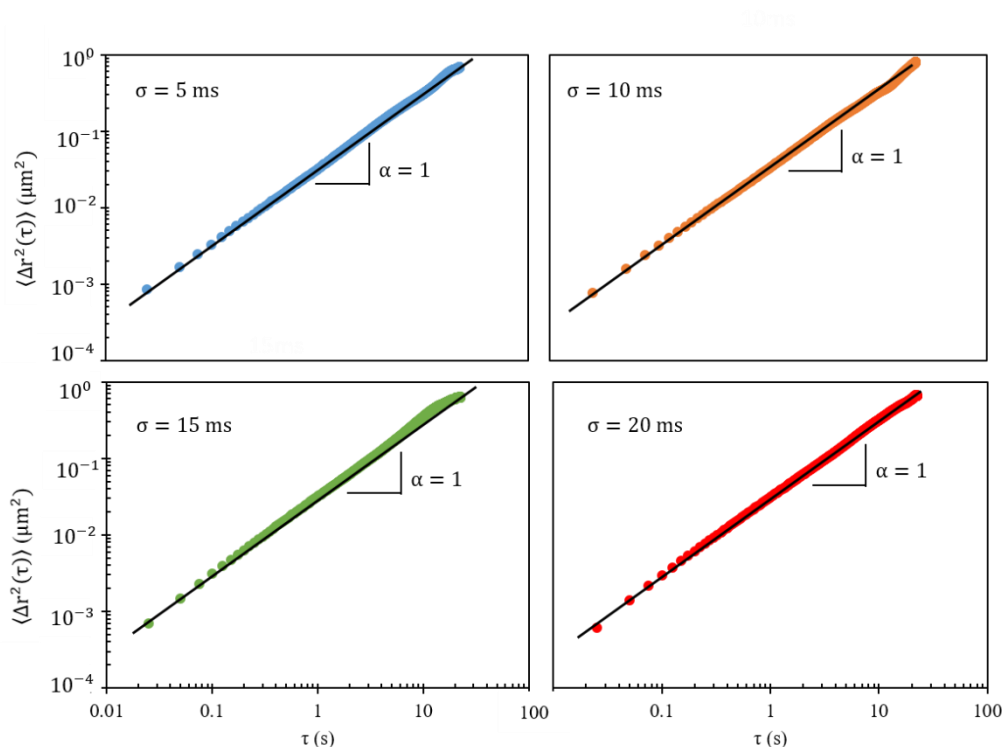


Figure 2.3 MSD for 84 wt% glycerol at 40 fps with various exposure times, σ . Subdiffusion and superdiffusion are observed as the exposure time increases from 5 ms to 20 ms, especially at short lag times. $\sigma = 10$ ms provides diffusive motion, where $\alpha = 1$.

2.5 Microscopy

An inverted Nikon Ti-U microscope at 10 \times magnification and a pco.panda 4.2 camera (0.65 $\mu\text{m}/\text{pixel}$) are used to track droplet dimensions during shrinking under bright field conditions. For each dehydration experiment, the diameters of all 40 droplets are measured at a specified time interval. At each time point, the entire device is automatically scanned in a zig-zag path across the device as shown by the red arrows in the grayscale image of Figure 2.1, taking an image of every droplet. The MS-2000 XY translational stage (Applied Scientific Instrumentation; Lane county, OR) of the microscope is controlled by Micro-Manager software, which

enables the automatic scanning of the entire device. Each diameter scan of the device requires 1.5 minutes, which is negligible compared to the overall dehydration time. The phase transitions of liquid crystals are monitored under the same inverted Nikon Ti-U microscope with crossed polarizers. For multiple particle tracking measurements, the movement of the particles is tracked using the same microscope and camera at 60× magnification ($0.11\ \mu\text{m}/\text{pixel}$) with an ultraviolet (UV) light source (X-cite 120 lamp) and a FITC filter set.

2.6 *Reference*

1. Bleier BJ, Anna SL, Walker LM (2018) Microfluidic Droplet-Based Tool To Determine Phase Behavior of a Fluid System with High Composition Resolution.
2. Xia Y, Whitesides GM (1998) Soft lithography. *Annu Rev Mater Sci* 28:153–184
3. McDonald JC, Duffy DC, Anderson JR, Chiu DT, Wu H, Schueller OJA, Whitesides GM (2000) Fabrication of microfluidic systems in poly(dimethylsiloxane). *ELECTROPHORESIS: An International Journal* 21(1): 27-40.
4. Bleier BJ (2018) Droplet-Based Approaches to Probe Complex Behavior in Colloidal Fluids with High Composition Resolution.
5. Vuong SM (2014) A microfluidic platform for the control and analysis of phase transitions in concentrating droplets.
6. Bithi SS, Vanapalli SA (2010) Behavior of a train of droplets in a fluidic network with hydrodynamic traps. *Biomicrofluidics* 4:044110
7. Crocker JC, Grier DG (1996) Methods of digital video microscopy for colloidal studies. *J Colloid Interface Sci* 179:298–310
8. Furst EM, Squires TM. *Microrheology*. Oxford University Press; 2017.
9. McGlynn JA, Wu N, Schultz KM (2020) Multiple particle tracking microrheological characterization: Fundamentals, emerging techniques and applications. *J Appl Phys* 127:201101
10. T G, A S (2019) Synthesis and application of PEGylated tracer particles for measuring protein solution viscosities using Dynamic Light Scattering-based microrheology. *Colloids Surf B Biointerfaces* 181:516–523
11. Valentine MT, Perlman ZE, Gardel ML, Shin JH, Matsudaira P (2004) Colloid Surface Chemistry Critically Affects Multiple Particle Tracking Measurements of Biomaterials. 86:4004–4014
12. Savin T, Doyle PS (2005) Static and dynamic errors in particle tracking microrheology. *Biophysical journal*. 88(1): 623-38.
13. Larsen TH, Larsen TH (2008) by.
14. Wehrman MD, Lindberg S, Schultz KM (2018) Multiple particle tracking microrheology measured using bi-disperse probe diameters. *Soft Matter* 14:5811–5820

Chapter 3. Droplet-based microfluidic tool to quantify viscosity of concentrating protein solutions

3.1 Introduction

Protein therapeutics make up an increasingly large fraction of pharmaceutical drugs for treatment of a diversity of diseases, including cancers, autoimmune disorders, infectious diseases and genetic disorders. [1–3] These proteins are too sensitive for oral delivery due to the proteases and acidic media of the stomach, [4, 5] therefore, subcutaneous injection is a preferred route of administration; it is also more convenient than intravenous delivery. [4–6] Despite the advantages of subcutaneous injection, it requires high doses (>100 mg) in a small volume (< 1.5 mL) and hence, proteins must be formulated at high concentrations, usually exceeding 100 mg/mL. [4, 5] High concentration induces a drastic increase in the viscosity, which can exceed the 50 cP limit for subcutaneous injection, [2] and complicate processing steps like pumping and filtration. [4, 5, 7, 8] Also, higher concentrations increase the tendency of proteins to aggregate, which reduces the stability of proteins and leads to decreased efficacy and the potential for undesired side effects. [9–12] Therefore, effective control of the viscosity is essential for the development of protein-based drugs.

The viscosity of the protein solution results from the protein-protein interactions (PPIs), such as electrostatic repulsions, attractions, hydrophobic interactions, steric repulsions, and specific interactions. [13, 14] Various types of additives are added to the concentrated protein solutions to control the viscosity by interrupting the PPIs. Wang *et al.* demonstrated that NaCl lowered the viscosity of

two highly concentrated monoclonal antibodies by electrostatically shielding the charge-charge interactions between the protein molecules. [15] Inoue *et al.* showed that arginine hydrochloride (ArgHCl) significantly reduced the viscosity of antibody solutions by weakening both the electrostatic and hydrophobic interactions between protein molecules. [16] Wang *et al.* (2015) observed an increase in serum albumin viscosity with addition of amino acids. [15] Shire *et al.* (2008) examined the effect of different ions on viscosity of concentrated monoclonal antibody solutions, and the trend follows the Hofmeister series. [17] The viscosity of the concentrated protein solutions is also sensitive to pH, ionic strength, and temperature. [14, 18] Overall, this is a complicated multicomponent system and accurate knowledge of the viscosity of concentrated protein solutions as a function of formulation conditions (excipient, protein composition, pH and temperature) is essential for protein formulation and development of therapeutics.

A significant hurdle is the fact that large amount of samples (~gm) are required for current viscosity measurements [3, 15, 19–21], limiting characterization of a reasonable composition space due to small available amounts of novel proteins. In addition, when using conventional rheometers to measure the viscosity of protein solutions, the adsorption of protein molecules onto the air-liquid interface leads to misinterpretation of the measured apparent viscosity [20, 22]. Microfluidic tools have been proposed for viscosity measurements with advantages of low cost, simple operation and small sample volume. Passive microrheology, smartphone imaging and electro-mechanical method have been implemented with microfluidic technology [23–25]. However, only discrete data

points are provided in the current literature, with large gaps in understanding the underlying mechanisms and no way to efficiently characterize a new target protein.

Correlation between protein interaction parameter (k_D) measured at low concentration and viscosity at high concentration had been observed. [26, 27] However, Woldeyes *et al.* (2018) questioned the validity of applying protein-protein interaction (PPI) indicators, such as k_D and B_{22} measured at low concentration to predict the rheology behavior at high concentration by showing that the large change in net PPI exerts insignificant changes in viscosity over a range of pH and ionic strengths. [28]

Theoretical models are being developed to predict the viscosities of protein solutions at high concentrations. Colloidal theories for spherical particles have been applied to predict the viscosity behavior of globular proteins, [20, 29, 30] while Sarangapani *et al.* (2013) critically examined the applicability of colloidal models by arguing that the assumptions of the uniform surface charges and the monodispersity of the globular protein molecules are invalid. [31] The development of theoretical models relies on sufficient real experimental data.

Therefore, the field of formulation of protein solutions requires tools to precisely quantify the viscosity of concentrated protein solutions with both small amounts of materials and high compositional resolution. In this chapter, we develop a droplet-based microfluidic tool to quantify viscosities of protein solutions *in situ* as concentration increases using only microliters of sample. The corresponding viscosity is characterized by multiple particle tracking microrheology. Our technique is validated by viscosity measurements of a Newtonian fluid, glycerol, at

various concentrations. Then, the technique is applied to quantify viscosities of two different molecular weights of water-soluble polymer, poly(ethylene) glycol (PEG), and is further extended to two types of well-studied proteins: Bovine serum albumin (BSA) and lysozyme, demonstrating the applicability in simple protein systems. The device is able to accurately measure viscosity over a wide range of concentrations with small sample volume ($\sim \mu\text{L}$) and high compositional resolution.

3.2 *Materials and Methods*

3.2.1 *Materials*

Glycerol is purchased from Sigma-Aldrich (St. Louis, MO). 4 kg/mol and 100 kg/mol poly(ethylene) glycol (PEG) are obtained from Sigma-Aldrich and Polysciences Inc. (Warminster, PA), respectively. Bovine Serum Albumin (BSA) is purchased from Sigma-Aldrich (Catalog number: A7030). Lysozyme is purchased from EMD Millipore Corp. (Burlington, MA; Catalog number: 4403). All solutions with varying concentrations are made by mixing known mass of solute with the deionized water ($18.2 \text{ M}\Omega\cdot\text{cm}$) at a known volume in a volumetric flask and are well mixed before using.

3.2.2 *Microscopy*

An inverted Nikon Ti-U microscope at $10\times$ magnification and a pco.panda 4.2 camera ($0.65 \mu\text{m}/\text{pixel}$) are used to track droplet dimensions during shrinking under bright field conditions. The MS-2000 XY translational stage (Applied Scientific Instrumentation; Lane county, OR) of the microscope is controlled by

Micro-Manager software, which enables the automatic scanning of the entire device. Multiple particle tracking microrheology experiments are conducted using the same microscope and camera at $60\times$ magnification ($0.11\ \mu\text{m}/\text{pixel}$) with an ultraviolet (UV) light source (X-cite 120 lamp) and a FITC filter set.

3.2.3 Multiple particle tracking microrheology

The viscosity of the solution is quantified using multiple particle tracking microrheology (MPT). Carboxylated, fluorescently labeled polystyrene probe particles with radius $0.26 \pm 0.007\ \mu\text{m}$ and $0.50 \pm 0.020\ \mu\text{m}$ are purchased from Thermo Fisher Scientific (Waltham, MA), which are dispersed in the solution and undergo Brownian motion. Either $0.26\ \mu\text{m}$ or $0.50\ \mu\text{m}$ probes are added into each sample with concentrations of 0.036% and 0.072% solids per volume, respectively. Video microscopy is used to capture the movement of the particles, using the inverted Nikon Ti-U microscope ($60\times$ mag, $0.11\ \mu\text{m}/\text{pixel}$) equipped with a sCMOS camera (PCO, pco.panda 4.2) and an ultraviolet (UV) light source (X-cite 120 lamp). The movement of 50 – 100 in-frame particles is captured at 2048×2048 resolution for a total of 1200 frames at 40 fps (30 seconds) and 10ms exposure time. Theory and details of MPT can be found in Chapter 2.4. All of our measurements are of diffusive particle motion, where the logarithm slope $\alpha = 1$. Viscosity is calculated from the y-intercept of a log-log plot of MSD versus τ .

3.2.4 Validation of MPT and results obtained in the microfluidic device

To validate our experimental setup for accurate MPT measurements, viscosity measurements are performed in a glass sample chamber, which is made of a $25 \times 75 \times 1\ \text{mm}$ glass slide with glass spacers of 0.16 mm height and a

25×25×0.16 mm top coverslip, all purchased from Sigma Aldrich. [32] The samples are injected into the chamber and sealed with UV curable adhesive (NOA-81) (Norland Products, Inc., Cranbury, NJ) to prevent leaking. MPT measurements are taken of these samples.

The viscosities obtained from the microfluidic device are compared with macroscopic measurements taken using Ubbelohde viscometers. Three sizes of viscometer 50, 100 and 300 are used for different viscosity ranges. Each viscometer is first calibrated with solution of known viscosity and then used to measure viscosity of sample solutions. All measurements are performed in a water bath maintained at $22 \pm 1^\circ\text{C}$. For 100 kg/mol PEG solutions, the microfluidic results are compared with measurements obtained using a torsional rheometer (TA Instrument, DHR-2; Bellingham, WA) taken by our colleague.

3.3 Approach

3.3.1 Concentration measured in shrinking droplets

The dilute and well-mixed aqueous sample solution is concentrated inside a droplet-based microfluidic device, which is made of PDMS. 40 nanoliter-sized aqueous droplets are produced hydrodynamically inside the microfluidic traps and are surrounded by the mineral oil, which is the continuous phase oil. 2 wt% Span-80 is added into the mineral to provide proper wetting conditions and lowers the interfacial tension for droplet production. Details of device fabrication and droplet generation are thoroughly discussed in Chapter 2.

Water slowly diffuses out of each droplet first by partitioning into the mineral oil and then through the PDMS, and the droplet decreases in volume. As time goes by, the concentration of solute increases. The dehydration process of each droplet is monitored under the microscope by taking sequential images at a specified time interval. The droplet diameter at each time point is measured and used to calculate the droplet volume (Eqn. (2.1)), which is then converted to the concentration of solute based on mass balance. Details of concentration calculation can be found in Chapter 2. Droplets are dehydrated at room temperature ($22\pm1^{\circ}\text{C}$). Overall dehydration rates are controlled by temperature, humidity, and device thickness. A typical time for complete droplet shrinking is approximately 24 -30 h under the current lab conditions, which minimizes concentration gradients inside the droplet.

3.3.2 Concentration-dependence of viscosity measured in shrinking droplets

In this work, the diameters of all 40 droplets are measured every 1 or 2 hours. At each time point, the entire device is automatically scanned in a zig-zag path across the device as shown by the top inset in Figure 3.1, taking an image of every droplet. Each diameter scan of the device requires 1.5 minutes, which is negligible compared to the overall dehydration time. Since droplets have different locations on the device, they evaporate at different rates. The droplets located on the edge of the device have higher dehydration rates due to a faster water partitioning, while those in the center have lower rates. Therefore, at each time point, droplets have

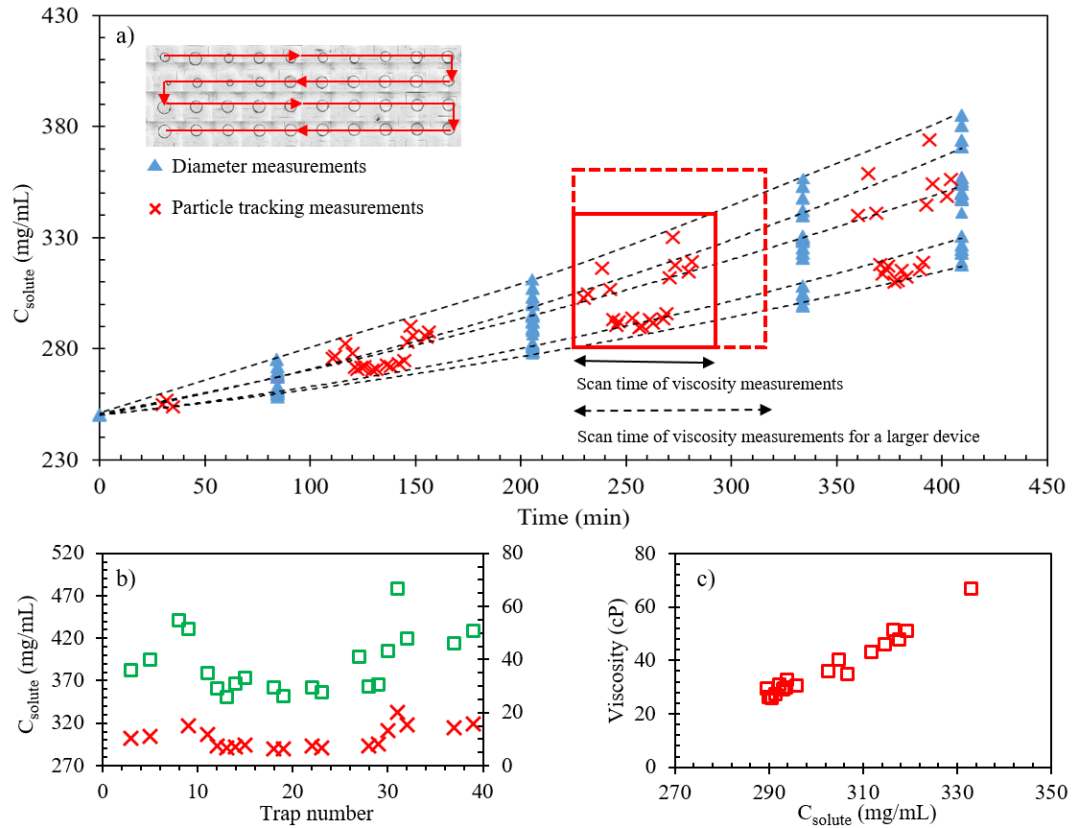


Figure 3.1 Viscosities are measured along the increasing concentration in shrinking droplets. a) Droplet diameters are tracked as a function of time for all 40 drops by scanning the device in the zig-zag direction (shown by the inset) every 1 or 2 hours. The corresponding solute concentrations are shown as the filled blue triangles. Viscosities are measured during the dehydration process. The corresponding solute concentrations calculated based on the linear-extrapolated diameter are represented by the red crosses. Each cluster represents one viscosity scan, which takes approximately 40 min. b) The variation in solute concentration (red crosses) and viscosity (green squares) as a function of drop position during one viscosity scan. c) Viscosity as a function of concentration with high composition resolution by replotting data provided in b).

different diameters, which results in variation in solute concentrations. In Figure 3.1 a, the filled blue triangles represent solute concentration as a function of time for all 40 droplets. At each time point, the vertical spread of the blue triangles indicates the variation in solute concentration among droplets. The dotted lines illustrate the increase in concentration for each droplet.

The viscosity of the solution in each droplet is tracked during the concentrating process. Between every two diameter scans, the viscosity of all 40 droplets are measured one by one in the same zig-zag direction across the device using MPT. Since the droplet diameter depends linearly on time, the time point at which the viscosity is measured is used to extrapolate the droplet diameter accurately. The diameter can then be used to calculate the solute concentration at this time point. The red crosses in Figure 3.1 a represent the solute concentrations at which the viscosities are measured. Each cluster of red crosses represents one viscosity scan, which takes roughly 40 minutes. Taking the third cluster as an example, since droplets evaporate at different rates, during the 40 minutes of one viscosity scan, a range of solute concentrations is sampled, which is shown by the spread of the red crosses. The length and height of the red box illustrate the scan time and the covered concentration range for one viscosity scan. Figure 3.1 b plots the same solute concentrations (red crosses) and the corresponding viscosity (green squares) as a function of trap number. By replotting Figure 3.1 b, we obtain continuous data of viscosity versus concentration shown in Figure 3.1 c. A 10% range in concentration is covered by just one viscosity scan. By combining all clusters, we obtain viscosity over a wide range of solute concentrations with high compositional resolution. The concentration range covered by each viscosity scan can be increased by either reducing the scan rate or increasing the size of the device, which is illustrated by the height of the dotted red box. To prevent probe particles from sedimenting, the device is slowly rotated on a rotator between each viscosity scan.

3.3.3 Design space of the device

There is a range of viscosities that can be measured by MPT; the maximum and minimum measurable viscosities are calculated based on Eqn.(3.1), [33]

$$\eta_{max/min} = \frac{2k_B T}{3\pi a \delta^2} \tau \quad , \quad (3.1)$$

where $k_B T$ is the thermal energy, a is the radius of the probe particle, τ is the lag time, and η is viscosity. First, due to the limited thermal energy available for Brownian motion, the optical resolution sets the upper limit of the measurable viscosity. In this case, δ is the spatial resolution and is determined by measuring the MSD of probe particles that are not moving. In this work, the particles are forced to settle in a 1M NaCl solution. [34] δ is measured to be 13.0 ± 0.8 nm and 9.7 ± 0.9 nm for probes with radius of $0.26 \mu\text{m}$ and $0.50 \mu\text{m}$, respectively. Therefore, the maximum measurable viscosities are calculated to be 500 cP and 460 cP for $0.26 \mu\text{m}$ and $0.50 \mu\text{m}$ probe particles, respectively. In addition, in low viscosity media, the tracer diffusion is so fast that particles can move out of the focal plane during the lag time. Therefore, the lower limit of viscosity is set by the depth of focus of the objective. In this case, δ is $1.4 \mu\text{m}$ for our $60\times$ objective. With a maximum lag time of 1 sec, the minimum viscosities are then calculated to be 1.7 cP and 0.9 cP for $0.26 \mu\text{m}$ and $0.50 \mu\text{m}$ probes, respectively. The detection range of viscosity can be tuned by changing the particle size, objective lens and lag time. In addition, as droplets shrink, the confinement effect of the oil/water interface on the particle movement needs to be considered. Based on Faxen's law, the extension of

hindrance on particle mobility depends on the particle radius, a , and the distance from the particles to the interface, l , as shown in Eqn. (3.2), [35, 36]

$$\frac{b_l}{b_0} = 1 - 1.004 \left(\frac{a}{l}\right) + 0.418 \left(\frac{a}{l}\right)^3 + 0.21 \left(\frac{a}{l}\right)^4 - 0.169 \left(\frac{a}{l}\right)^5, \quad (3.2)$$

where b_l and b_0 represent the free and hindered mobility, respectively. From Eqn. (3.2), larger particles are more strongly affected by confinement, the following discussion is based on particles with radius of $0.50 \mu m$. To avoid significant confinement effects, at which $\frac{b_l}{b_0} < 0.95$, particles need to be $10 \mu m$ away from the interface. During MPT, only probes that are toward the center of the droplet are taken into account in all dimensions and probes need to be at least $10 \mu m$ away from the drop interface to avoid significant confinement effects.

The achievable range of solute concentration during droplet shrinking is first set by the geometry of the droplet. The droplet diameter cannot be smaller than the height of the trap ($100 \mu m$) to maintain the pancake-shape volume equation valid. For an initial drop diameter of $575 \mu m$, the drop volume can shrink by roughly 40 times. In addition, the volume fraction of the probes is suggested to be less than 0.01 to avoid brightness saturation during MPT. [36] The initial concentration of $0.5 \mu m$ and $0.26 \mu m$ probes are 0.072% and 0.036%, respectively, therefore the droplet is not recommended to shrink more than 15 and 30 times correspondingly, which is the same as the fold change of solute concentration.

3.4 Results

3.4.1 Validation of MPT in a glass sample chamber

MPT is validated by measuring viscosity of the Newtonian glycerol at various concentrations with probe sizes $a = 0.26 \mu\text{m}$ and $0.50 \mu\text{m}$ in a glass chamber. The results are compared with bulk rheology, which is measured by the Ubbelohde viscometer, as shown by the unity plot in Figure 3.2. The top two orange and blue dash-dotted lines represent the maximum viscosities calculated from Eqn. (3.1) for $0.26 \mu\text{m}$ and $0.50 \mu\text{m}$, respectively, at which the uncertainty in viscosity is 100%.

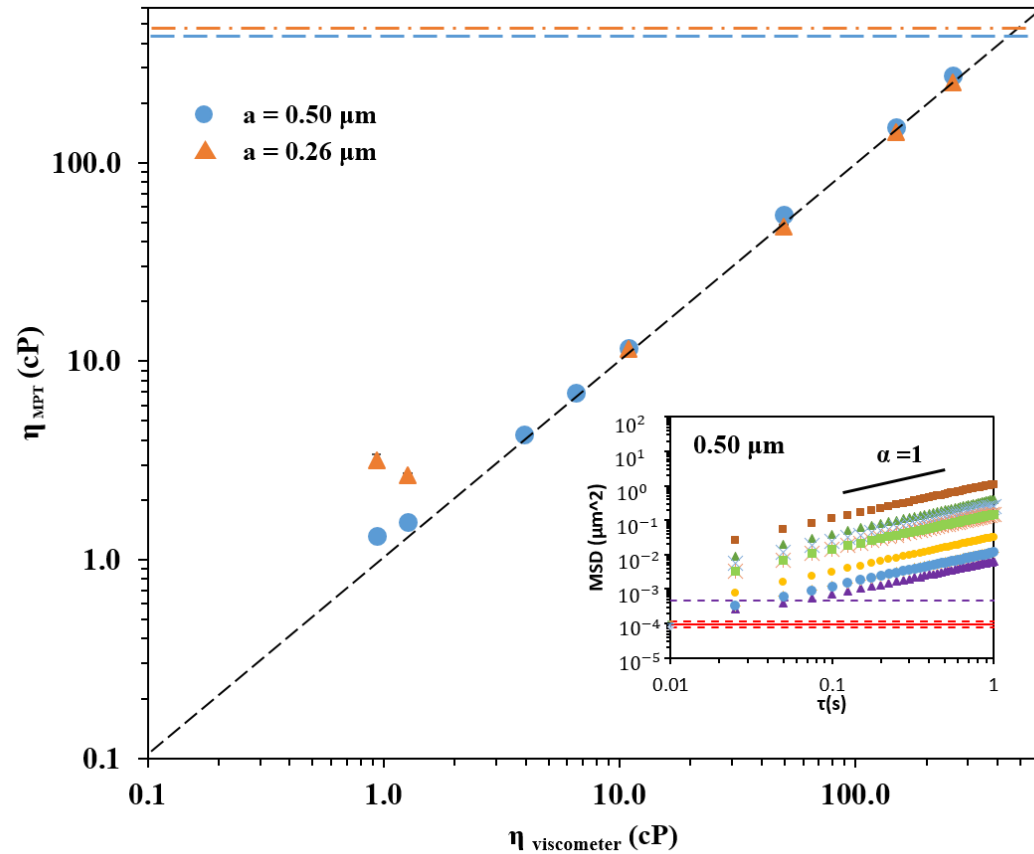


Figure 3.2 Unity plot of viscosities measured by multiple particle tracking (MPT) versus viscosities measured by viscometer of glycerol solutions at varying concentrations. The diagonal dotted line represents slope of 1. The filled orange triangles and blue circles represent results using $0.26 \mu\text{m}$ and $0.50 \mu\text{m}$ probes for MPT, respectively. The inset shows the mean-squared displacement curves for $1 \mu\text{m}$ probe particles for glycerol at various concentrations.

The diagonal dotted line represents the unity line. The filled orange triangles and blue circles show the results obtained from MPT by using 0.26 μm and 0.50 μm probes, respectively. The error bars of viscosity due to the uncertainty of probe sizes are smaller than the symbols. For viscosities above 3 cP, both probes provide consistent results with bulk rheology up to 250 cP. The inset represents the corresponding mean-squared displacement curves for a= 0.50 μm probe as an example. Each type of symbol shows a different glycerol concentration. The bottom red and purple horizontal dotted lines represent the spatial resolution and half order of magnitude above it, respectively, for the 0.50 μm probe. The magnitude of MSDs decreases as the concentration of glycerol increasing, indicating a decrease in particle movement and an increase in the solution viscosity. Both sizes of probes provide accurate results with less than 5% deviation for viscosities from 3 - 250 cP and the logarithm slope, α , equals to 1 for all measurements, indicating diffusive motion. For viscosities above 250 cP, the uncertainty of viscosities increases since the MSDs at short lag times approach to the maximum resolution of the particle tracking, which is illustrated by the slight upward curving at short lag times for the lowest MSD curve in the inset (filled purple triangles). This could result in inaccurate extrapolation of diffusion coefficient and further affect the calculated viscosity. The 0.26 μm probes move faster compared to the 0.50 μm probes, providing more resolvable MSDs at short lag times for high viscosity media. Therefore, in this work, we use 0.26 μm probes to quantify viscosities higher than 200 cP. For low viscosity media (water to 3cP), the MPT results deviate from the bulk measurements, especially for the 0.26 μm probe particles. This is because that

the smaller particles move faster and are harder to stay inside the focal plane, which truncates trajectories as lag time increases and further induces error in MSDs. [37] In this work, we use 0.50 μm probes for low viscosity solutions, which provide results within $\pm 20\%$ deviation. Overall, MPT can provide accurate measurements for viscosity up to 250 cP by showing agreement with bulk rheology.

3.4.2 Validation of MPT in microfluidic droplets

Viscosities measured by MPT inside droplets (aqueous droplets in mineral oil continuous phase) are compared with results measured in a glass chamber for glycerol (blue circles), BSA (red triangles) and lysozyme (green squares) at various concentrations. The consistency of the technique is illustrated by the unity plot in Figure 3.3. The filled points represent results measured in the droplet taken right after droplet formation (without shrinking). Most of the filled points fall on the unity line (the diagonal dashed line) and all of them are within $\pm 10\%$ deviation (2 dotted lines), indicating that the oil/water interface of the droplet has no significant effect on the viscosity measurement. The small deviation is attributed to the variation in solute concentration due to slight shrinking of the droplets between sample loading and imaging of the drop diameter. The open symbols represent the measurements obtained in the shrinking droplets, in which viscosity is quantified as a function of concentration. The viscosity of a specific solute concentration is determined by averaging the viscosities of droplets with $\pm 1\text{mg/mL}$ of that solute concentration. As shown by the open symbols, the shrinking droplet results are consistent with the results measured in the glass chamber but with a larger deviation, $\pm 20\%$, compared to the measurements taken without shrinking. The deviation is

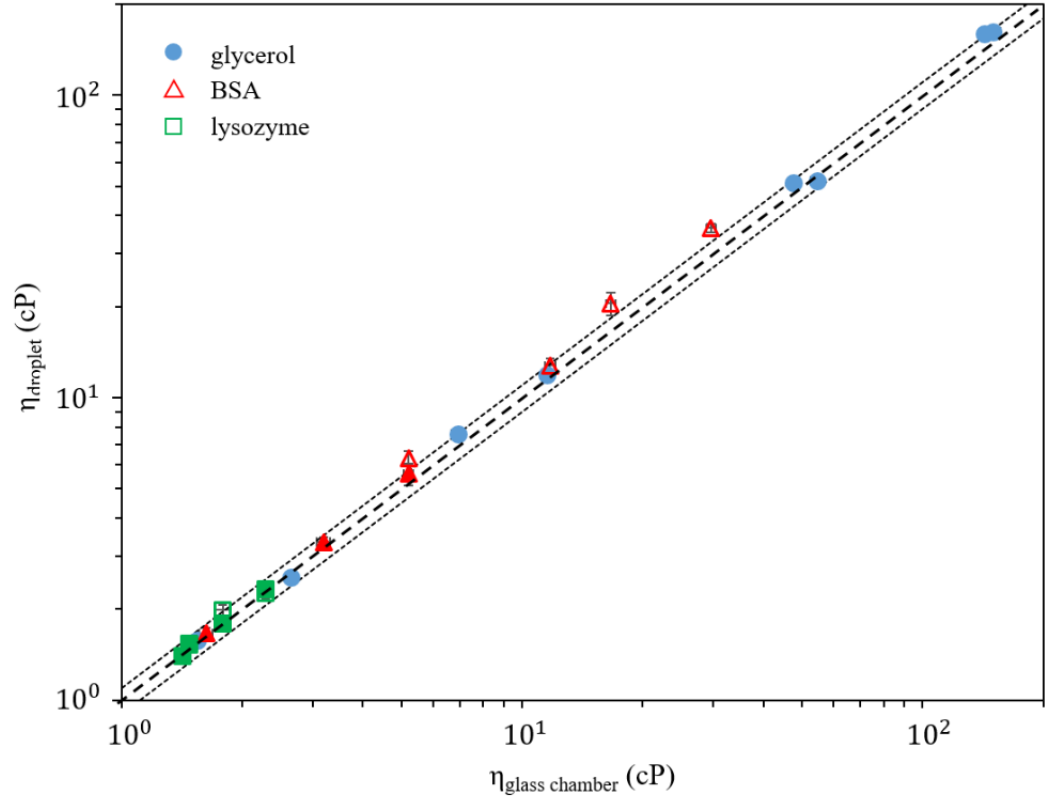


Figure 3.3 Unity plot of viscosities measured inside the droplets versus viscosities measured in the glass chamber for glycerol (blue circles), BSA (red triangles), and lysozyme (green squares) at varying concentrations. The diagonal dashed line represents a slope of 1 and the two dotted lines represent $\pm 10\%$ deviation. The open and filled symbols represent measurements in the droplet taken at initial loading and results obtained from the shrinking droplets, respectively.

attributed to the uncertainty in the solute concentration and becomes larger at higher concentrations, at which viscosity is a stronger function of concentration and small deviations in concentration impact comparison. Overall, we have demonstrated that the viscosity can be quantified inside the droplets using MPT, which we call as the ‘microfluidic results’ in the later section.

3.4.3 Viscosity measurements of PEG in shrinking droplets

To validate our technique, the viscosity is first characterized as a function of concentration in the shrinking droplets for 100 kg/mol PEG using MPT. As shown in Figure 3.4, two devices are used to cover the concentration range from 2 to 9 w/v%, which are represented by the red and yellow filled triangles, respectively.

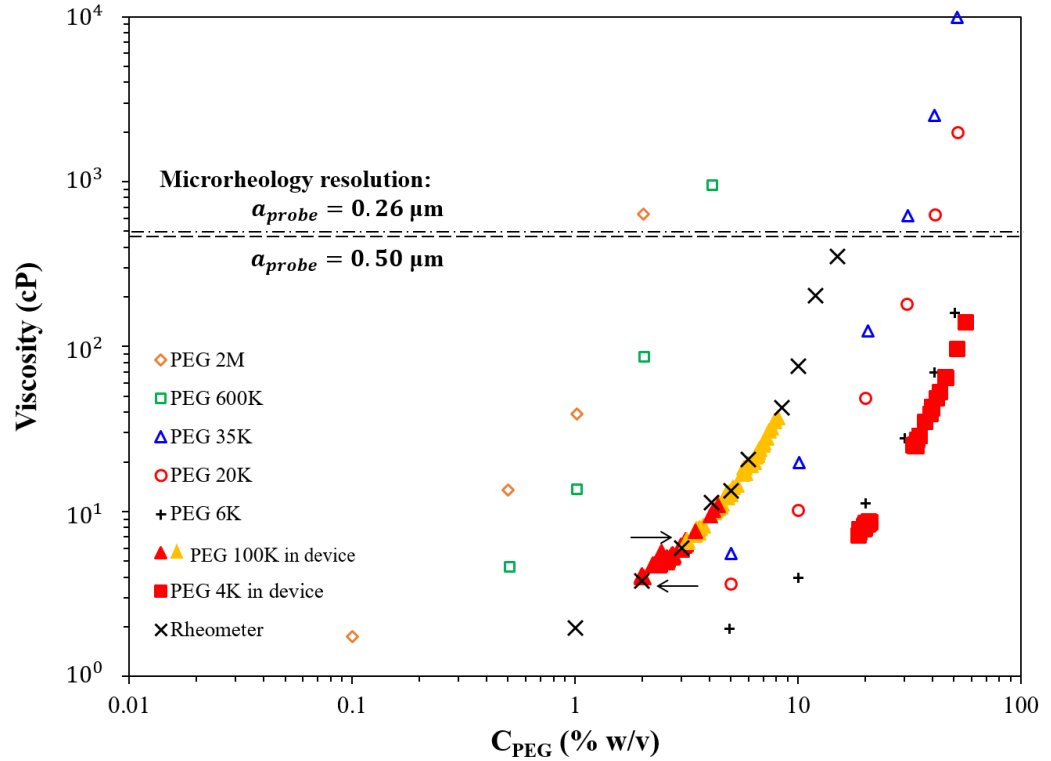


Figure 3.4 Viscosity of concentrating 4 kg/mol (filled squares) and 100 kg/mol (filled triangles) PEG solutions are quantified inside shrinking droplets using MPT. For 100 kg/mol PEG, two devices (red and yellow filled triangles) are used with loading concentrations indicated by the arrows. The black crosses are bulk measurements for 100 kg/mol PEG. The open symbols indicate results obtained from Natalia et al. (2011). Each symbol represents a specific molecular weight. The top two dotted lines show the microrheology resolution for 0.26 μm and 0.50 μm probes, respectively.

The two arrows indicate the PEG loading concentration for each device. The two sets of data collapse on top of each other, indicating high reproducibility of the results and the continuous data points illustrate high compositional resolution. The microfluidic results are consistent with the macroscopic measurements obtained

using a rheometer, which are represented by the black crosses. The two horizontal dotted lines represent the calculated maximum viscosities that can be measured by the 0.26 μm and 0.50 μm probes, respectively. Using our low concentration data, the intrinsic viscosity of 100 kg/mol PEG is determined based on the Huggins equation by extrapolating the reduced viscosity ($\frac{\eta_{sp}}{C}$) to zero solute concentration shown as Eqn. (3.3),

$$\frac{\eta_{sp}}{C} = [\eta] + K_H[\eta]^2 C \quad , \quad (3.3)$$

where C is the concentration, η_{sp} is the specific viscosity, which is calculated based on our viscosity measurements. $[\eta]$ is the intrinsic viscosity and K_H is the Huggins constant [38]. The intrinsic viscosity is determined to be $80.1 \frac{\text{mL}}{\text{g}}$. This is consistent with the value calculated from the Mark-Houwink equation using the tabulated constants $K = 0.01192 \frac{\text{mL}}{\text{g}}$ and $a = 0.76$, [39] which is $75.2 \frac{\text{mL}}{\text{g}}$. The small deviation arises from the polydispersity of the PEG molecules. The same measurement is performed for 4 kg/mol PEG in one microfluidic device, which is represented by the filled red squares. The microfluidic results for 4 kg/mol and 100 kg/mol PEG are compared with the work by Natalia *et al.* (2011), [40] in which PEG of a range of molecular weights from 6k to 20 Mg/mol are studied. Each molecular weight is represented by the open symbols in Figure 3.4 and is specified by the legend. As shown in Figure 3.4, the viscosities for both 4 kg/mol and 100 kg/mol measured in the device increase exponentially with concentration, which are consistent with other molecular weights from the literature. In addition, our results follow the trend that at a given PEG concentration, the larger the molecular weight, the higher the

viscosity. Overall, we have demonstrated that the viscosity of concentrating PEG solutions can be accurately quantified in the microfluidic device.

3.4.4 Viscosity measurements of proteins in shrinking droplets

The microfluidic approach is extended to protein systems. In this work, the viscosity of two globular proteins BSA and lysozyme are characterized, which are represented by the circles and diamonds, respectively, in Figure 3.5. The proteins are dissolved in deionized water and the pH is not controlled. For each protein,

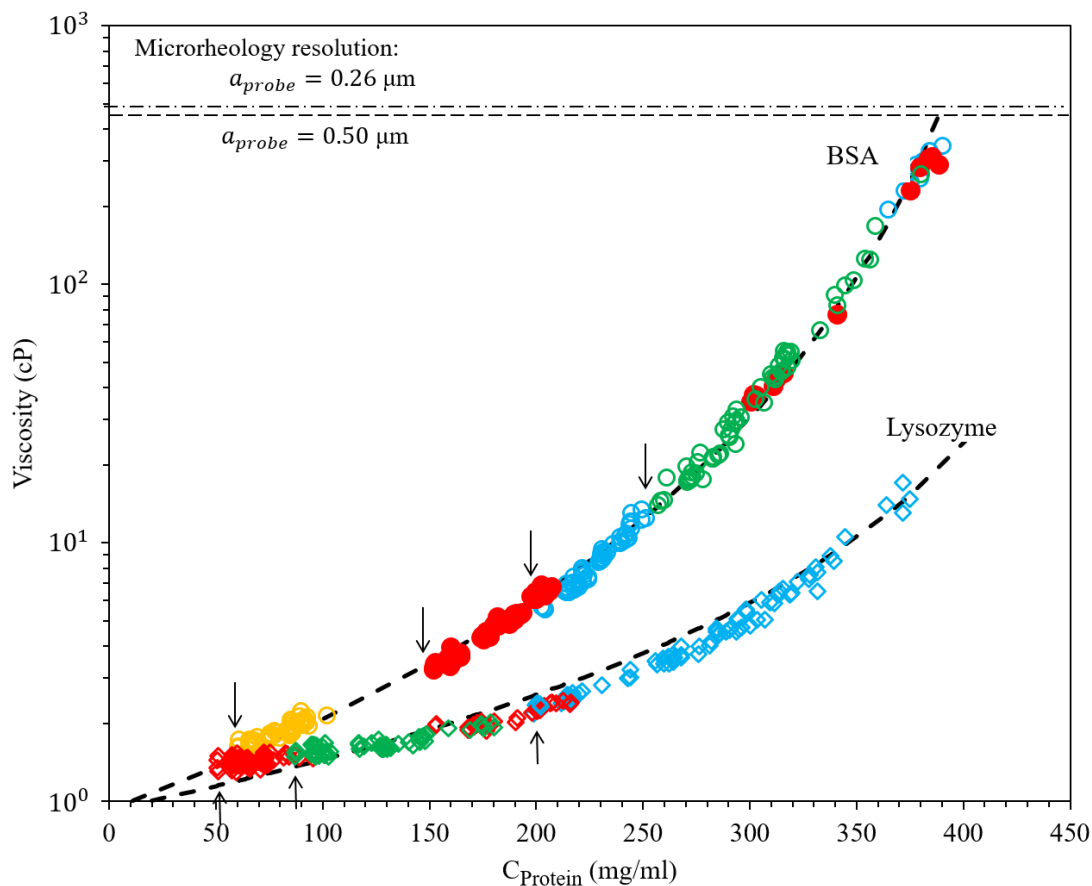


Figure 3.5 Concentration-dependence of viscosity for BSA (circles) and lysozyme (diamonds) are quantified in the microfluidic device. For each protein, multiple devices are used to cover the entire concentration range from 50 to 400 mg/ml. Each color represents one device, with the loading concentration indicated by the arrow. The two bold dotted lines represent the best-fit to the Krieger-Dougherty model for each protein. The top two dotted lines show the microrheology resolution for 0.26 μm and 0.50 μm probes, respectively.

three to four devices are used to cover the concentration range from 50 to 400 mg/mL, which only requires roughly 150 μ L of protein solution in total. Each color represents one device with the loading concentration indicated by the arrow. For convenience, each experiment is usually performed for 8-10 hours, during which the solute is concentrated by 1.5-2 times under the current lab condition. We can extend the experimental time or increase the dehydration rate to cover a wider concentration range. As discussed in the ‘Design Space of Device’ section, the concentration of the solute can increase by 15 or 30 times depending on the size of the probes. The filled red circles illustrate the results obtained after a 15 hour dehydration, in which the solute is concentrated by roughly 2.7 times, and more than two orders of magnitude of viscosity is covered by a single device. Since the data was taken before and after the overnight dehydration, there is a gap in the filled red circles, but the key here is to show that the range of concentration covered by a device can be expanded by adjusting the experimental conditions. For each protein, the results obtained from different devices overlap well, indicating reproducibility of the measurements.

The device-quantified concentration dependence of viscosity for the two proteins are fitted to the Krieger-Dougherty Model shown as Eqn. (3.4), [41]

$$\eta = \eta_0 \left(1 - \frac{\phi}{\phi_m}\right)^{-[\eta]\phi_m} \quad , \quad (3.4)$$

where ϕ is the volume fraction of the protein molecule, η_0 is the viscosity of solvent (in this case water), $[\eta]$ is the intrinsic viscosity and ϕ_m is the maximum packing parameter. ϕ_m is 0.74 and 0.6 for monodisperse spheres and random

packing respectively. [42] Since the intrinsic viscosity can be easily measured and determined based on the Huggins equation, when applying the Krieger-Dougherty model to our data, the intrinsic viscosity is fixed and only ϕ_m is fitted. The intrinsic viscosity for BSA and lysozyme are measured as $5.3 \frac{mL}{g}$ and $3.2 \frac{mL}{g}$, respectively. The best-fit results are plotted as the bold dotted lines for each protein as shown in Figure 3.5. ϕ_m is determined to be 0.62 for BSA, which is close to the random-close packing limit for monodisperse hard spheres. [43] Sharma *et al.* (2011) and Prasad *et al.* (2013) also successfully fit BSA viscosity with the Krieger-Dougherty model up to 250 mg/mL at pH 7.4. [20, 31] For lysozyme, ϕ_m is determined to be 0.60, which is also reasonable. However, the Krieger-Dougherty model fits less well, suggesting that lysozyme involves more complicated intermolecular interactions, such as strong short-range attraction in addition to the electrostatic repulsion, [44] which has been demonstrated to affect the viscosity of the lysozyme solution by Liu *et al.* (2010), [45] and this is not accounted in the colloidal models. Godfrin *et al.* (2015) observed deviation between experimental data and hard sphere predictions for lysozyme at volume fractions larger than 0.15. [46] Overall, we have demonstrated that the droplet-based microfluidic device is able to quantify viscosity as a function of concentration for polymer and protein systems with microliters of sample and high compositional resolution.

3.5 Discussion

The microfluidic device accompanied with multiple particle tracking microrheology has been demonstrated to be a valuable tool to quantify viscosity of protein solutions. Figure 3.5 shows that only microliters of sample solutions (~ mg of proteins) is required to measure an 8 times increase in concentration and two orders of magnitude increase in viscosity, which is a great advantage for precious protein-based drugs, especially for formulation optimization during the early stage of development. Compared to the discrete points obtained from macroscopic experiments, the high compositional resolution is another advantage of the device, which depends on the frequency of the viscosity scan, size of the device and the evaporation rate. The slow rate of water partition provides a mass transfer Biot number on the order of 10^{-4} , which minimizes the concentration gradient inside the droplet.

Several design constraints need to be considered when performing viscosity measurements using this device. First, droplet diameters are required to be larger than the height of the trap in order to maintain the pancake-shape volume, which affects the extent of droplet shrinking. This can be improved by using droplet traps with larger diameters. Second, the concentration of the probes needs to be chosen carefully to provide good statistics for the MSD calculation. Meanwhile, the probe particles concentration needs to be maintained lower than 0.01 during droplet shrinking to prevent brightness saturation, [36] which also affects the extent of droplet shrinking and the increase in solute concentration. Additionally, proteins are surface active, to avoid significant depletion effect, the loading concentration

cannot be too low otherwise the assumed initial concentration in the droplet will be incorrect. With a surface concentration of $2 \text{ mg}/\text{m}^2$ for globular proteins, [47] the amount of proteins adsorbed onto the drop interface is negligible for all loading concentrations in this work. The surface coverage concentration of different proteins varies between $1\text{-}3 \text{ mg}/\text{m}^2$, [47, 48] therefore, the loading concentration is recommended to be larger than $1 \text{ mg}/\text{ml}$ to guarantee that the effect of surface depletion on the calculated concentration is less than 10%. Finally, the probe particles must remain suspended in the droplet for MPT. To avoid rapid sedimentation or buoyancy during the viscosity measurement, both probe size and the droplet density changes during droplet shrinking need be considered. The calculated settling velocity can be used to estimate the traveling time through the height of the droplet ($\sim 100 \text{ }\mu\text{m}$). In this work, the device is slowly rotated on a rotator between viscosity scans to prevent probes from sedimenting. In addition, particle interactions need to be avoided to obtain accurate MPT measurements. Proteins, such as monoclonal antibodies, have been demonstrated to have higher tendency to induce tracer particle aggregations. [23, 49] The surface chemistry of the particles can be modified or molecules can be grafted to the particle surface to generate electrostatic or steric repulsions between particles and prevent particle interactions. [23, 37] In future work, automatic data acquisition for viscosity measurements will be developed, which will enable data to be captured for the entire 24 hour droplet shrinking process and cover a larger increase in concentration using one device.

3.6 Conclusions

In this chapter, we have shown that the developed droplet-based microfluidic device is able to quantify viscosity using MPT for protein solutions as a function of concentration with high compositional resolution. Only a few microliters of sample is needed to cover nearly a decade increase in concentration and several orders of magnitude increase in viscosity. MPT is validated by measuring the viscosity of glycerol at various concentrations in a glass chamber. We have shown that the viscosity can be accurately quantified from water up to 250 cP by showing consistency with macroscopic measurements. Then the viscosities measured inside the droplets are shown to be consistent with those taken in a glass chamber, which indicates that there is no significant confinement effect of the oil/water interface on the viscosity measurements. Finally, the concentration dependence of viscosity are quantified inside shrinking droplets for two different molecular weight PEG, BSA and lysozyme. The intrinsic viscosity of 100 kg/mol PEG is extrapolated from the measured viscosities using the Huggins method, which are consistent with the calculated values based on the Mark-Houwink equation. The best-fit ϕ_m based on the Krieger-Dougherty model is reasonable for both BSA and lysozyme. Overall, we have shown the applicability of the developed device on characterizing viscosity as a function of concentration for protein solutions with small sample volumes. Continuous data points have the potential to provide complimentary work for theoretical modeling. This the first time that the microfluidic shrinking droplets are combined with MPT. This technique will be further extended to quantify viscosity of more complex proteins and will be applied

to characterize the effects of different excipients and multiple formulation factors, such as pH, ionic strength, on the viscosity of protein solutions.

3.7 *Reference*

1. Sauna ZE, Lagassé HAD, Alexaki A, Simhadri VL, Katagiri NH, Jankowski W, Kimchi-Sarfaty C (2017) Recent advances in (therapeutic protein) drug development. F1000Research.
2. Du W, Klibanov AM (2011) Hydrophobic salts markedly diminish viscosity of concentrated protein solutions. *Biotechnol Bioeng* 108:632–636
3. Inoue N, Takai E, Arakawa T, Shiraki K (2014) Arginine and lysine reduce the high viscosity of serum albumin solutions for pharmaceutical injection. *J Biosci Bioeng* 117:539–543
4. Shire SJ, Shahrokh Z, Liu J (2004) Challenges in the development of high protein concentration formulations. *J Pharm Sci* 93:1390–1402
5. Harris RJ, Shire RJ, Winter C (2004) Commercial manufacturing scale formulation and analytical characterization of therapeutic recombinant antibodies. *Drug Dev Res* 61:137–154
6. Berteau C, Filipe-Santos O, Wang T, Roja HE, Granger C, Schwarzenbach F (2015) Evaluation of the impact of viscosity, injection volume, and injection flow rate on subcutaneous injection tolerance. *Med Devices Evid Res* 8:473–484
7. Liu J, Nguyen MDH, Andya JD, Shire SJ (2005) Reversible self-association increases the viscosity of a concentrated monoclonal antibody in aqueous solution. *J Pharm Sci* 94:1928–1940
8. Johnson HR, Lenhoff AM (2013) Characterization and suitability of therapeutic antibody dense phases for subcutaneous delivery. *Mol Pharm* 10:3582–3591
9. Daugherty AL, Mersny RJ (2006) Formulation and delivery issues for monoclonal antibody therapeutics. *Adv Drug Deliv Rev* 58:686–706
10. Braun A, Kwee L, Labow MA, Alsenz J (1997) Protein aggregates seem to play a key role among the parameters influencing the antigenicity of interferon alpha (IFN- α) in normal and transgenic mice. *Pharm Res* 14:1472–1478
11. Koren E, Zuckerman L, Mire-Sluis A (2005) Immune Responses to Therapeutic Proteins in Humans - Clinical Significance, Assessment and Prediction. *Curr Pharm Biotechnol* 3:349–360
12. Cleland JL, Powell MF, Shire SJ (1993) The development of stable protein

formulations: A close look at protein aggregation, deamidation, and oxidation. *Crit Rev Ther Drug Carrier Syst* 10:307–377

13. Chari R, Jerath K, Badkar A V., Kalonia DS (2009) Long- and short-range electrostatic interactions affect the rheology of highly concentrated antibody solutions. *Pharm Res* 26:2607–2618
14. Hong T, Iwashita K, Shiraki K (2018) Viscosity Control of Protein Solution by Small Solutes: A Review. 0:746–758
15. Wang S, Zhang N, Hu T, Dai W, Feng X, Zhang X, Qian F (2015) Viscosity-Lowering Effect of Amino Acids and Salts on Highly Concentrated Solutions of Two IgG1 Monoclonal Antibodies. *Mol Pharm* 12:4478–4487
16. Inoue N, Takai E, Arakawa T, Shiraki K (2014) Arginine and lysine reduce the high viscosity of serum albumin solutions for pharmaceutical injection. *J Biosci Bioeng* 117:539–543
17. Kanai S, Liu J, Patapoff TW, Shire SJ (2008) Reversible self-association of a concentrated monoclonal antibody solution mediated by fab-fab interaction that impacts solution viscosity. *J Pharm Sci* 97:4219–4227
18. Yadav S, Shire SJ, Kalonia DS (2010) Factors Affecting the Viscosity in High Concentration Solutions of Different Monoclonal Antibodies. *J Pharm Sci* 99:4812–4829
19. Inoue N, Takai E, Arakawa T, Shiraki K (2014) Specific decrease in solution viscosity of antibodies by arginine for therapeutic formulations. *Mol Pharm* 11:1889–1896
20. Sharma V, Jaishankar A, Wang YC, McKinley GH (2011) Rheology of globular proteins: Apparent yield stress, high shear rate viscosity and interfacial viscoelasticity of bovine serum albumin solutions. *Soft Matter* 7:5150–5160
21. Yadav S, Shire SJ, Kalonia DS (2011) Viscosity analysis of high concentration bovine serum albumin aqueous solutions. *Pharm Res* 28:1973–1983
22. Castellanos MM, Pathak JA, Colby RH (2014) Both protein adsorption and aggregation contribute to shear yielding and viscosity increase in protein solutions. *Soft Matter* 10:122–131
23. Josephson LL, Furst EM, Galush WJ (2016) Particle tracking microrheology of protein solutions. *Cit J Rheol* 60:531

24. Kim S, Kim KC, Yeom E (2018) Microfluidic method for measuring viscosity using images from smartphone. *Opt Lasers Eng* 104:237–243
25. Wang G, Tan C, Li F (2017) A contact resonance viscometer based on the electromechanical impedance of a piezoelectric cantilever. *Sensors Actuators A Phys* 267:401–408
26. Connolly BD, Petry C, Yadav S, Demeule B, Ciaccio N, Moore JMR, Shire SJ, Gokarn YR (2012) Weak Interactions Govern the Viscosity of Concentrated Antibody Solutions: High-Throughput Analysis Using the Diffusion Interaction Parameter. *Biophys J* 103:69–78
27. Yadav S, Shire SJ, Kalonia DS (2012) Viscosity Behavior of High-Concentration Monoclonal Antibody Solutions: Correlation with Interaction Parameter and Electroviscous Effects. *J Pharm Sci* 101:998–1011
28. Woldeyes MA, Qi W, Razinkov VI, Furst EM, Roberts CJ (2019) How Well Do Low- and High-Concentration Protein Interactions Predict Solution Viscosities of Monoclonal Antibodies? *J Pharm Sci* 108:142–154
29. Foffi G, Savin G, Bucciarelli S, Dorsaz N, Thurston GM, Stradner A, Schurtenberger P (2014) Hard sphere-like glass transition in eye lens α -crystallin solutions. *Proc Natl Acad Sci U S A* 111:16748–16753
30. Heinen M, Zanini F, Roosen-Runge F, et al (2012) Viscosity and diffusion: Crowding and salt effects in protein solutions. *Soft Matter* 8:1404–1419
31. Sarangapani PS, Hudson SD, Migler KB, Pathak JA (2013) The limitations of an exclusively colloidal view of protein solution hydrodynamics and rheology. *Biophys J* 105:2418–2426
32. Wehrman MD, Leduc A, Callahan HE, Mazzeo MS, Schumm M, Schultz KM (2018) Rheological properties and structure of step- and chain-growth gels concentrated above the overlap concentration. *AIChE J* 64:3168–3176
33. Breedveld V, Pine DJ (2003) Microrheology as a tool for high-throughput screening. *J Mater Sci* 38:4461–4470
34. Wehrman MD, Lindberg S, Schultz KM (2018) Multiple particle tracking microrheology measured using bi-disperse probe diameters. *Soft Matter* 14:5811–5820
35. Swan JW, Brady JF (2010) Particle motion between parallel walls: Hydrodynamics and simulation. *Phys Fluids* 22:103301
36. McGlynn JA, Wu N, Schultz KM (2020) Multiple particle tracking

microrheological characterization: Fundamentals, emerging techniques and applications. *J Appl Phys* 127:201101

37. Furst EM, Squires TM. *Microrheology*. Oxford University Press; 2017.
38. Huggins ML (1942) The Viscosity of Dilute Solutions of Long-Chain Molecules. IV. Dependence on Concentration. *J Am Chem Soc* 64:2716–2718
39. Schubert D. (2000) *Kirk-Othmer Encyclopedia of Chemical Technology*. Kirk-Othmer Encycl Chem Technol. 1-68.
40. Zębacz N, Wieczorek SA, Kalwarczyk T, Fiałkowski M, Hołyst R (2011) Crossover regime for the diffusion of nanoparticles in polyethylene glycol solutions: Influence of the depletion layer. *Soft Matter* 7:7181–7186
41. Krieger IM, Dougherty TJ (1959) A Mechanism for Non-Newtonian Flow in Suspensions of Rigid Spheres. *Trans Soc Rheol* 3:137–152
42. Quemada D, Berli C (2002) Energy of interaction in colloids and its implications in rheological modeling. *Adv Colloid Interface Sci* 98:51–85
43. Donev A, Cisse I, Sachs D, Variano EA, Stillinger FH, Connelly R, Torquato S, Chaikin PM (2004) Improving the Density of Jammed Disordered Packings Using Ellipsoids. *Science* (80-) 303:990–993
44. Zhang Z, Liu Y (2017) Recent progresses of understanding the viscosity of concentrated protein solutions. *Curr Opin Chem Eng* 16:48–55
45. Liu J, Thompson ZJ, Sue HJ, Bates FS, Hillmyer MA, Dettloff M, Jacob G, Verghese N, Pham H (2010) Toughening of epoxies with block copolymer micelles of wormlike morphology. *Macromolecules* 43:7238–7243
46. Godfrin PD, Hudson SD, Hong K, Porcar L, Falus P, Wagner NJ, Liu Y (2015) Short-Time Glassy Dynamics in Viscous Protein Solutions with Competing Interactions. *Phys Rev Lett* 115:228302
47. Beverung CJ, Radke CJ, Blanch HW (1999) Protein adsorption at the oil/water interface: characterization of adsorption kinetics by dynamic interfacial tension measurements. *Biophys Chem* 81:59–80
48. T S, S D (1998) A New Methodology for Studying Protein Adsorption at Oil-Water Interfaces. *J Colloid Interface Sci* 206:407–415
49. T G, A S (2019) Synthesis and application of PEGylated tracer particles for measuring protein solution viscosities using Dynamic Light Scattering-based microrheology. *Colloids Surf B Biointerfaces* 181:516–523

Chapter 4: Systematic quantification of the effects of pH and ionic strength on the viscosity of highly concentrated BSA solutions

4.1 Introduction

Viscosity control is essential for the manufacturing and administration of high concentration therapeutic proteins. The viscosity of the concentrated protein solutions is sensitive to the formulation conditions, such as protein concentrations, temperature, pH, ionic strength, and excipients. [1, 2] These formulation factors correlate with each other, generating a complicated multi-component system. In addition, the viscosity shows non-monotonic dependence on several parameters, such as pH, and salt concentration, [3, 4] complicating the selection of the optimum formulation conditions. Therefore, being able to accurately and efficiently quantify the viscosity of protein solutions over a wide range of practical formulation conditions is critical for the viscosity control and the development of protein-based drugs.

Limited availability of protein-based drugs induces challenges in viscosity quantification. Experimental methods for viscosity quantification have been developed with the intent of reducing the sample volume required for viscosity measurements. Hirschman *et al.* (2021) developed a thin gap rheometry, which minimizes the artifacts due to protein adsorption at the air-water interface, to successfully quantify the viscosity of high concentration mAb solutions with reduced sample volume ($\sim\mu\text{L}$) and over a wide range of shear rates. [5] Dharmaraj *et al.* (2016) applied a microcapillary rheometer to examine the rheology of lysozyme solution over a range of parameter spaces including temperature,

concentration, and shear rates. [6] However, these experimental methods can only provide discrete data covering a limited parameter space.

Molecular simulation with coarse-grained models has been developed to investigate the relationship between protein-protein interactions (PPIs) and the viscosity of mAbs over a range of concentrations. [7] Schwenger *et al.* (2019) developed a model by combining the Ross-Minton model with modified Arrhenius temperature dependence to capture the viscosity of mAbs over varying temperatures and concentrations. [8] To improve the robustness and extend the applicability of the developed models for viscosity prediction over a wide range of formulation parameter space, a large number of continuous experimental data is required for parameter fitting. Computational methods have been applied to develop tools to fast screen the well-behaved mAbs from a large number of potential candidates based on the easily obtainable sequence or structural molecular descriptors. Sharma *et al.* developed a model equation to predict the viscosity of mAb based on their net charge, charge dipole distribution, and hydrophobicity, which can be obtained by antibody sequence and molecular dynamic simulations. [9] Agrawal *et al.* present a spatial charge map (SCM) tool to accurately identify the high-viscosity antibodies solely based on their sequence. [10] Recently, machine learning has been applied to select the molecular descriptors for viscosity prediction. Lai *et al.* developed a decision tree model to classify the low- and high-viscosity mAbs among 27 mAbs based on the net charges and a high viscosity index, which are selected based on machine learning. [11] In addition, machine learning regression methods and classification methods have been applied to predict the

aggregation rates of mAbs. [12] Among all these works, experimental data is applied to test the effectiveness of the molecular descriptors and define their threshold values. Also, the accuracy of the predictive model and classification is affected by the experimental uncertainty. However, only discrete experimental data with large uncertainties are provided in the literature. Therefore high compositional data covering a large parameter space is highly demanded.

In the last chapter, we have demonstrated that the developed droplet-based microfluidic device incorporated with MPT is able to quantify the concentration dependence of viscosity for protein solutions up to 400 mg/mL. More than 2 orders of magnitude increase in viscosity were covered with only a few microliters of sample, and data with high compositional resolution is provided. [13] The goal of this chapter is to extend our previous study by increasing the number of parameters in the system. In this work, the viscosity of BSA is quantified as a function of BSA concentration, and ionic strength at three different values of pH using the droplet-based microfluidic device. The high resolution in concentration and ionic strength can provide operation regimes for specific formulation requirements. Caffeine is added to the BSA solution to investigate underlying interaction mechanisms between BSA molecules.

4.2 *Materials and Methods*

4.2.1 *Materials*

Sodium acetate is obtained from Sigma Aldrich (St. Louis, MO) (Product No.: S-8750). Acetic acid is obtained from Thermo Fisher Scientific (Waltham, MA) (Catalog No.: A35-500). Bovine Serum Albumin (BSA) is purchased from Sigma-Aldrich (Catalog No.: A7030). Caffeine is obtained from Sigma Aldrich.

4.2.2 *Preparation of BSA solutions*

Acetic acid-sodium acetate buffer is prepared with appropriate buffer concentrations and molar ratios of the conjugate acid to base in order to achieve desired ionic strengths and pH. Change in the acid-base equilibrium constant due to the variation in solution ionic strength is accounted during the buffer calculation. An appropriate amount of lyophilized BSA powder is dissolved in the buffer solutions or deionized water (18.2 M Ω .cm) in a volumetric flask to reach the concentration of 250 mg/mL. For BSA solutions made in DI, the pH is determined as 6.6 and the ionic strength is adjusted by adding an appropriate amount of NaCl. During droplet dehydration, the increase in ionic strength induces a less than 0.2 pH unit change, which is negligible. The solution ionic strength in this work refers to the contribution from the buffer species. Caffeine is dissolved at a concentration of 15 mg/mL in buffer solution and is then well-mixed with BSA powder before using.

4.2.3 Quantification of viscosity vs. concentration of BSA solutions in the microfluidic device

The concentration dependence of viscosity for BSA solutions at various pHs and ionic strengths are measured using the droplet-based microfluidic device. Aqueous droplets of dilute and well-mixed sample solution are generated in the channel traps and are surrounded by mineral oil. The device fabrication and droplet generation are discussed in Chapter 2. The dehydration process of all 40 droplets is tracked under the microscope. The solution viscosity is quantified by multiple particle tracking microrheology (MPT) along the concentration process. The measurements of concentration dependence of viscosity in the shrinking droplets are thoroughly discussed in Chapter 3.3. Droplets are dehydrated at room temperature ($22 \pm 1^\circ\text{C}$). A typical time for complete droplet shrinking is approximately 24 - 30 h under the current lab conditions, which is slow enough to minimize concentration gradients inside the droplet. In this work, as droplets shrink, the concentrations of BSA and all ionic species in the buffer solution increase by the same fold, which results in an increase in the solution ionic strength and a constant molar ratio of each ionic species to BSA. Since the ionic strength depends linearly on the concentration of each ionic species, the ratio of ionic strength to BSA concentration is also constant, which is defined as ξ . This work includes five different values of ξ , 0, 0.06, 0.3, 0.6, and 0.8, which correspond to five different initial buffer ionic strength, 0 mM, 15 mM, 75 mM, 150 mM and 200 mM, respectively.

For MPT measurements, carboxylated, fluorescently labeled polystyrene probe particles with a radius of $0.26 \pm 0.007 \mu\text{m}$ are dispersed in the solution with

a concentration of 0.036% solids per volume and undergo Brownian motion. There is a possibility that the BSA molecules adsorb on the surface of the particles. Since the pegylated probes are not effective to prevent aggregation in the solution conditions studied in this work, unpegylated probes particles are used. No aggregation is observed among the probes, which could be stabilized by the adsorbed BSA molecules. We have demonstrated that the BSA adsorption doesn't affect the MPT measurements. The movement of the probes is measured at 40 fps for 30s with 10 ms exposure time and is used to calculate the viscosity. The methodology of MPT has been explained in Chapter 2.4. All of our measurements are of diffusive particle motion, $\alpha = 1$.

4.2.4 Microscopy

An inverted Nikon Ti-U microscope at 10 \times magnification and a pco.panda 4.2 camera (0.65 $\mu\text{m}/\text{pixel}$) are used to track droplet dimensions during shrinking under bright field conditions. The MS-2000 XY translational stage (Applied Scientific Instrumentation; Lane county, OR) of the microscope is controlled by Micro-Manager software, which enables the automatic scanning of the entire device. MPT experiments are conducted using the same microscope and camera at 60 \times magnification (0.11 $\mu\text{m}/\text{pixel}$) with an ultraviolet (UV) light source (X-cite 120 lamp) and a FITC filter set. All measurements are conducted at room temperature ($22 \pm 1^\circ\text{C}$).

4.2.5 Zeta potential measurements

Zeta potential measurements are performed using a Zetasizer Nano ZS (Malvern, Houston, TX) at 23 $^\circ\text{C}$. The zeta potential is measured at a BSA

concentration of 12.5 mg/mL with ionic strength of 15 mM using a DTS 1070 clear folded capillary cell. The Smoluchowski method is chosen in the software for the zeta potential measurements.

4.3 Results and Discussions

Figure 4.1 shows data for nine different experiments in the form that data is collected. For each device, data is collected on multiple drops providing a nearly continuous curve of viscosity versus concentration of BSA. Figure 4.1a, b, and c represent the concentration dependence of viscosity for BSA quantified at three different values of pH 6.6, 5.0, and 3.9, respectively, with various ionic strengths. For each value of pH, different symbols represent a single dehydration experiment with a constant ξ , which is defined as the ratio of ionic strength to BSA concentration. The circles, squares, diamonds, triangles, and inverted triangles represent ξ of 0, 0.06, 0.3, 0.6, and 0.8, respectively. The arrow indicates the direction of increasing ξ , which corresponds to the increase in ionic strength. At pH 6.6, the viscosity of BSA solution decreases as ionic strength increases at a constant BSA concentration. While no effect and the opposite trend of increasing ionic strength on the viscosity is observed for pH 5.0 and pH 3.9, respectively. In addition, the viscosity increases less dramatically with BSA concentration at pH 5.0, compared to the other two values of pH. For each dehydration experiment, the concentration dependence of viscosity for BSA is quantified from 250 mg/mL to approximately 400 mg/mL, which is nearly a 1.5 fold increase. Meanwhile, the concentration of all ionic species in the buffer increases with the same fold as BSA.

Therefore, the ionic strength is also changing during these experiments, but the composition at each point is known. Less than a milliliter of BSA solution is required to perform all nine droplet dehydration experiments in Figure 4.1, which

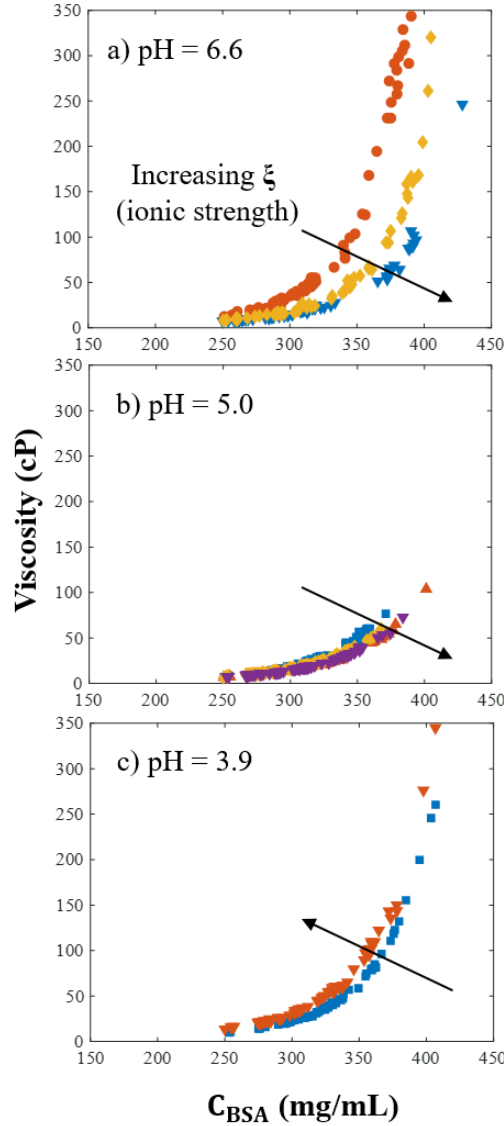


Figure 4.1 The viscosity of BSA solution as a function of BSA concentration at pH 6.6 (a), pH 5.0 (b), and pH 3.9 (c) with various ionic strengths. Each symbol represents a constant ratio of ionic strength to BSA concentration, ξ . The circles, squares, diamonds, triangles, and inverted triangles represent ξ of 0, 0.06, 0.3, 0.6, and 0.8, respectively.

provide data in viscosity with high compositional resolution covering a multi-dimensional parameter space, including BSA concentration, pH, and ionic strength.

Comparing the data in Figure 4.1 to typical data in the literature is complicated by the fact that ionic strength varies with protein composition.

These continuous multi-dimensional data can be represented as surface plots. Surface plots clarify that both protein concentration and ionic strength change across these data sets, but the near continuous nature of data allows slices (planes)

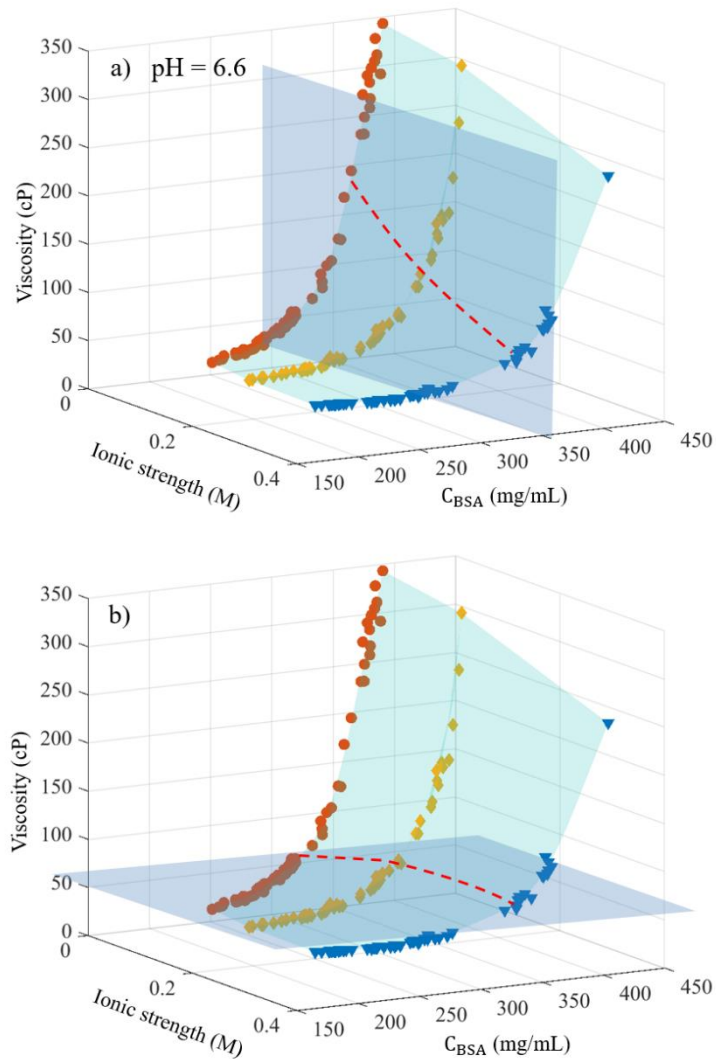


Figure 4.2 Viscosity of BSA solution as a function BSA concentration and ionic strength at pH 6.6. The shaded area represents the surface plot generated based on the three data sets. The shaded rectangle in a) shows the plane cut of constant BSA concentration at 350 mg/mL, and in b) shows the plane cut of constant viscosity of 50 cP. The red dotted line represents a) iso-concentration line and b) iso-viscosity line, which are drawn to guide the eyes.

to be taken for comparison to literature and extract viscosity at specific formulation conditions. Figure 4.2a shows the viscosity of BSA as a function of BSA concentration and ionic strength at pH 6.6, composed of data taken from Figure 4.1a. The shaded area illustrates the surface, which is generated based on the three data sets at various ionic strengths. Similar surface plots can be obtained for pH 5.0 and 3.9, respectively. The continuous nature of data enables the interpolation of parameters, which allows parameterization of data and simple extraction of viscosity at specific conditions. For a dosage-based formulation, for example at BSA concentration of 350 mg/mL, the viscosity as a function of ionic strength at pH 6.6 can be obtained by cutting a plane at 350 mg/mL, which is represented by the blue shaded rectangle in Figure 4.2a. The three intersection points are linearly interpolated based on the continuous data points. The red dotted line represents the iso-concentration line, which is drawn to guide the eyes. Similarly, the iso-concentration lines can be obtained for pH 5.0 and 3.9 from the corresponding surface plots.

Figure 4.3 shows the iso-concentration lines for all three values of pH at a fixed BSA concentration of 350 mg/mL. The circles, diamonds, and squares represent the viscosity of BSA as a function of ionic strength at 350 mg/mL for pH 6.6, 5.0 and 3.9, respectively. The viscosity of BSA can be reduced by increasing the ionic strength at pH 6.6 and 5.0, while an opposite trend is observed at pH 3.9. Therefore, based on our results, increasing ionic strength is an effective approach to decrease viscosity for pH 6.6, while formulations with high ionic strengths should be screened out for pH 3.9.

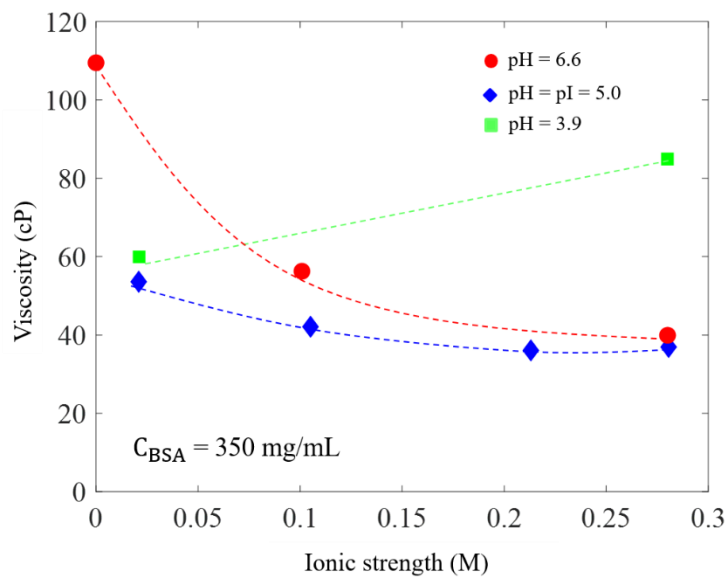


Figure 4.3 Viscosity of BSA as a function of ionic strength at pH 6.6 (red circles), 5.0 (blue diamonds), and 3.9 (green squares) at 350 mg/mL obtained from the plane cuts of constant BSA concentration. The dotted lines represent iso-concentration lines and are drawn to guide the eyes.

These multi-dimensional data points can also provide the operating regime for formulations with maximum viscosity requirements. For example, 50 cP is the threshold value for the subcutaneous injection. [14] The shaded blue area in Figure 4.2b indicates a plane cut of constant viscosity of 50 cP, which provides BSA concentration as a function of ionic strength at pH 6.6. Similarly, the three intersection data points are linearly interpolated based on the continuous data points. The red dotted line represents the iso-viscosity line. Figure 4.4 shows the iso-viscosity lines for the three different values of pH 5.0, pH 3.9, and pH 6.6 as a function of ionic strength. Figure 4.4 provides a tool to design formulations based on a constraint like viscosity. At pH 6.6, by increasing the ionic strength to 0.28 M, the BSA concentration can be increased from nearly 317 mg/mL to 365 mg/mL, which still satisfies the 50 cP threshold value for the subcutaneous injection. At ionic strength of 0.28 M, by adjusting the pH from 3.9 to 5.0, the maximum BSA

concentration can be increased from approximately 325 mg/mL to 365 mg/mL. Figure 4.4 provides the operating regimes for formulations aiming to increase the BSA concentration meanwhile maintain the viscosity below a threshold value. Overall, we have demonstrated that the multi-dimensional data with high

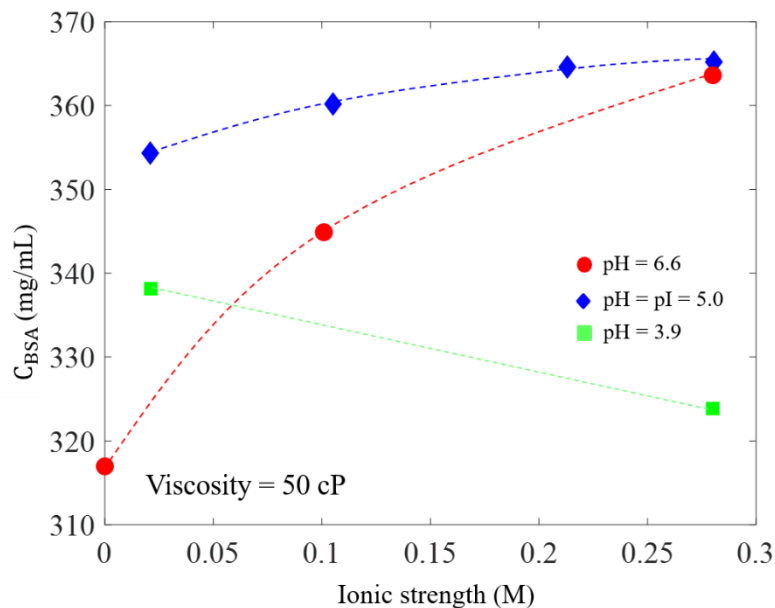


Figure 4.4 Concentration of BSA as a function of ionic strength at pH 6.6 (red circles), 5.0 (blue diamonds) , and 3.9 (green squares) at 50 cP obtained from the plane cuts of constant viscosity. The dotted lines represent iso-viscosity lines and are drawn to guide the eyes.

compositional resolution has the potential to provide guidance for various formulation requirements with small sample volumes.

In addition, the results provide insights into the nature of intermolecular interactions of BSA involved under various solution conditions. As shown in Figure 4.3, at 350 mg/mL, the viscosity of BSA decreases by nearly 60% as ionic strength increases to 0.28 M at pH 6.6. While a lower reduction and a slight increase in viscosity are observed with the same extent of increase in ionic strength at pH 5.0 and pH 3.9, respectively. The isoelectric point, pI, of BSA is known to be near pH

5.0. [15] To verify this in the sample used here, the zeta potential is measured as a function of pH and shown in Figure 4.5. BSA has nearly zero net charge at pH 5.0, which is consistent with the reported value. At pH 5.0, we expect the electrostatic interactions between the protein molecules to be nearly zero, so that increasing ionic strength has insignificant effect on the viscosity is expected. At pH 6.6, BSA

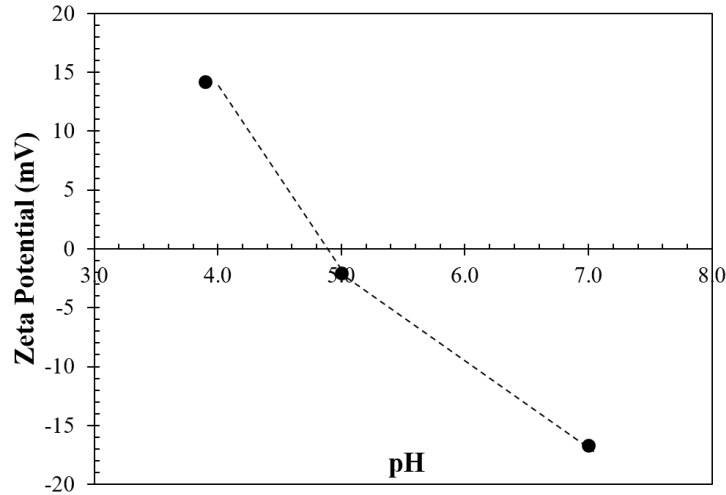


Figure 4.5 Zeta potential of BSA solution as a function of pH at 15 mM ionic strength.

is negatively charged. Increasing ionic strength suppresses the electrostatic repulsion of BSA molecules through screening, which further reduces the viscosity of the solution. The trend with increasing ionic strength observed at pH 3.9 is less obvious and can not be explained through electrostatic screening. Previous studies have shown that concentrated BSA solutions (> nearly 150 mg/mL) form an electrostatically triggered hydrogel within 24 h at room temperature in the pH range between 3.0 to 4.0, at which BSA is partially denatured and the increased solvent exposure hydrophobic surface area drives the self-assembly.[16] Atomistic molecular dynamics studies indicate that the hydrophobic interactions govern protein aggregation and the counter-ion binding promotes the self-assembly of BSA

by overcoming the electrostatic repulsions of highly charged BSA monomers, which further facilitates the formation of the hydrogel. [17] In this work, the formation of hydrogel is not observed but this may be due to the lack of incubation time. However, the increase in viscosity at high ionic strength observed at pH 3.9 is consistent with the proposed theory, that the increase in the free ions concentration promotes the hydrophobic interactions of BSA and the formation of the protein network. This also explains why at high ionic strength the BSA solution is the most viscous at pH 3.9 compared with the other values of pH.

As shown in Figure 4.3, for the ionic strength range studied ($\sim 0 - 0.28$ M), the viscosity is lowest at pH 5.0. Tanford and Buzzel observed the same trend at low BSA concentration (40 mg/mL), which is explained by the charge-induced electroviscous effects. [18] Yadav *et al.* (2011) reported an opposite viscosity behavior for BSA at 250 mg/mL, where the highest viscosity is observed at pH 5.0. [15] This is at the same concentration range as this work. The inconsistency in reported behavior could be explained by the varied purity and quality of BSA from different sources. Gu *et al.* (2018) reported that the viscosity behaviors can be profoundly affected by the BSA product type and lot. [19] Yadav *et al.* measured the viscosity using a VISCOLab 500 viscometer with a moving piston, for which the shear rate ranged from 350 to 1000 Hz. [15] In this work, we quantify the zero shear viscosity using MPT. Additionally, the VISCOLab 500 viscometer generates an air-liquid interface, at which BSA has the strong tendency to adsorb and form aggregates. The layer of BSA networks affects viscosity measurements, especially

at low shear rates. [19–21] The difference in methods can cause inconsistency in the measured results.

These results suggest that electrostatic interactions are minimal at pH 5.0 and hydrophobic interactions dominate at pH 3.9. Caffeine has been shown to reduce the viscosity of concentrated mAb solutions via the suppression of hydrophobic interactions by weakly binding to the aromatic residues of the proteins. [22] To further explore if hydrophobic interactions govern the viscosity behaviors at pH 5.0 and pH 3.9, 15 mg/mL caffeine is added to each BSA solution. The concentration dependence of viscosity is examined at $\xi = 0.8$, at which all the electrostatic interactions are screened. Figure 4.6 shows the viscosity as a function of BSA concentration at pH 5.0 (diamonds) and 3.9 (squares), respectively. The filled and open symbols represent the BSA solution with and without caffeine, respectively. For both pHs, adding caffeine has no effect on the viscosity of BSA solutions. BSA reversibly changes conformations with variation in pH. [23, 24] At pH 5.0, BSA is in the stable heart-like N form. [23, 25] No change in viscosity with caffeine indicates that less hydrophobic interactions are involved. This is consistent with the literature result that the addition of hydantoin, which has a similar structure to caffeine, only slightly reduces the viscosity of BSA at pH 7.0.[26] In addition, Inoue *et al.* (2014) demonstrated that ArgHCl, which reduces the viscosity of protein solutions by suppressing both the electrostatic and hydrophobic interactions, has the same effects as NaCl on reducing the BSA viscosity at pH 7.4 and concludes that less hydrophobic interactions are involved in the concentrated BSA solutions.[27] At both pH 7 and 7.4, BSA is in the same N form as pH 5.0. At pH

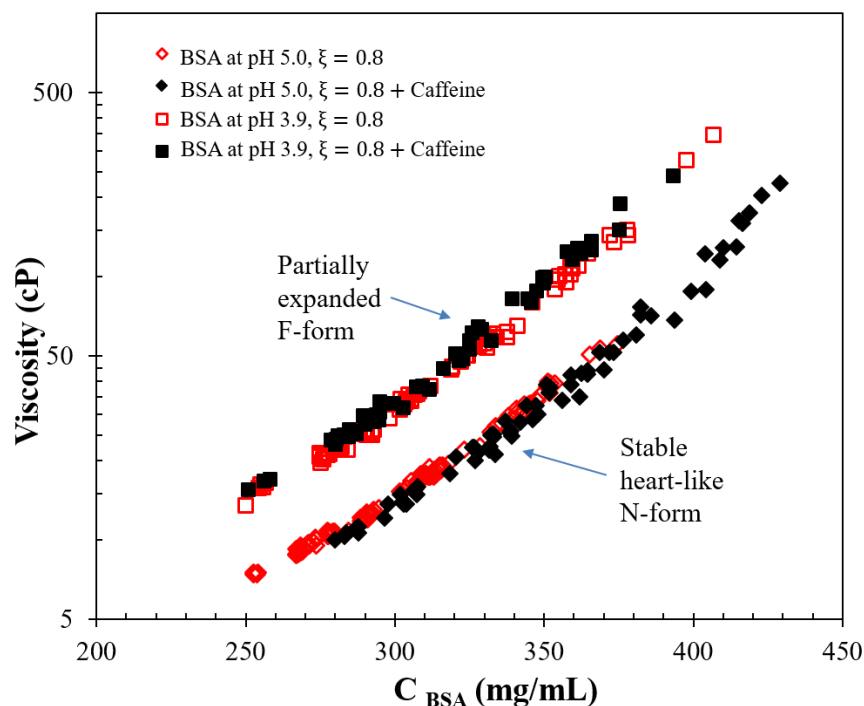


Figure 4.6 Viscosity of BSA as a function of BSA concentration at pH 5.0 (diamonds) and pH 3.9 (squares) with ξ of 0.8. The filled and open symbols represent the BSA solution with and without caffeine, respectively. BSA is in the stable heart-like N-form and partially expanded F-form at pH 5.0 and 3.9, respectively.

3.9, BSA is in a partially expanded F form and hydrophobic interactions dominate.

[23, 25] No reduction in viscosity by adding caffeine suggested that the mechanism of interaction between caffeine and partially denatured BSA is more complicated than weakly binding. The specific type of intermolecular interactions of BSA at these two pHs and the mechanism of caffeine on changing the viscosity require further characterization.

4.4 Conclusion

In this chapter, the viscosity of BSA has been systematically quantified as a function of BSA concentration, pH, and ionic strength using the droplet-based microfluidic device with small sample volume and high resolution in concentration.

The viscosity of BSA is found to be lowest at pH 5.0, which is the pI of BSA, and increases as the pH deviates from pI. Increasing ionic strength effectively reduces the viscosity of BSA at pH 6.6 by shielding the electrostatic attractions between the protein molecules. The weaker effect is observed at pI due to less involvement of electrostatic interactions. High ionic strength exerts a negative effect at pH 3.9, which could be explained as that the increasing concentration of the counter ions overcomes the electrostatic repulsions between the highly charged and partially denatured BSA molecules, and promotes the hydrophobic interactions and self-assembly of the proteins. Therefore, it leads to an increase in the solution viscosity. Overall, we have demonstrated that this microfluidic device approach is able to provide high compositional data covering multi-parameter space, which has the potential to provide operating regimes for different formulation requirements and provide complimentary work for computational studies. The addition of caffeine has no effects at pH 5.0, indicating that fewer hydrophobic interactions are involved. Ineffectiveness of caffeine is also observed at pH 3.9, suggesting that the mechanism of interaction between caffeine and partially denatured BSA may be more complicated than interacting with the hydrophobic residues of the BSA surface, which requires further investigation. The developed droplet-based microfluidic has the potential to investigate and provide insights into the intermolecular mechanism of concentrated protein solutions.

4.5 *Reference*

1. Yadav S, Shire SJ, Kalonia DS (2010) Factors Affecting the Viscosity in High Concentration Solutions of Different Monoclonal Antibodies. *J Pharm Sci* 99:4812–4829
2. Hong T, Iwashita K, Shiraki K (2018) Viscosity Control of Protein Solution by Small Solutes: A Review. *0*:746–758
3. Yadav S, Shire SJ, Kalonia DS (2011) Viscosity Analysis of High Concentration Bovine Serum Albumin Aqueous Solutions. *Pharm Res* 28:1973–1983
4. Inoue N, Takai E, Arakawa T, Shiraki K (2014) Arginine and lysine reduce the high viscosity of serum albumin solutions for pharmaceutical injection. *J Biosci Bioeng* 117:539–543
5. Hirschman J, Venkataramani D, Murphy MI, Patel SM, Du J, Amin S (2021) Application of thin gap rheometry for high shear rate viscosity measurement in monoclonal antibody formulations. *Colloids Surfaces A Physicochem Eng Asp* 626:127018
6. Dharmaraj VL, Godfrin PD, Liu Y, Hudson SD (2016) Rheology of clustering protein solutions. *Biomicrofluidics* 10:043509
7. Lai P-K, Swan JW, Trout BL (2021) Calculation of therapeutic antibody viscosity with coarse-grained models, hydrodynamic calculations and machine learning-based parameters. In *MAbs* (Vol. 13, No. 1, p. 1907882)
8. Schwenger W, Pellet C, Attonaty D, Authelin JR (2020) An Empirical Quantitative Model Describing Simultaneously Temperature and Concentration Effects on Protein Solution Viscosity. *J Pharm Sci* 109:1281–1287
9. Sharma VK, Patapoff TW, Kabakoff B, et al (2014) In silico selection of therapeutic antibodies for development: viscosity, clearance, and chemical stability. *Proc Natl Acad Sci U S A* 111:18601–18606
10. Agrawal NJ, Helk B, Kumar S, Mody N, Sathish HA, Samra HS, Buck PM, Li L, Trout BL (2016) Computational tool for the early screening of monoclonal antibodies for their viscosities. *MAbs* 8:43–48
11. Lai PK, Fernando A, Cloutier TK, Gokarn Y, Zhang J, Schwenger W, Chari R, Calero-Rubio C, Trout BL (2021) Machine Learning Applied to Determine the Molecular Descriptors Responsible for the Viscosity Behavior of Concentrated Therapeutic Antibodies. *Mol Pharm* 18:1167–

12. Lai PK, Gallegos A, Mody N, Sathish HA, Trout BL (2022) Machine learning prediction of antibody aggregation and viscosity for high concentration formulation development of protein therapeutics. *MAbs*. (Vol. 14, No. 1, p. 2026208).
13. Yang D, Daviran M, Schultz KM, Walker LM (2021) Droplet-Based Microfluidic Tool to Quantify Viscosity of Concentrating Protein Solutions. *Pharm Res* 38:1765–1775
14. Du W, Klivanov AM (2011) Hydrophobic salts markedly diminish viscosity of concentrated protein solutions. *Biotechnol Bioeng* 108:632–636
15. Yadav S, Shire SJ, Kalonia DS (2011) Viscosity analysis of high concentration bovine serum albumin aqueous solutions. *Pharm Res* 28:1973–1983
16. Baler K, Michael R, Szleifer I, Ameer GA (2014) Albumin hydrogels formed by electrostatically triggered self-assembly and their drug delivery capability. *Biomacromolecules* 15:3625–3633
17. Baler K, Martin OA, Carignano MA, Ameer GA, Vila JA, Szleifer I (2014) Electrostatic Unfolding and Interactions of Albumin Driven by pH Changes: A Molecular Dynamics Study. *J Phys Chem B* 118:921–930
18. Tanford C, Buzzell JG (1955) Abstracted from the *Proc. Bull, Trans Faraday Soc* 36:533
19. Gu JH, Qian R, Chou R, Bondarenko P V., Goldenberg M (2018) Rotational Rheology of Bovine Serum Albumin Solutions: Confounding Effects of Impurities, Mechanistic Considerations and Potential Implications on Protein Formulation Development. *Pharm Res* 35:1–11
20. Castellanos MM, Pathak JA, Colby RH (2014) Both protein adsorption and aggregation contribute to shear yielding and viscosity increase in protein solutions. *Soft Matter* 10:122–131
21. Sharma V, Jaishankar A, Wang YC, McKinley GH (2011) Rheology of globular proteins: apparent yield stress, high shear rate viscosity and interfacial viscoelasticity of bovine serum albumin solutions. *Soft Matter* 7:5150–5160
22. Zeng Y, Tran T, Wuthrich P, Naik S, Davagnino J, Greene DG, Mahoney RP, Soane DS (2021) Caffeine as a Viscosity Reducer for Highly Concentrated Monoclonal Antibody Solutions. *J Pharm Sci* 110:3594–3604

23. Carter DC, Ho JX (1994) Structure of Serum Albumin. *Adv Protein Chem* 45:153–203
24. Peters T (1996) 01. Foreword: All about Albumin. *All about Albumin* xi–xiii
25. Leggio C, Galantini L, Pavel NV (2008) About the albumin structure in solution: cigar Expanded form versus heart Normal shape. *Phys Chem Chem Phys* 10:6741–6750
26. Nishinami S, Kameda T, Arakawa T, Shiraki K (2019) Hydantoin and Its Derivatives Reduce the Viscosity of Concentrated Antibody Formulations by Inhibiting Associations via Hydrophobic Amino Acid Residues. *Ind Eng Chem Res* 58:16296–16306
27. Inoue N, Takai E, Arakawa T, Shiraki K (2014) Arginine and lysine reduce the high viscosity of serum albumin solutions for pharmaceutical injection. *J Biosci Bioeng* 117:539–543

Chapter 5: Synergistic effects of multiple excipients on reducing viscosity of concentrated antibody solutions

5.1 Introduction

Various types of excipients are added to the concentrated protein solutions to control the viscosity by interrupting the protein-protein interactions (PPIs), such as electrostatic repulsions, attractions, hydrophobic interactions, steric repulsions, and specific interactions. [1–3] Each new protein or excipient will require a specific formulation based on PPIs. Among these excipients, ArgHCl is one of the most common excipients that showed a significant reduction in the viscosity of concentrated protein solutions, [3–5] suppressed protein aggregation, [6–9] enhanced the solubility of less soluble biomaterials, [10, 11] and suppressed liquid-liquid phase separation of proteins. [12] In addition, ArgHCl has no effect on the folding of proteins as it suppresses the PPIs. [13–15] However, the effectiveness of ArgHCl depends on the solution conditions and the intrinsic properties of the proteins. Inoue *et al.* reported that ArgHCl shows weak effectiveness at alkaline pH and exerts a negative effect on the viscosity of α -Amylase. [4] Zeng *et al.* demonstrated that the ineffectiveness of ArgHCl can be compensated by the addition of caffeine, which lowered the viscosity of the two mAb solutions for which ArgHCl failed. [16] Caffeine has been applied as a pharmaceutical ingredient with existing safety profiles and has been shown to have no effect on the stability and *in vitro* bioactivities of the mAbs. [16] The synergistic effect of ArgHCl and caffeine on reducing the viscosity of concentrated antibody solutions was observed (Patent US 9,605,051 B2) but has not been systematically studied. [17]

Limited availability of the therapeutic proteins hinders the effective characterization of their viscosities under formulation conditions with new types or various combinations of multiple excipients. In the last chapter, we have demonstrated that the droplet-based microfluidic tool implemented with multiple particle tracking microrheology (MPT) is able to quantify the viscosity of high concentration protein solutions across a wide range of parameter space with small sample volume and high compositional resolution. In this chapter, this microfluidic tool is applied to systematically quantify the effects of ArgHCl and caffeine on the viscosity of highly concentrated bovine gamma globulin (BGG) solutions under various formulation conditions, which will provide useful guidance on developing formulations with ArgHCl and caffeine as the viscosity-reducing agents. This work also demonstrates the potential of the microfluidic approach to assess the impact of multiple excipients on the viscosity and provide data with high compositional resolution, which can be potentially applied for computational methods of viscosity prediction for high concentration formulations.

5.2 Materials and methods

5.2.1 Materials

Bovine gamma globulin (BGG) (Product number: G5009), L-Arginine monohydrochloride (ArgHCl), caffeine, sodium carbonate, sodium bicarbonate, sodium phosphate dibasic and sodium phosphate monobasic are purchased from Sigma-Aldrich (St. Louis, MO). Light mineral oil is obtained from Fisher Scientific (Hampton, NH), and Fluorinert FC-70 is obtained from 3M (St. Paul, MN). Span-

80 is purchased from Sigma-Aldrich, and 008-FluoroSurfactant is purchased from RAN Biotechnologies, Inc. (Beverly, MA), which are added to the mineral oil and FC-70 oil, respectively, for producing droplets.

5.2.2 *Preparation of BGG solutions*

The phosphate buffer (pH 7) and carbonate buffer (pH 10) are prepared by dissolving appropriate buffer concentrations in deionized water (18.2 MΩ.cm) to achieve ionic strength of 15mM and the desired pH. Buffer solutions with ArgHCl, caffeine, and both ArgHCl and caffeine are made by dissolving the appropriate mass of excipients into the buffers at concentrations of 150 mM for ArgHCl and 15mg/mL for caffeine. Few drops of 1M NaOH are added to buffers with ArgHCl to compensate the pH reduction at pH 10. The induced change in the ionic strength is negligible. A known mass of BGG is dissolved in the buffers at different values of pH with or without excipients at a known volume in a volumetric flask to reach a target concentration of 240 mg/mL of BGG. The initial concentration is chosen to be able to capture the rapid increase in viscosity, although it is at the higher end for subcutaneous injection (~ 100 – 200 mg/mL). Also, the initial concentration ensures low enough solution viscosity so that there is no concern about concentration gradient inside the droplet. We define ξ_1 and ξ_2 as the mass ratios of ArgHCl to BGG and caffeine to BGG, respectively, which are calculated as 0.13 and 0.06. To better describe the different combinations of ArgHCl and caffeine, ξ is introduced as the sum of ξ_1 and ξ_2 . For example, ξ equals 0 for BGG without additive, and ξ equals 0.19 for BGG with both ArgHCl and caffeine. For each microfluidic experiment, 240 mg/mL BGG solution with a specific value of ξ is

loaded into the microfluidic device. During the dehydration experiment, the concentrations of all solutes increase, and ξ is constant.

5.2.3 Approach for measuring protein solution viscosity vs. concentration

The concentration dependence of viscosity of BGG solutions with different excipients and pH are quantified using the droplet-based microfluidic device. Aqueous droplets of dilute and well-mixed sample solution are generated in the channel traps and are surrounded by mineral oil. A 2wt% Span 80 in mineral oil and 2wt% fluorosurfactant in FC-oil are used to provide proper wetting conditions and lower interfacial tension for droplet production at pH 7 and pH 10, respectively. We have verified that the type of continuous phase oil and surfactant has no effect on the concentration and viscosity measurements. [18] The device fabrication and droplet generation are discussed in Chapter 2. The dehydration process of all 40 droplets is tracked under the microscope. The solution viscosity is quantified by multiple particle tracking microrheology (MPT) along the concentration process. The measurements of concentration dependence of viscosity in the shrinking droplets are thoroughly discussed in Chapter 3.3. Droplets are dehydrated at room temperature ($22 \pm 1^\circ\text{C}$).

For MPT measurements, carboxylated, fluorescently labeled polystyrene probe particles with a radius of $0.26 \pm 0.007 \mu\text{m}$ are dispersed in the solution with a concentration of 0.036% solids per volume and undergo Brownian motion. Even though a small extent of probe aggregation is observed in the BGG solutions with ArgHCl, more than 40 independent probes are able to be detected and provide enough statistics for calculating the mean-squared displacement (MSD). In addition,

the probe aggregation has an insignificant effect on the measured viscosity, which is verified by the consistent results between the measurements conducted in the viscometer and that measured by MPT. The movement of the probes is measured at 40 fps for 30s with 10 ms exposure time and is used to calculate the viscosity. The methodology of MPT has been explained in Chapter 2.4. All of our measurements are of diffusive particle motion, $\alpha = 1$. The microscopy setup is the same as in Chapter 4.

5.2.4 Measurements of initial protein concentrations

The protein concentrations of the loading sample solutions without caffeine are determined using the UV-vis spectrophotometer (NanoDrop 2000c, ThermoFisher Scientific, Waltham, MA) with the extinction coefficient of $E^{1\%} = 12.65 \text{ L g}^{-1} \text{ cm}^{-1}$ at 280 nm. [19, 20] For solutions with caffeine, the protein concentration is measured by Pierce BCA Protein Assay Kit, since caffeine exhibits strong absorption at 280 nm. BCA assay analysis is first performed with BGG standards at different concentrations ranging from 0 to 2000 $\mu\text{g/mL}$ under a specific buffer condition. 25 μL of each standard solution is mixed with 200 μL of BCA reagents (a mixture of reagent A and reagent B in a ratio of 50:1) in a 96-well plate and are incubated at 37 °C for 30 min. Then the mixed standards are cooled to room temperature and the absorbance of all the standards is measured at 562 nm in the BioTek Synergy H1 reader, which generates a calibration curve of absorbance vs. BGG concentration. The absorbance of the BGG solution with caffeine under the same buffer condition is measured and is used to calculate BGG concentration from the calibration curve.

5.3 Results

Figure 5.1 shows the viscosity of BGG solutions as a function of BGG concentration with various additives at pH 7 (Figure 5.1a) and pH 10 (Figure 5.1b). Circles represent the control case with no additive ($\xi = 0$). The squares, diamonds and triangles indicate BGG solutions with ArgHCl ($\xi = \xi_1 = 0.13$), caffeine ($\xi = \xi_2 = 0.06$) and both ArgHCl and caffeine ($\xi = 0.19$), respectively. The value of ξ is

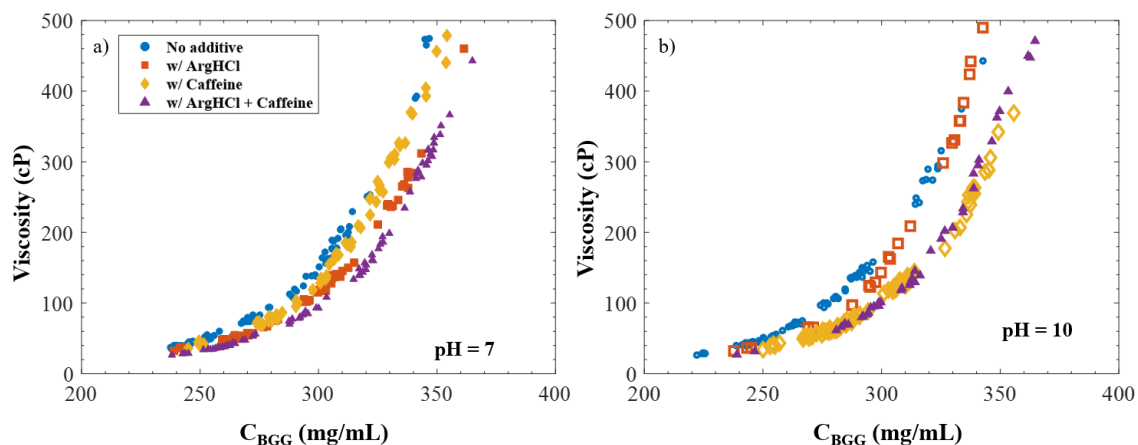


Figure 5.1 Concentration dependence of viscosity for BGG solutions at pH 7 (a) and pH 10 (b). Circles represent the control case with no additives. Squares, diamonds, and triangles represent BGG with ArgHCl, caffeine, and with both ArgHCl and caffeine, respectively. Each symbol represents one droplet dehydration experiment with a constant value of ξ .

defined in the method section and is applied to differentiate the combinations of the two excipients. The initial concentrations of ArgHCl and caffeine are chosen to be 150 mM and 15 mg/mL, respectively, which are shown to be able to induce more than 20% change in viscosity, [4, 17] so that the difference in viscosity can be easily identified by MPT technique. Each curve shows one droplet dehydration experiment with a constant value of ξ , generating data points with high continuity in the concentration dimension referred as high compositional resolution. As shown in Figure 5.1, for all eight cases, a gradual increase in viscosity with concentration

is observed up to approximately 280 - 300 mg/mL and the viscosity starts to increase sharply above 300 mg/mL, due to the enhanced intermolecular interactions between protein molecules as expected. [4, 21, 22] At pH 7, both ArgHCl and caffeine decrease the viscosity of BGG solution, and ArgHCl is more effective compared to caffeine. Synergistic effects of ArgHCl and caffeine on reducing the viscosity are observed, which provides the largest extent of reduction in viscosity. At pH 10, ArgHCl effectively decreases the viscosity at low BGG concentrations, while little and even negative effects are observed at high protein concentrations. Caffeine lowers the viscosity of BGG and is much more effective than ArgHCl. Furthermore, no synergistic effect is observed, which is indicated by the fact that the addition of caffeine and ArgHCl has the same effect as adding caffeine alone. There is an apparent difference in the performance of ArgHCl and caffeine as the viscosity-reducing excipients between pH 7 and pH 10. For both pHs, adding two excipients together shifts the viscosity-concentration curve to the right, while the single component curves flip the order as pH changes. During the dehydration experiment, the concentrations of all solutes (including BGG, the salts from buffer, ArgHCl, and caffeine) increase, but the mass ratio of each excipient to BGG is constant. Since the initial BGG concentration and the initial ionic strength of the buffer are the same for pH 7 and 10, at a specific BGG concentration and ξ , the solution conditions (such as the concentration of each excipient and the ionic strength) are the same for both pHs. To be mentioned, the theoretical maximum measurable viscosity by MPT for probe radius of 0.26 μm under the current experimental setup is calculated to be 500 cP. [18]

To better understand the effect of BGG concentration on the performance of the excipients in reducing viscosity, the viscosity of BGG solutions is plotted as a function of BGG concentration and ξ at pH 7 (a) and pH 10 (b), respectively as shown in Figure 5.2. Each symbol represents the type of excipients as in Figure 5.1, which is specified by the value of ξ . Here the dimension of ξ is not continuous in

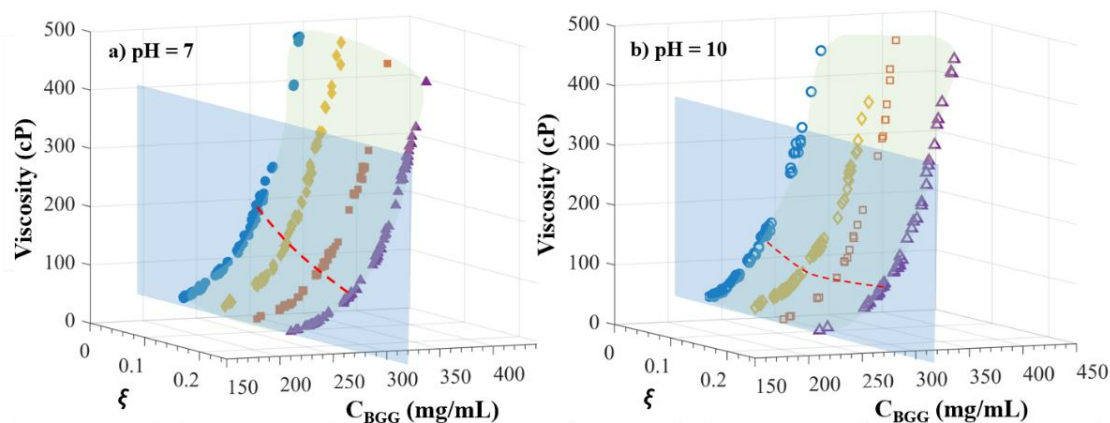


Figure 5.2 Viscosity of BGG as a function of BGG concentration and ξ at pH 7 (a) and pH 10 (b). Different types of symbols represent the excipients same as denoted in Figure 5.1. The light green shaded area represents the surface plot generated based on the continuous data points. The shaded rectangle indicates the plane cut at the BGG concentration of 280 mg/mL as an example and the dashed red line shows the iso-concentration line, which is drawn to guide the eyes.

magnitude. The high resolution in concentration enables the generation of a surface plot, represented by the green shaded area, which indicates the wide range of covered parameter space. To investigate the dependence of the effectiveness of excipients on BGG concentration, plane cuts at three constant BGG concentrations: 280 mg/mL, 330 mg/mL, and 340 mg/mL are performed at each pH. The shaded blue rectangle in Figure 5.2 represents a plane cut at 280 mg/mL as an example. For each pH, the four intersection points with the plane are linearly interpolated based on the continuous exact data points of each viscosity-concentration curve, which are connected by the red dotted line drawn to guide the eyes.

In Figure 5.3, the columns of each color represent the four intersection points obtained from the plane cuts at three constant BGG concentrations: 280 mg/mL (orange), 330 mg/mL (gray) and 340 mg/mL (yellow) as mentioned above. The height of the column indicates the viscosity. Instead of using ξ as the x-axis, the type of excipient is directly labeled. Figure 5.3 (a) and (b) show the results for

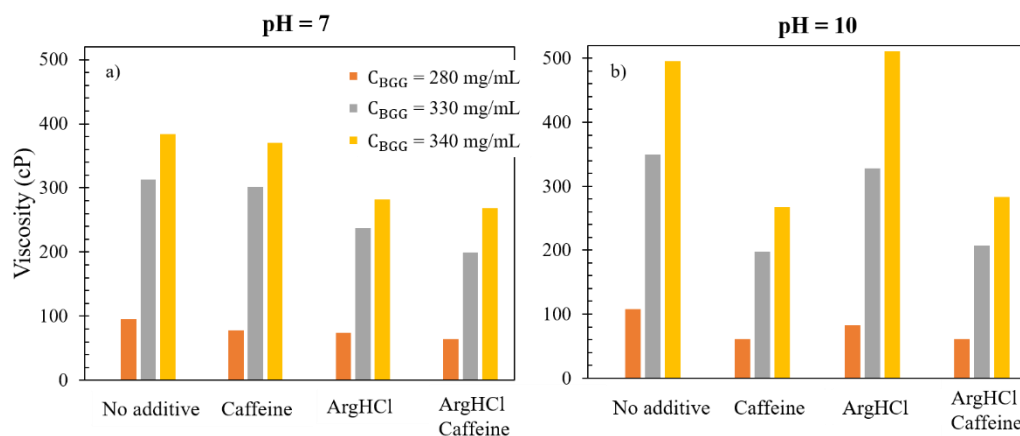


Figure 5.3 Viscosity of BGG versus type of excipients at BGG concentrations of 280 mg/mL (orange), 330 mg/mL (gray) and 340 mg/mL (yellow) at pH 7 (a) and pH 10 (b).

pH 7 and pH 10, respectively. Again, it can be clearly observed that ArgHCl is less effective at pH 10 compare to pH 7, especially at high BGG concentrations, and caffeine shows the opposite behavior. The degree of change in viscosity resulting from the excipients appears to be more significant at pH 10 than pH 7, and it also depends on the BGG concentration for both pH values.

Figure 5.4 illustrates the percent change in viscosity as a function of BGG concentration, which is calculated based on data in Figure 5.3. At pH 7, ArgHCl decreases the viscosity up to 340 mg/mL and is more effective than caffeine. Caffeine reduces the viscosity by approximately 20% at lower BGG concentration, while the reduction in viscosity decreases to nearly 4% as BGG concentration increases to 330 mg/mL. A synergistic effect of ArgHCl and caffeine is observed at all three BGG concentrations and is weakly dependent on the BGG concentration. At pH 10, ArgHCl effectively reduces the viscosity at 280 mg/mL. As the BGG

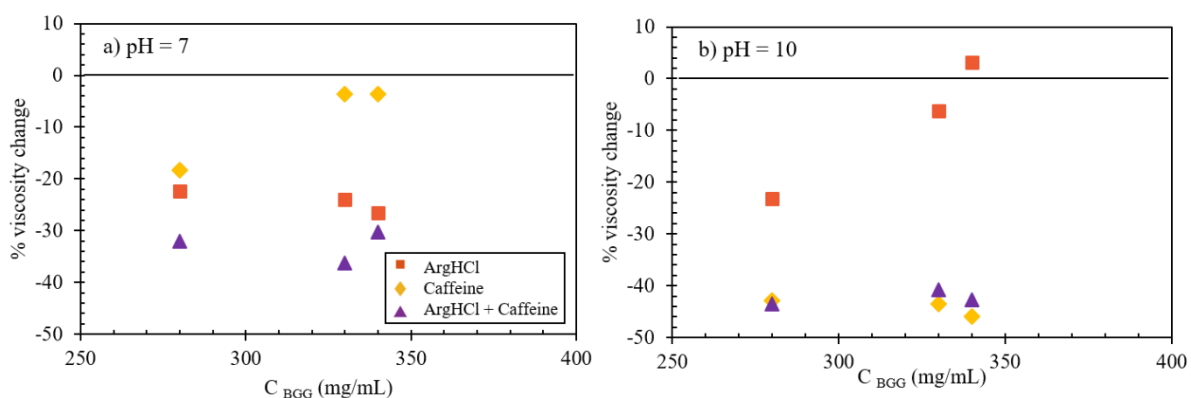


Figure 5.4 The degree of change in viscosity as a function of BGG concentration at pH 7 (a) and pH 10 (b). Squares, diamonds, and triangles represent ArgHCl, caffeine, and ArgHCl with caffeine, respectively.

concentration increases, ArgHCl shows a weaker reducing effect on the viscosity and even increases the viscosity by nearly 4% at 340 mg/mL. Caffeine significantly lowers the viscosity by approximately 40% at all three concentrations, which is more effective than ArgHCl. No synergistic effect is observed, which is illustrated by the same magnitude of change in viscosity with caffeine alone and with both caffeine and ArgHCl.

The advantage of this droplet-based microfluidic device is that it generates high compositional resolution data that covers a wide range of parameter space, which can provide useful information for developing formulations with ArgHCl and caffeine as the viscosity-reducing excipients. In addition, less than a mL of the stock protein solutions is required to conduct the eight experiments, which is essential for precious therapeutic proteins. Subcutaneous injection requires protein solutions to be formulated at high concentrations due to small injection volume and 50 cP is considered to be a threshold value for subcutaneous injection. [23] Therefore, we performed a plane cut at a constant a viscosity of 50 cP on the surface plot, which is illustrated by the shaded rectangle in Figure 5.5 for pH 7 (a) and pH

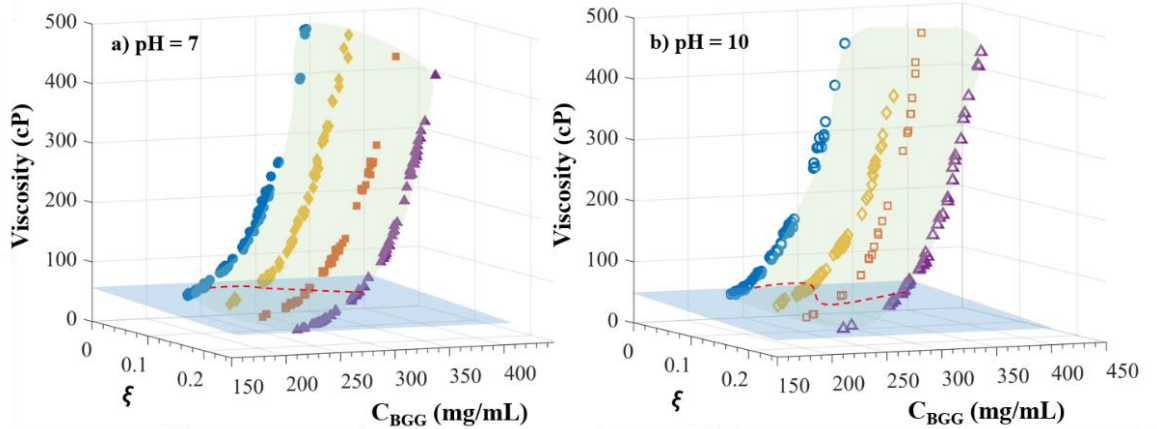


Figure 5.5 Viscosity of BGG as a function of BGG concentration and ξ at pH 7 (a) and pH 10 (b). Different types of symbols represent the additives same as denoted in Figure 5.1. The light green shaded area represents the surface plot generated based on the continuous data points. The shaded rectangle indicates the plane cut at 50 cP. The dashed red line shows the iso-viscosity line, which is drawn to guide the eyes.

10 (b). Similarly, the plane cut generates four intersection points for each pH, which are connected by the red dashed line drawn to guide the eyes, indicating BGG concentrations at four values of ξ at viscosity of 50 cP. The columns in Figure 5.6 show the interpolated four intersection points for both pH 7 (crossed blue) and pH

10 (green). The height of the column illustrates the BGG concentration. The x-axis indicates different types of excipients, each of which corresponds to a value of ξ same as Figure 5.5. At pH 7, by adding both ArgHCl and caffeine, the BGG concentration can be increased from nearly 312 mg/mL to 330 mg/mL, at which the viscosity of BGG solution still maintains 50 cP. Adding ArgHCl or caffeine alone is effective but to a much lesser extent than the combination of both.

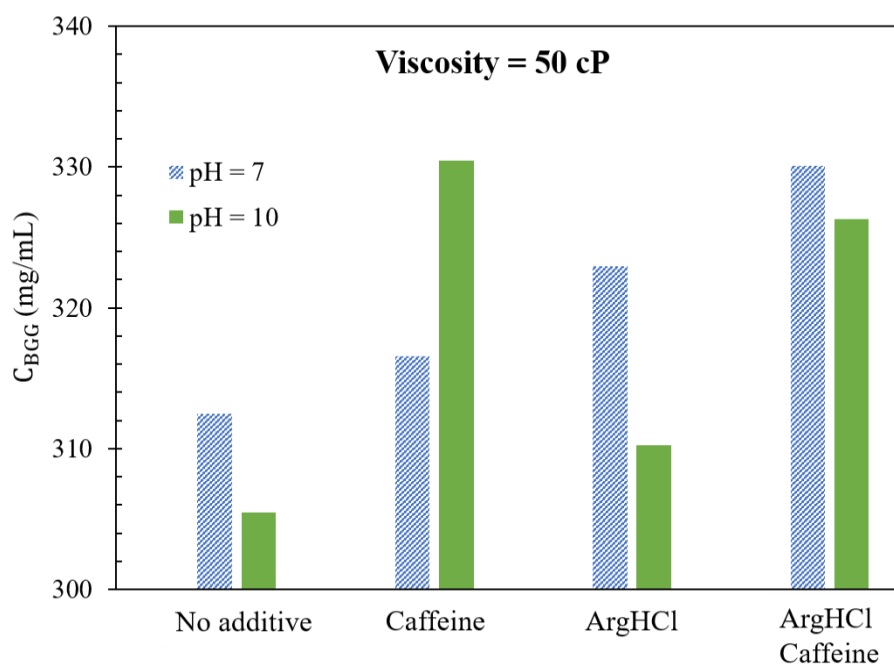


Figure 5.6 BGG concentration versus type of excipients at a constant viscosity of 50 cP for pH 7 (crossed blue) and pH 10 (green).

Therefore, adding both excipients is the ideal choice among the four candidate formulations. At pH 10, by adding ArgHCl, the BGG concentration can be increased from approximately 306 mg/mL to 330 mg/mL. Addition of both ArgHCl and caffeine shows a smaller degree of increase in the BGG concentration. Therefore, instead of adding both excipients to the formulation, adding ArgHCl alone can provide the most effective outcome, which also reduces cost due to fewer materials. In addition, for the formulation with caffeine alone, changing pH from 7

to 10 can increase the BGG concentration from nearly 315 mg/mL to 330 mg/mL, which is opposite to the other three cases and could be missed in the discrete experiments.

The limited availability of the therapeutic proteins induces challenges in the characterization of the viscosity of high concentration formulations, especially during the early stage of development where a large number of candidate formulations need to be screened. Machine learning has been recently applied to predict the viscosity of concentrated therapeutic proteins. [24–26] The uncertainties

Table 5.1. Tabulated parameters obtained from fitting the viscosity-concentration curves to $\eta = a\exp(bC)$

(pH, ξ)	a	b	R^2
(7, 0)	0.134 ± 0.006	0.0235 ± 0.0002	0.997
(7, 0.06)	0.081 ± 0.007	0.0247 ± 0.003	0.992
(7, 0.13)	0.137 ± 0.007	0.0225 ± 0.002	0.994
(7, 0.19)	0.087 ± 0.004	0.0235 ± 0.002	0.997
(10, 0)	0.107 ± 0.005	0.0246 ± 0.002	0.996
(10, 0.06)	0.113 ± 0.007	0.0228 ± 0.002	0.994
(10, 0.13)	0.050 ± 0.006	0.0267 ± 0.004	0.994
(10, 0.19)	0.070 ± 0.007	0.0243 ± 0.003	0.993

in the experimental data have a non-negligible influence on the feature selection and the classification accuracy of the developed model. In this work, the high compositional resolution data obtained from the microfluidic tool can provide resources for estimating viscosities at various solution conditions with improved accuracy. Each viscosity curve in Figure 5.1 is fitted to the simplest exponential function, $\eta = a\exp(bC)$, where C is the BGG concentration in mg/mL, η is viscosity, and a and b are the fitted parameters. The fitted parameters with

uncertainties are tabulated in Table 5.1. It is mentioned that even though the viscosity-concentration curves can be fitted to the exponential function with a value of R^2 close to 1, at low concentrations, the data deviate from the fitted line as indicated by the red circle in **Figure 2.1**Figure 5.7. Figure 5.7 shows the viscosity as a function of BGG concentration plotted in the semi-log scale for BGG with

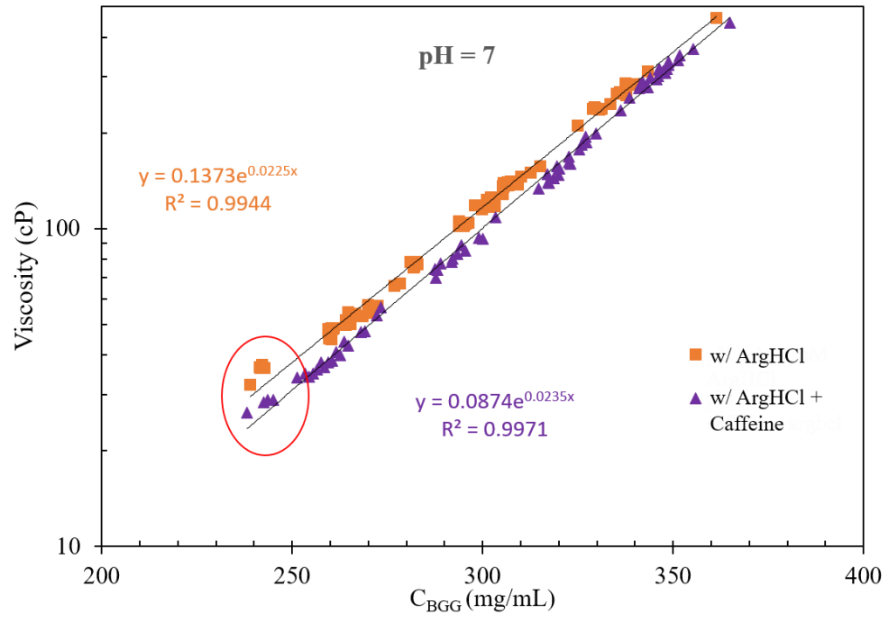


Figure 5.7 Viscosity-concentration curves for BGG with ArgHCl (squares) and both ArgHCl and caffeine (triangles) at pH 7, which are fitted to the exponential function of $\eta = a\exp(bC)$ represented by the solid lines, where C is the BGG concentration in mg/mL, η is viscosity, and a and b are the fitted parameters. The red circle indicates the deviation from the exponential function at low BGG concentrations.

ArgHCl (squares) and both ArgHCl and caffeine (triangles) at pH 7 as an example.

This deviation at low concentration from the fitted function could be missed in the discrete experiments, but it is captured by the high compositional data obtained from the microfluidic tool. The small gaps between the clusters of data points in each viscosity-concentration curve can be filled by increasing the frequency of the viscosity scan, which will further improve the accuracy of the fitting parameters.

Overall, we have demonstrated that this microfluidic method of simple parameterization can provide data resources for machine learning methods to predict the viscosity of concentrated therapeutic proteins and has the potential to be used in more complex formulation design approaches.

5.4 Discussion

The results indicate that the effectiveness of ArgHCl and caffeine on reducing viscosity is different at the two pH values and exhibits a BGG concentration-dependence. During each droplet shrinking, the concentration of BGG increased by almost two fold, which is the same for all the other solutes in the solution. During the dehydration, the change in the Debye length due to the increase in the ionic strength is negligible, as it decreased from 2.5 nm to 2.0 nm. The change in the acid-base equilibrium constant due to the increase in the ionic strength causes a negligible shift (less than 0.02 pH unit) in the solution pH.

At pH 7, ArgHCl is more effective compared to caffeine at all three BGG concentrations and the synergistic effect is observed between ArgHCl and caffeine. pH 7 is near the isoelectric point of BGG, [27] at which the electrostatic interactions are less dominant than other interactions, such as the hydrophobic interactions. Caffeine has been reported to significantly reduce the viscosity of antibody solutions by weakly binding to the aromatic and charged amino acid residues on the protein surface, which decreases the hydrophobic interactions between the protein molecules through the cation- π and π - π interactions. [16] Aside from suppressing the hydrophobic interactions in a similar manner to caffeine, [3, 28–

30] ArgHCl also reduces the electrostatic interactions between the protein molecules acting simply as a salt. [3] Therefore, ArgHCl is more effective than caffeine in reducing the viscosity by compensating the electrostatic shielding effect that is lacking in caffeine. Such compensating effect has been observed for hydantoin, possessing a similar structure and mechanism to caffeine, whose effectiveness in reducing the protein viscosity is augmented by adding NaCl. [3] This also explains the synergistic effect between ArgHCl and caffeine, which has been observed for BGG at pH 6. [17] In addition, as the concentration of BGG increases, the extent of reduction in viscosity resulting from caffeine decreases, while ArgHCl is slightly more effective at higher BGG concentrations. At pH 7, caffeine is nonionic and ArgHCl is charged. [16] The difference in the charge state may cause variation in the binding strength with proteins. At high BGG concentration, the molecular crowding effect (excluded volume effect) is enhanced, which may hinder the weak binding between caffeine and the amino acid residues on the protein surface.

At pH 10, the ArgHCl shows weaker effectiveness and it even increases the viscosity as the BGG concentration increases. The diminished effectiveness of ArgHCl may be ascribed to the loss of the positive-charge on the α -amino group, which has a pKa of 9.0 and is deprotonated at pH 10. [31] Miyatake *et al.* reported that ArgHCl had limited effects in suppressing heat-induced protein aggregation at alkaline pH, where ArgHCl lost its positive charge of the amino group and thus the non-charged ArgHCl became more hydrophobic and its binding to the proteins promoted the hydrophobic interactions and the aggregation of proteins. [32] The

same mechanism of ArgHCl could be applied here. BGG has a negative net charge at pH 10, therefore, both the electrostatic and hydrophobic interactions contribute importantly to the high viscosity. At low BGG concentrations, the electrostatic interaction may dominate. ArgHCl decreases the viscosity by the electrostatic shielding. As BGG concentration increases, the short-range hydrophobic interactions dominate, the counteracting effects between the electrostatic shielding and the promotion of hydrophobic interactions reduce the effectiveness of ArgHCl. At higher BGG concentrations, the promoted hydrophobic interactions overcome the shielded electrostatic attractions by ArgHCl and further increase the viscosity of BGG solutions. Inoue *et al.* also observed that ArgHCl is less effective in reducing the viscosity of BGG at pH 9.4 than pH 7.4 and 5.4. [4] The performance of caffeine is not affected by the BGG concentrations at pH 10. At low BGG concentrations, caffeine appears to be more effective than ArgHCl, suggesting that hydrophobic interactions are suppressed by caffeine. Caffeine is nonionic at pH 10. The difference in the charge state and the structure may make the binding between proteins and caffeine more favorably than that with ArgHCl at pH 10. [16] Zeng *et al.* observed that caffeine effectively reduced the viscosity of two concentrated antibody solutions, where ArgHCl showed no effect. [16] No synergistic effect of ArgHCl and caffeine is observed at pH 10 due to the loss of effectiveness of ArgHCl.

5.5 *Conclusions*

In this chapter, we have quantified the effects of ArgHCl and caffeine on the viscosity of BGG solutions at two pHs with high compositional resolution using the novel microfluidic device. The effectiveness of ArgHCl and caffeine depend on the solution conditions. The synergistic effect of ArgHCl and caffeine on reducing the viscosity is observed at pH 7, which may be induced by the additive effects of electrostatic screening and the interferences of the hydrophobic interactions between the protein molecules. ArgHCl loses its effectiveness at pH 10 and no synergistic effect is observed. This may be due to the change of the charge state of ArgHCl. The high compositional resolution data shows the potential of the microfluidic device to test the novel excipients and provide guidance for developing the therapeutic formulations by efficiently screening out a large number of candidate formulations. In addition, the nearly continuous viscosity-concentration curve can provide resources for the computational methods to predict the viscosity of high concentration formulations. The microscopy station will be fully automated to improve the frequency of the viscosity scan, which can further improve the compositional resolution of the data points. Small sample volumes required by this approach provide an advantage for the characterization of the precious therapeutic proteins. In the future, the resolution in ξ could be increased to examine the effect of the mass ratio of ArgHCl to caffeine on the synergistic effect.

5.6 *Reference*

1. Wang S, Zhang N, Hu T, Dai W, Feng X, Zhang X, Qian F (2015) Viscosity-Lowering Effect of Amino Acids and Salts on Highly Concentrated Solutions of Two IgG1 Monoclonal Antibodies. *Mol Pharm* 12:4478–4487
2. Inoue N, Takai E, Arakawa T, Shiraki K (2014) Arginine and lysine reduce the high viscosity of serum albumin solutions for pharmaceutical injection. *J Biosci Bioeng* 117:539–543
3. Nishinami S, Kameda T, Arakawa T, Shiraki K (2019) Hydantoin and Its Derivatives Reduce the Viscosity of Concentrated Antibody Formulations by Inhibiting Associations via Hydrophobic Amino Acid Residues. *Ind Eng Chem Res* 58:16296–16306
4. Inoue N, Takai E, Arakawa T, Shiraki K (2014) Specific decrease in solution viscosity of antibodies by arginine for therapeutic formulations. *Mol Pharm* 11:1889–1896
5. Borwankar AU, Dear BJ, Twu A, Hung JJ, Dinin AK, Wilson BK, Yue J, Maynard JA, Truskett TM, Johnston KP (2016) Viscosity Reduction of a Concentrated Monoclonal Antibody with Arginine·HCl and Arginine·Glutamate. *Ind Eng Chem Res* 55:11225–11234
6. Arakawa T, Ejima D, Tsumoto K, Obeyama N, Tanaka Y, Kita Y, Timasheff SN (2007) Suppression of protein interactions by arginine: A proposed mechanism of the arginine effects. *Biophys Chem* 127:1–8
7. Hamada H, Arakawa T, Shiraki K. (2009) Effect of Additives on Protein Aggregation. *Current pharmaceutical biotechnology*. 10(4): 400-7.
8. Tsumoto K, Ejima D, Kita Y, Arakawa T (2005) Review: Why is Arginine Effective in Suppressing Aggregation? *Protein Pept Lett* 12:613–619
9. Shiraki K, Kudou M, Fujiwara S, Imanaka T, Takagi M (2002) Biophysical effect of amino acids on the prevention of protein aggregation. *J Biochem* 132:591–595
10. Tischer A, Lilie H, Rudolph R, Lange C (2010) L-Arginine hydrochloride increases the solubility of folded and unfolded recombinant plasminogen activator rPA. *Protein Sci* 19:1783–1795
11. Takai E, Yoshizawa S, Ejima D, Arakawa T, Shiraki K (2013) Synergistic solubilization of porcine myosin in physiological salt solution by arginine. *Int J Biol Macromol* 62:647–651
12. Kheddo P, Bramham JE, Dearman RJ, Uddin S, Van Der Walle CF, Golovanov AP (2017) Investigating Liquid-Liquid Phase Separation of a Monoclonal Antibody Using Solution-State NMR Spectroscopy: Effect of Arg·Glu and Arg·HCl. *Mol Pharm* 14:2852–2860

13. Arakawa T, Kit Y. (2014) Multi-Faceted Arginine: Mechanism of the Effects of Arginine on Protein. *Curretn Protein an Peptide Science*. 15(6): 208-20.
14. Tsumoto K, Umetsu M, Kumagai I, Ejima D, Philo JS, Arakawa T (2004) Role of Arginine in Protein Refolding, Solubilization, and Purification. *Biotechnol Prog* 20:1301–1308
15. Ishibashi M, Tsumoto K, Tokunaga M, Ejima D, Kita Y, Arakawa T (2005) Is arginine a protein-denaturant? *Protein Expr Purif* 42:1–6
16. Zeng Y, Tran T, Wuthrich P, Naik S, Davagnino J, Greene DG, Mahoney RP, Soane DS (2021) Caffeine as a Viscosity Reducer for Highly Concentrated Monoclonal Antibody Solutions. *J Pharm Sci* 110:3594–3604
17. (2017) (12) United States Patent (45) Date of Patent: (54) (71) (72) (73) (*) (21) (22) (65) (63) (60) (51) (52) (58) VISCOSTY-REDUCING EXCIPIENT COMPOUNDS FOR PROTEIN FORMULATIONS.
18. Yang D, Daviran M, Schultz KM, Walker LM (2021) Droplet-Based Microfluidic Tool to Quantify Viscosity of Concentrating Protein Solutions. *Pharm Res* 38:1765–1775
19. Tyn MT, Gusek TW (1990) Prediction of diffusion coefficients of proteins. *Biotechnol Bioeng* 35:327–338
20. Duncan JR, Wilkie BN, Hiestand F, Winter AJ (1972) The Serum and Secretory Immunoglobulins of Cattle: Characterization and Quantitation. *J. Immunol.* 108:
21. Yadav S, Liu J, Shire SJ, Kalonia DS (2010) Specific interactions in high concentration antibody solutions resulting in high viscosity. *J Pharm Sci* 99:1152–1168
22. Liu J, Nguyen MDH, Andya JD, Shire SJ (2005) Reversible self-association increases the viscosity of a concentrated monoclonal antibody in aqueous solution. *J Pharm Sci* 94:1928–1940
23. Du W, Klibanov AM (2011) Hydrophobic salts markedly diminish viscosity of concentrated protein solutions. *Biotechnol Bioeng* 108:632–636
24. Lai PK, Fernando A, Cloutier TK, Gokarn Y, Zhang J, Schwenger W, Chari R, Calero-Rubio C, Trout BL (2021) Machine Learning Applied to Determine the Molecular Descriptors Responsible for the Viscosity Behavior of Concentrated Therapeutic Antibodies. *Mol Pharm* 18:1167–1175
25. Lai PK, Gallegos A, Mody N, Sathish HA, Trout BL (2022) Machine learning prediction of antibody aggregation and viscosity for high concentration formulation development of protein therapeutics. *MAbs*. (Vol. 14, No. 1, p. 2026208).
26. Narayanan H, Dingfelder F, Condado Morales I, et al (2021) Design of Biopharmaceutical Formulations Accelerated by Machine Learning. *Mol Pharm*

27. Sakata S, Inoue Y, Ishihara K (2016) Precise control of surface electrostatic forces on polymer brush layers with opposite charges for resistance to protein adsorption. *Biomaterials* 105:102–108
28. Vagenende V, Han AX, Mueller M, Trout BL (2013) Protein-associated cation clusters in aqueous arginine solutions and their effects on protein stability and size. *ACS Chem Biol* 8:416–422
29. Ito L, Shiraki K, Matsuura T, Okumura M, Hasegawa K, Baba S, Yamaguchi H, Kumasaka T (2011) High-resolution X-ray analysis reveals binding of arginine to aromatic residues of lysozyme surface: implication of suppression of protein aggregation by arginine. *Protein Eng Des Sel* 24:269–274
30. Shukla D, Trout BL (2010) Interaction of arginine with proteins and the mechanism by which it inhibits aggregation. *J Phys Chem B* 114:13426–13438
31. Of C, Isoelectric P (2002) *Data for biochemical research*, 3rd ed. Clarendon Press, Oxford
32. Miyatake T, Yoshizawa S, Arakawa T, Shiraki K (2016) Charge state of arginine as an additive on heat-induced protein aggregation. *Int J Biol Macromol* 87:563–569

Chapter 6: Quantifying the effects of additives on the phase transition of lyotropic liquid crystals with high composition resolution

6.1 *Introduction*

Protein crystallization is a powerful tool of purification and is used by crystallographers to study the three-dimensional structure of proteins via x-ray diffraction. [1] Recently, crystalline formulations of proteins have been demonstrated to be a promising alternative for subcutaneous injection, which exhibits much lower viscosity and higher stability compared with solution formulations. [2–4] Therefore, protein crystallization is essential for the manufacturing and delivery of biotherapeutic proteins. Protein crystallization is a complicated process, which is sensitive to a large number of parameters, such as pH, temperature, purity, and concentration of protein, concentration of excipients, etc. [5] A large number of candidate formulation conditions need to be tested and screened to determine the best formulation conditions to produce high-quality crystals. In addition, the crystallization conditions can not be transferred to another protein, which even complicates the screening process.

Kinetic approaches developed to find the optimal conditions for protein crystallization, such as hanging drop and micro-batch require large sample volumes, which is limited for the precious therapeutic proteins. [6] Microfluidic methods have been applied to study protein crystallization with significantly reduced sample volume. [7–11] Birefringence has been widely applied to study crystallization of macromolecules. [12, 13] In this chapter, the droplet-based microfluidic device is implemented with polarizing microscopy. Birefringence is applied as the sensing

method to quantify the phase transitions of a lyotropic chromonic liquid crystal, which is rich in optical polarization and is chosen as the test case for verifying the applicability of the microfluidic device to identify the crystalline phase transitions based on birefringence.

6.1.1 Lyotropic Chromonic Liquid Crystals (LCLCs)

Lyotropic chromonic liquid crystals (LCLCs), a distinct class of lyotropic liquid crystals, are central to a wide range of applications such as biological sensing, [14, 15] optical compensators, [16, 17] production of patterned dye films, [16, 18] organic electronics, [19] and functional materials for nanofabrication. [20] LCLCs often have a plank-like rigid aromatic core with polar groups at the periphery. When dissolved in water, the chromonic molecules have a strong tendency to form the reversible self-assembled aggregates, defined as mesogens, by stacking on top of each other through the non-covalent π - π interactions. Besides concentration, the aggregation also depends on temperature, ionic content, pH, and the structure of the chromonic molecule. [21–26] As the concentration increases, the mesogens become ordered and form mesophases, which exhibit specific optical textures, defined as birefringence, and can be identified using the polarizing microscope. [16, 21, 27] The uniaxial nematic (N) phase and the hexagonal columnar (C) phase are the two most common mesophases. [16, 20, 21]

It has been shown that colloidal forces impact both the structure of mesogens and intermesogen interactions. Addition of additives affects the self-assembly of LCLCs mainly through electrostatic interactions and excluded volume effects, and further influence the phase transitions, which are the essential physical

properties deciding their applications. [28] Saupe *et al.* reported that by adding NaCl to disodium cromoglycate (DSCG), one of the most studied LCLC materials, both the phase transition temperatures from the nematic (N) to nematic + isotropic (N+I) coexistence phase ($T_{N \rightarrow N+I}$) and from the N+I phase to the I phase ($T_{N+I \rightarrow I}$) increase. [26] Park *et al.* observed the same trend for another chromonic material, Sunset Yellow (SSY), which is a food coloring azo dye. [24, 28] Kostko *et al.* found that the change in phase transition temperature depends on the type of added salts. Addition of salts with small cations increases the transition temperature, while salts with larger organic cations decrease it. [29] Addition of PEG has been shown to promote the formation of liquid crystalline phases for both DSCG and SSY through excluded volume effects. [28, 30] The extent of change depends on the molecular weight of PEG, that PEG with a molecular weight of 600 -1500 has no effects on the phase transitions. [31] Being able to accurately quantify the phase transitions of LCLCs and understand the mechanisms of self-assembly and aggregation are essential for the development of the potential applications.

The conventional methods for quantifying the phase transitions of LCLCs require samples with large volumes (> mL) and only provide phase diagrams with discrete data points. [28, 32–34] In addition, the identification of the phase transitions based on the observation of optical textural features by human eye is subjective and qualitative, which requires additional methodology such as x-ray scattering and NMR spectroscopy. It has been shown that image processing can be applied to quantitatively identify the phase transitions of LCs by computing textural features of the images recorded during the phase transitions. [35–38] In this chapter,

the droplet-based microfluidic device is applied to accurately quantify the phase transitions of SSY as concentration increases *in situ*. The device has been previously demonstrated to be able to accurately quantify the phase separation of multi-component systems. [39] The evolution of the phase transitions is real-time monitored under the crossed-polarized microscopy in the device. The phase transition mechanisms are studied by characterizing the effects of three different additives: salts, polymers, and nanoparticles on the phase transitions of SSY. A standard image processing technique, gray-level co-occurrence matrix (GLCM) has been demonstrated as a potential tool to identify various liquid crystalline phases.

6.2 *Materials and Methods*

6.2.1 *Materials*

Sunset Yellow FCF (SSY) with a dye content of 90%, polyethylene glycol (PEG) with molecular weight of 600 g/mol, 4 kg/mol, and 10 kg/mol are purchased from Sigma Aldrich (St. Louis, MO). Sodium chloride is purchased from Alfa Aesar (Haverhill, MA). Magnesium chloride is obtained from Thermo Fisher Scientific (Waltham, MA). All reagents are used without further purification. The stock solutions of SSY and additives are made individually by dissolving a known mass of solute in the deionized water (18.2 M Ω .cm). The sample solutions of SSY with additives are made by mixing the SSY stock solution and the additive stock solution in a specified molar ratio of SSY to additive, defined as ξ . The sample solution is

well-mixed before use. Figure 6.1 shows the chemical structure of SSY for reference. [40]

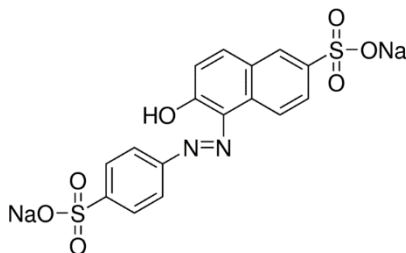


Figure 6.1 Chemical structure of SSY.

6.2.2 *Microfluidic shrinking droplets*

The phase transition is quantified using the droplet-based microfluidic device. The details for device fabrication and droplet generation is discussed in Chapter 2. 40 aqueous droplets containing dilute and well-mixed sample solutions are generated in the microfluidic channel surrounded by mineral oil. The dehydration process of all 40 droplets is monitored under a Nikon Ti-U microscope with crossed polarizers (10× mag, 0.65 $\mu\text{m}/\text{pixel}$) by taking sequential images every 2 min. At each time point, the entire device is automatically scanned in a zig-zag path across the device (Figure 2.1), taking an image of every droplet. The droplet diameter is analyzed using the image processing method developed in MATLAB. The diameter is used to calculate the droplet volume based on Eqn. (2.1) in Chapter 2, which is then converted to the concentration of solute based on mass balance. Details of droplet dehydration process and volume calculation can be found in Chapter 2. The increasing solute concentration is accurately tracked inside each droplet.

Figure 6.2 a) and b) illustrate the measured droplet diameter and calculated SSY concentration as a function of time, respectively for a typical droplet. The droplet is only allowed to shrink to the point that the diameter is comparable to the trap height, $100\ \mu\text{m}$, to maintain the pancake shape valid. Therefore, in this work, the initial droplet size and solute concentrations are chosen to have the transition occur while the droplet is still larger in diameter than the height of the device. As shown in Figure 6.2 a), while $D > h$, the diameter of the droplet decreases linearly with time until D reaches approximately $380\ \mu\text{m}$, which corresponds to nearly 1M of SSY concentration. The red dotted line shows the diameter and concentration based on the linear fit. The deviation in linearity when $D > 380\ \mu\text{m}$ may be because that the elevated concentration increases the viscosity of SSY solution, which hinders the transport of water and induces wetting to the channel, thus the droplet starts to deviate from the pancake shape. When concentration is larger than 1 M, we have less confidence in the measured results, which is indicated by the grey

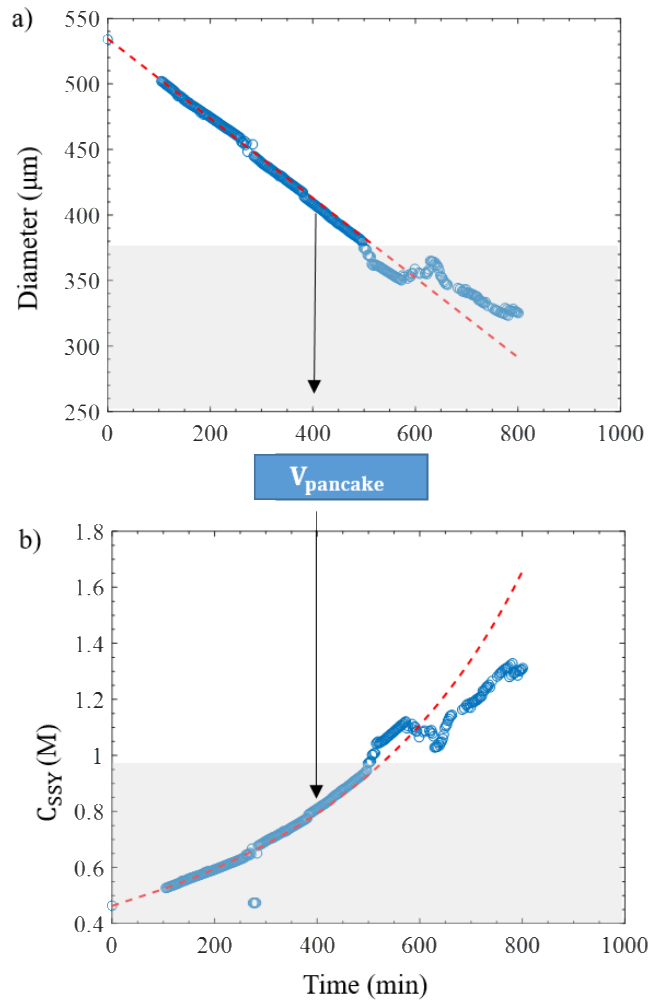


Figure 6.2 a) and b) show the measured droplet diameter and calculated SSY concentration, respectively, for a typical droplet. The dotted red line represents the linear fit. Gray shaded areas indicate the measurements with less confidence due to the deviation from the pancake shape.

shaded area in Figure 6.2. Droplets are dehydrated at room temperature ($22 \pm 1^\circ\text{C}$).

The dehydration rates are controlled by temperature, humidity, and device thickness.

The accuracy of concentration determined in the device depends on the homogeneity of the sample solution. A typical time for complete droplet shrinking is approximately 15 - 24 h under current lab conditions. By defining a 1-D flux

from the top of the device, water diffuses out at a typical rate of $10^{-3} \frac{g}{m^2 s}$. The diffusivity coefficient of water through mineral oil is estimated to be $10^{-12} \frac{m^2}{s}$. The Biot number defined as $Bi = \frac{l_c k_c}{D}$ is determined to be on the order of 10^{-1} by assuming a $100 \mu m$ characteristic length of the drop. The actual viscosity at the phase transitions studied in this work would be lower than the applied value, leading to a smaller Biot number. This further indicates a uniform droplet concentration.

6.2.3 Theory of Gray-Level Co-Occurrence Matrix

Gray-level co-occurrence matrix (GLCM), which is a second-order statistical method for image texture analysis in terms of the spatial distribution of pairs of pixels, [42, 43] is applied for detecting the phase transitions of SSY with or without additives. Four second-order statistical texture features are extracted from GLCM, which are energy, entropy, contrast and homogeneity. For a GLCM with number of gray levels of N , $p(i, j, d, \alpha)$ represents the occurrences of pairwise gray levels, i, j with a separate distance d , and a specified angle α . [43] The four statistical parameters are calculated by the following formulas.[38, 42, 43]

- 1) Energy measures the uniformity, namely, the pixel pair repetitions.

$$\text{Energy} = \sum_{i=1}^N \sum_{j=1}^N (p_{(i,j)})^2 \quad (3.1)$$

- 2) Entropy is a measure of disorder of the image.

$$\text{Entropy} = - \sum_{i=1}^N \sum_{j=1}^N p_{(i,j)} \log(p_{(i,j)}) \quad (3.2)$$

- 3) Contrast measures the local variations of intensity in the GLCM.

$$\text{Contrast} = \sum_{i=1}^m \sum_{j=1}^n (i - j)^2 p_{(i,j)} \quad (3.3)$$

- 4) Homogeneity measures the closeness of pairwise pixels in the GLCM to the GLCM diagonal.

$$\text{Homogeneity} = \sum_{i=1}^N \sum_{j=1}^N \frac{1}{1+(i-j)^2} p_{(i,j)} \quad (3.4)$$

In this chapter, energy, entropy, contrast and homogeneity are calculated as a function of time for the sequential images obtained from the evaporation experiments.

6.3 *Results and Discussions*

6.3.1 *Observation of birefringence in the microfluidic device*

Figure 6.3 represents the dehydration sequence of a typical droplet containing dilute sunset yellow (SSY) aqueous solution observed through a crossed-polarized microscopy in the microfluidic device. Images are captured every 2 min and the entire dehydration takes approximately 24 h. Images in the figure are at various time intervals, illustrating the droplet shrinking process. Dim light from the environments can pass through the crossed polarizers. Even though the image appears black, by adjusting the contrast using the image analysis tool, the droplet outline can be observed, which enables the measurement of droplet diameter. The dashed circles show the outline of the droplet. Initially, the droplet contains dilute SSY solution with a concentration of 0.44 M and the system is isotropic (I) as shown in image 1, where the droplet appears black through the crossed polarizers. As water evaporates, the droplet shrinks in size and the concentration of SSY

increases. The first observation of birefringence is seen as bright spots as shown in image 2. Birefringence continues to grow with time as well as the increasing SSY concentration as shown in image 3. At some point, the bright spots coalesce into one homogenous phase (image 4). Then a different texture develops in the droplet and finally a sharp line texture appears, which are shown as images 5 and 6. It is known that SSY undergoes various phase transitions as concentration increases. [28, 32, 33] We first focus on the phase transition when birefringence appears

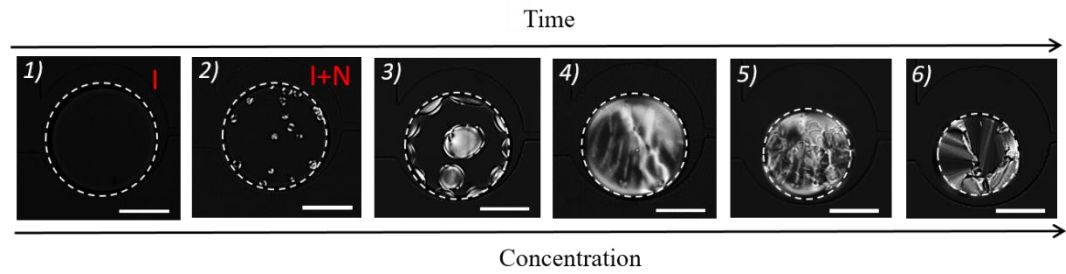


Figure 6.3 Representative dehydration process of a droplet containing dilute sunset yellow aqueous solution captured under the polarizing microscope with polarizers crossed in the microfluidic device. Dashed circles outline the representative droplet for clarity. White bars are equivalent to 200 μm . The occurrence of the bright spots, shown by image 2), indicates the onset of isotropic (I) to isotropic + nematic (I+N).

(images 1 to 2). The dehydration process is monitored for all 40 droplets and the droplet diameter is measured as a function of time for each droplet, which is used to calculate the SSY concentration. Due to the variation in the location on the device, the droplets undergo different evaporation rates. Therefore, the occurrence of birefringence is observed at different time frames for each droplet across the device. The concentrations at which the birefringence is first observed, C_B , are essentially the same for all droplets, which is determined as 0.66 ± 0.002 M. The small standard deviation indicates the high reproducibility of our results. The 40 droplets are equivalent to 40 repetitions of the experiment, which provides high statistics. The determined C_B is consistent with the transition concentration of I to I+N

coexistence phase obtained from the literature, 26.5 wt%, which is equivalent to 0.67 M, converted based on the provided formula. [28] For the comparisons in the rest of the chapter, the unit of the concentrations from the literature are all converted from wt% to M by the same method. The small deviation can be induced by the difference in impurities and degree of dehydration of sunset yellow. [24] Therefore, macroscopic experiments are performed and the result is consistent with the microfluidic experiment. Details can be found in the next section. In addition, the bright spots seen in the polarizing microscopy show a similar texture to the I+N coexistence phase classified in the literature using the same optical techniques. [24, 28] Overall, the occurrence of birefringence indicates the onset of I to I+N coexistence phase transition, which can be easily detected and accurately quantified in the microfluidic droplets. By tuning the time interval of image acquisition, the phase transition can be quantified with various compositional resolutions. Loading of this device requires small volumes (<mL) of dilute sample and provides highly accurate results for the lyotropic phase transition.

6.3.2 *Macroscopic experiments*

For the macroscopic experiment, concentrated SSY solutions are produced from dilute samples using Rotovap and are well mixed before taking observations. Arrays of 1mm capillary tubes are used, each filled with a different concentration of SSY solution and two ends are sealed with the epoxy glue to prevent water evaporation, which is shown in Figure 6.4 (top). Then the arrays are put on a glass slide and are observed through the crossed-polarized microscope with $4\times$

magnification at room temperature. A clear visual difference is observed between the two states: the isotropic sample appears to be dark and the birefringent sample is bright and tinted red as shown in Figure 6.4 (bottom). The concentration at which birefringence is first observed falls between 0.68 M and 0.70 M, which is close to the microfluidic result, 0.66 M.

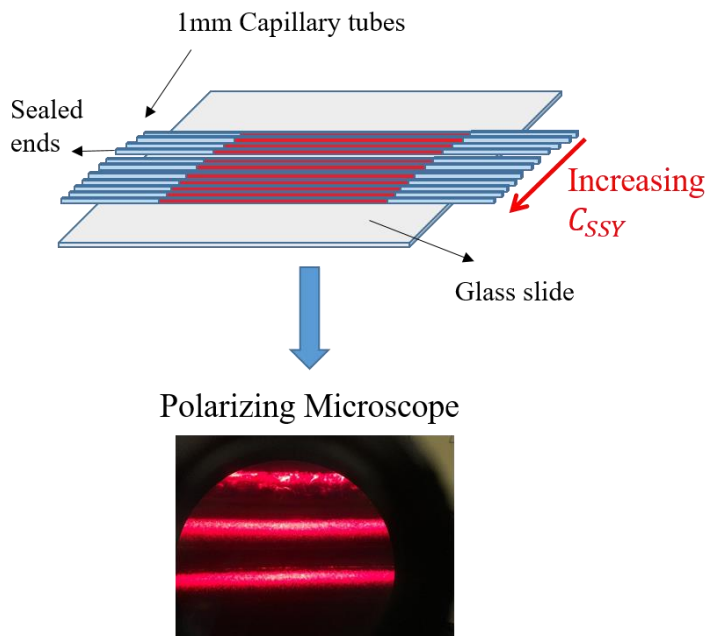


Figure 6.4 A schematic of the macroscopic experiment. SSY at various concentrations are loaded into the 1mm capillary tubes, which ends are sealed with epoxy glue to prevent water evaporation. The tubes are observed under the crossed-polarized microscope. A clear visual difference is observed for samples that are isotropic and birefringent, which appear to be dark and tinted red, respectively.

6.3.3 Quantification of colloidal effects on the I to $I+N$ transition

Phase transitions in SSY are induced by the process of reversible self-assembly and packing of the mesogens, which can be affected by additives through two main mechanisms: 1) electrostatic screening and 2) excluded volume effects. [28] Since birefringence can be easily detected in the microfluidic droplets and

applied to quantify the phase transition of SSY, in this work, we studied the effects of additives on the I to I+N phase transition using the microfluidic device.

Electrostatic screening

SSY mesogens are highly charged in solution due to the dissociating sulfonate groups in the structure, [24] and salts affect the phase transition of SSY through electrostatic screening by affecting both the intra and inter-aggregate interactions. To tune the screening effect, two types of salts with different valencies: NaCl and MgCl₂ are added into the SSY solution, respectively. Figure 6.5 illustrates the concentration at I to I+N transition (C_{I+N}), which is signified by the occurrence of birefringence, as a function of the molar ratio of salt to SSY for NaCl (circles) and MgCl₂ (squares), respectively. The dotted lines are drawn to guide the eyes. The triangle on the y axis indicates C_{I+N} for SSY without salt, determined to be 0.66 ± 0.002 M previously. As shown in Figure 6.5, for both salts, C_{I+N} decreases with increasing salt concentration. In addition, MgCl₂ causes a more significant reduction in C_{I+N} compared to NaCl. These results are consistent with the trends observed in the literature, where the reduction in C_{I+N} is explained by the salt-induced electrostatic screening of the repulsive interactions between the SSY aggregates. [24, 28] The inset in Figure 6.5 indicates C_{I+N} as a function of Debye length, $\lambda_D = \left(\frac{1}{e}\right) (\epsilon \epsilon_0 k_B T / \sum_i C_i q_i^2)^{\frac{1}{2}}$, which is a function of both the concentration and valence of the added salt. As expected, the higher the salt concentration and valency, the smaller the λ_D , therefore the larger the reduction in C_{I+N} . In addition, salts screen the electrostatic repulsions between the charged SSY

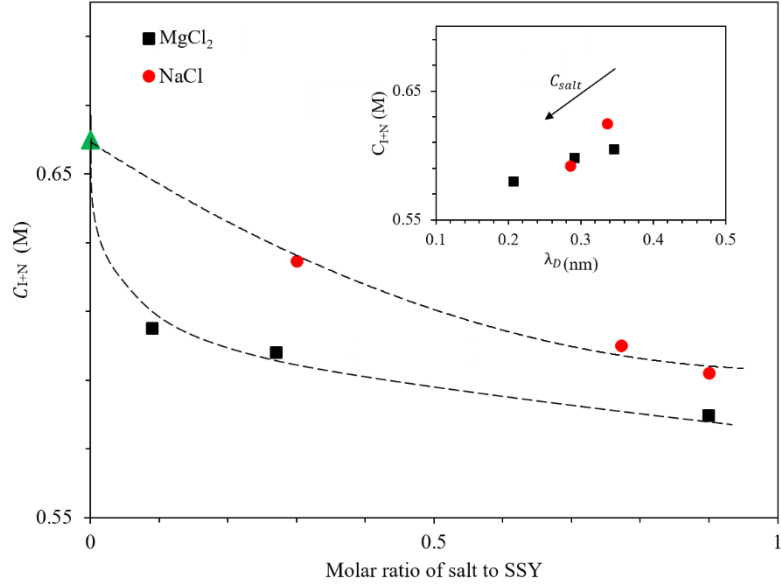


Figure 6.5 C_{I+N} as a function of molar ratio of salt to SSY for two types of salts: NaCl and $MgCl_2$, which are represented by the circles and squares, respectively. The triangle on the left axis represents C_{I+N} without salts. The dotted lines are drawn to guide the eyes. The inset illustrates C_{I+N} as a function of Debye length. The arrow indicates the increase in the salt concentration.

molecules, which promotes the face-to-face stacking and facilitates the elongation of aggregates. [24, 28] The phase transition concentration is a strong function of aggregate (mesogen) length as illustrated in Eqn. (3.5), where L is the length of aggregates and d is the diameter of the SSY molecule. [44] Therefore, increasing the length of the aggregates reduces C_{I+N} as

$$C_{I+N} \sim \frac{1}{dL^2} \quad . \quad (3.5)$$

Excluded volume

In addition to electrostatic screening, additives can alter the phase transition through excluded volume effects. Polyethylene glycol (PEG) is an effective depletant in aqueous suspensions and has been shown to promote the formation of

liquid crystal phases through the depletion effects. [28, 30] In this work, PEG (MW = 4 kg/mol) is added to the SSY solution with various molar ratios of SSY to PEG. Figure 6.6 shows the SSY concentration, C_{SSY} , as a function of PEG concentration, C_{PEG} , measured in the microfluidic device. Each dotted line represents one droplet shrinking experiment where the slope is set by ξ , defined as the molar ratio of SSY to PEG. For each experiment, the open circle represents the initial solute concentration. The molar ratio of initial solution, and hence the slope, is precisely controlled. As water evaporates, the concentration of both SSY and PEG increases,

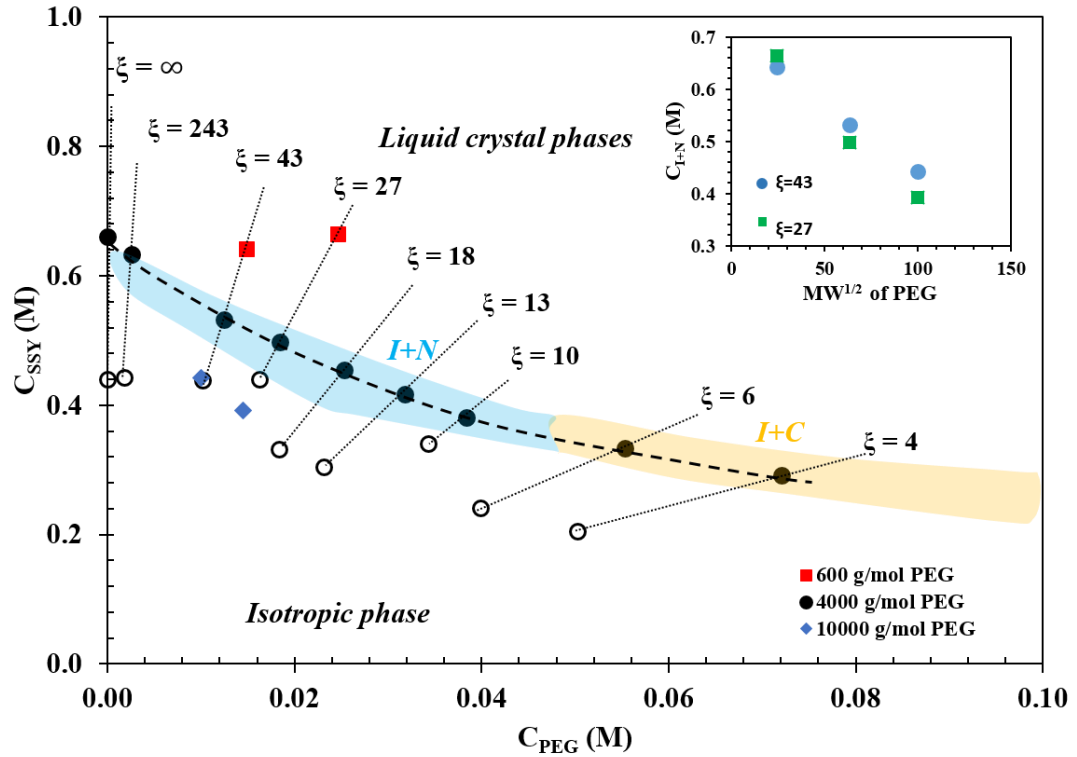


Figure 6.6 Phase diagram of SSY, PEG, and water mixtures established via the microfluidic experiments. The filled squares, circles, and diamonds represent the solute concentrations at phase transition for 600 g/mol, 4000 g/mol, and 10000 g/mol PEG, respectively. Each dotted black line represents one droplet shrinking experiment and the slope indicates a constant molar ratio of SSY to PEG (ξ). Open circles indicate the initial solute concentrations for SSY with 4000 g/mol PEG. The colored shaded areas represent the concentration intervals where phase transitions occur obtained from Park H.S. *et al* (2011). The inset shows the phase transition concentration, C_{I+N} , as a function of $MW^{1/2}$ of PEG for ξ of 27 (squares) and 43 (circles).

represented by following along the dotted line. The filled circle represents the solute concentration at which birefringence is first observed, which indicates the transition from the isotropic to the liquid crystal phase. The bold dashed line represents the phase boundary determined by the microfluidic experiments, which separates the isotropic phase from the liquid crystal phases. The blue and yellow shaded areas represent the concentration interval where the I to I+N and I to I+C phase transitions occur, respectively, for PEG with MW of 3350 g/mol, which are taken from the ternary phase diagram in Park, H.S. *et al* (2011). [28] The phase boundary line determined using the microfluidic device is consistent with the literature results. Instead of an interval, the microfluidic device is able to provide a phase boundary line composed of exact data points with significantly improved compositional resolution. And less than a milliliter of SSY solution is needed to establish this phase diagram.

As shown in Figure 6.6, C_{SSY} at phase transition decreases with increasing PEG concentration as has been observed. [28] This is due to the PEG-induced depletion attraction, which promotes both the face-to-face stacking of the SSY molecule and the side-by-side packing of the aggregates. [24, 28] PEG, excluded from the SSY molecules, exerts an osmotic pressure gradient within the solvent and a force on SSY mesogens, which increases with increasing PEG concentration, c , as shown in Eqn. (3.6),

$$\frac{\pi}{RT} = \frac{c}{M} + Bc^2 + B_3c^3 + \dots, \quad (3.6)$$

where R is the gas constant, T is the temperature, M is the molecular weight of PEG, and B is the second virial coefficient. [45] At the liquid crystal phase, the osmotic pressure balances with the electrostatic repulsions of the charged SSY aggregates, which correlates with the inter-aggregate distance, D , and Debye length, λ , by Eqn. (3.7),

$$\pi = \sqrt{6\pi}\tau_{eff}^2 \frac{4k_B T}{d_{SSY}^2 l_B K_1^2(\frac{d_{SSY}}{2\lambda})} \left(\frac{\lambda}{D}\right)^{3/2} \exp\left(-\frac{D}{\lambda}\right) \quad (3.7)$$

where K_1 is the first-order modified Bessel function of the second type, l_B is the Bjerrum length at room temperature, d_{SSY} is the diameter of a charge SSY aggregate, and τ_{eff} is the effective charge density. [28] At the liquid crystal phase, D is fixed. λ is positively correlated with osmotic pressure as shown in Eqn. (3.7). As more PEG added, the larger the osmotic pressure can be provided, therefore the larger λ . Since λ is inversely related to the SSY concentration, the higher the PEG concentration, the lower the SSY concentration required at the liquid crystal phase transition.

In addition, the excluded volume effect depends on the size of the depleting agent. Studies have shown that PEG with molecular weight of 600 – 1500 g/mol has no effect on the phase transition of LCLCs. [31] To test this mechanism, PEG with two other molecular weights: 600 g/mol and 10 kg/mol are added into the SSY solution at ξ of 27 and 43, respectively. In Figure 6.6, the diamonds and squares represent the phase transition concentrations determined by the microfluidic device for 600 g/mol and 10 kg/mol PEG, respectively. 600 g/mol PEG has no effect on the phase transition concentration, while 10 kg/mol PEG reduces the concentration

to a larger extent than 4 kg/mol PEG, which is consistent with the literature. [28, 31] This is because that PEG with a larger molecular weight has a larger size, such as the radius of gyration, which is proportional to the $MW^{1/2}$ by assuming unperturbed coil. [45] Therefore, it is easier to be excluded from the SSY aggregates and induces depletion attraction between the SSY aggregates, thus promoting the ordering within the aggregates and the phase transition. This is confirmed by the inset in Figure 6.6, which represents the phase transition concentration as a function of $MW^{1/2}$ for two molar ratios ξ of 27 (squares) and 43 (circles). The larger the MW, the larger the reduction in the phase transition concentration.

Nanoparticles have been shown to also affect the phase transition of liquid crystals through excluded volume effects by confining the LC in the network of flocs of nanoparticles. [46–48] In this work, two types of silica particles, Ludox-AM ($d = 7$ nm) and Ludox-TMA ($d = 22$ nm) are added to the SSY solution. Figure 6.7 shows the phase diagram of SSY with Ludox-AM (squares) and SSY with Ludox-TMA (circles) at various molar ratios of SSY to Ludox (ξ). For Ludox-AM, at ξ of 1 and 5, addition of SSY significantly reduces the volume fraction of Ludox-AM at gelation, which is observed as the wrinkled drop edge shown in image 1. The SSY solution undergoes phase transition after the gelation, illustrated by the occurrence of bright spots in image 2. Since the droplets deviate from the pancake shape after gelation, the phase transition concentration can not be determined. Therefore, the concentration of Ludox-AM is reduced ($\xi = 30$). Similarly, Ludox-TMA is added to SSY at $\xi = 30$. For both silica particles, no gelation is observed at

the phase transition, which is indicated by the circular droplet shown in image 3. The dashed dotted line separates the ξ with and without gelation and is drawn to guide the eyes. Furthermore, there is no change in C_{I+N} with both types of Ludox at $\xi=30$ and the mechanism of phase transition is similar to the pure SSY as shown

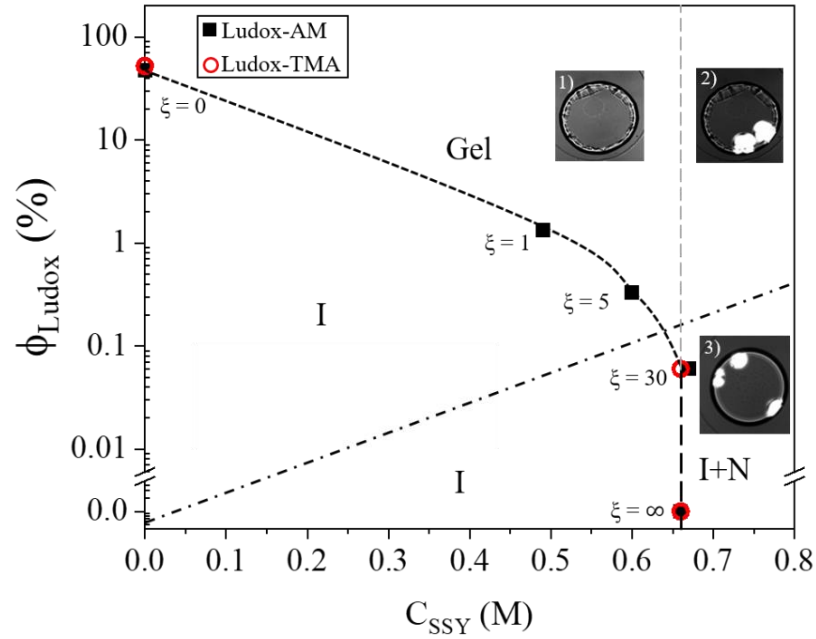


Figure 6.7 Phase diagram of SSY with Ludox-AM (squares) and SSY with Ludox-TMA (circles) at various molar ratios of SSY to Ludox (ξ). The vertical dashed line and the bold dashed line represent the boundaries for I to I+N phase transition and gelation, respectively. The dotted dashed line separates the ξ with or without gelation, which is drawn to guide the eyes. Images 1-3 show a gelled droplet, a gelled droplet at I to I+N phase, and a droplet at I+N phase without gelation, respectively.

in Figure 6.8. However, the addition of both types of silica particles promotes the formation of a fewer number of larger birefringent domains. It is interesting that by adding Ludox-TMA, birefringence starts to form from the center of the droplet and then expanded through the entire droplet as water evaporates (image 6 – 10 in Figure 6.8), which is different from Ludox-AM and all the other systems. Ludox-TMA has a larger diameter ($d \sim 22\text{nm}$), which provides a stronger depletion attraction between SSY aggregates. In addition, Ludox-TMA may form

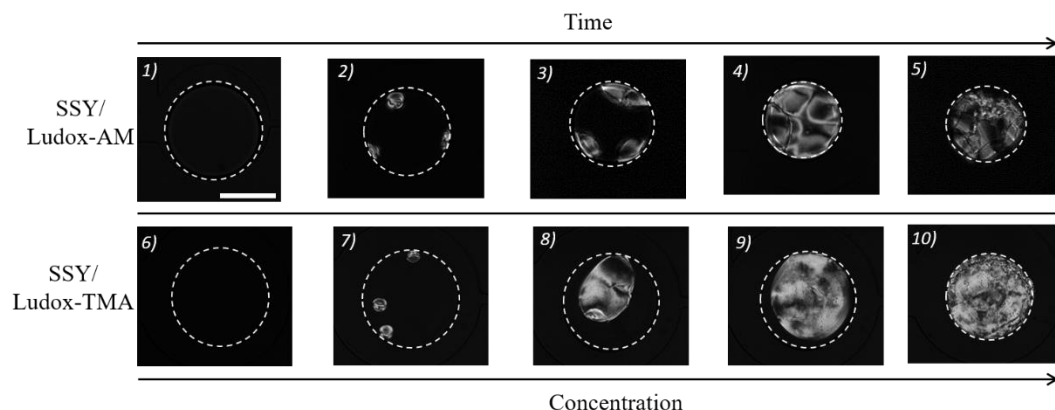


Figure 6.8 Dehydration sequence of a typical droplet containing SSY solution with Ludox-AM (top row) and Ludox-TMA (bottom row) at $\xi = 30$. The dashed lines outline the droplets for clarity. White bars are equivalent to 200 μm .

nanoparticle aggregates at the boundary of the droplet interface, thus promoting the formation of nematic phase at the inner region of the droplet. The mechanism of interactions between Ludox and SSY requires further examination. Overall, we have demonstrated that the microfluidic device is able to efficiently and accurately quantify the effects of additives on the I to I+N phase transition of SSY with high composition resolution.

6.3.4 *Potential of image analysis for identification of phase transitions*

The evolution of the phase transitions of the SSY solution with or without additives are live monitored during the dehydration experiments, therefore, besides the I to I+N phase transition, which has been extensively discussed in the previous sections, the sequential images also contain critical information of other liquid crystalline mesophases. As shown in Figure 6.3, various optical texture features are observed as SSY gets concentrated in the shrinking droplet and have been used to identify the phase transitions in the literature. [28] However, unlike the I to I+N

phase transition, which can be easily identified by eyes based on the occurrence of birefringence, other LC phases, such as nematic (N) and columnar (C) phases, gradually evolve with more complex textures and are hard to be identified due to the lack of the on-and-off features such as the occurrence of birefringence.

In addition, three different mechanisms of phase transitions are observed for SSY with PEG. As shown in Figure 6.9, the addition of PEG at low concentration ($\xi = 243$) exhibits the same phase transition mechanism as the systems of pure SSY and SSY with salts (Figure 6.9 images 1 – 6) as described previously. By increasing the PEG concentration ($\xi = 43, 27, 18, 13, 10$), instead of forming one homogenous phase, the bright spots stop coalescing at some point during the dehydration as shown in Figure 6.9 image 7 - 12. The images are taken from the dehydration process of a typical droplet with $\xi = 43$ as the representative example. With an even higher PEG concentration ($\xi = 6, 4$), the bright spots barely grow in both size and quantity right after the appearance as shown by Figure 6.9 image 13 – 16, which are taken from the dehydration process of a droplet with $\xi = 6$ as the representative example. These three phase transition mechanisms contain

different textural features, such as the number of bright spots, smoothness, and contrast, which can be captured and differentiated by eyes but is less objective and also the eye-picking process for over 10,000 images from 40 droplets is time-consuming.

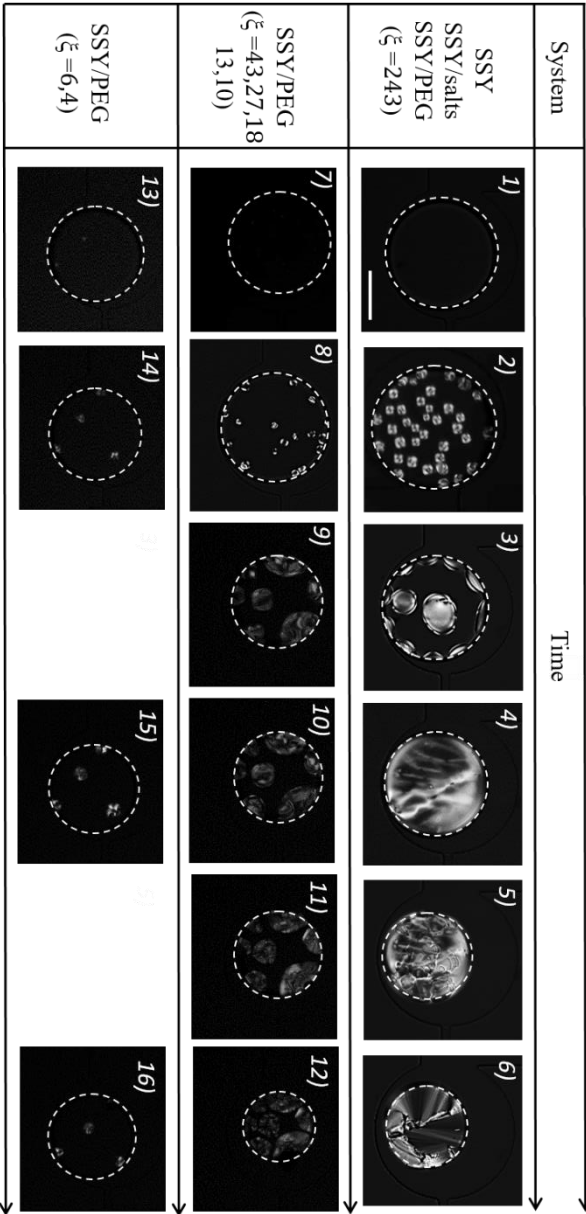


Figure 6.9 Optical textures of SSY, SSY/ salts, and SSY/ PEG with various ξ during the dehydration process for a representative droplet. Dotted lines outline the droplets for clarity. The arrow points in the direction of increasing time and solute concentrations.

To solve this issue, image analysis techniques are applied with the intent of objective and automatic identification of the phase transitions and the transition concentrations. The advantage of the microfluidic device is that the entire evolution process of the phase transition is live monitored with high temporal resolution, which produces a stack of sequential images containing essential texture features as a function of time. Since the solute concentration can be determined at each time point, the textural features are tracked as a function of solute concentration. In this work, the standard image analysis technique, gray-level co-occurrence matrix (GLCM), is applied to extract four second-order statistical parameters: entropy, energy, contrast, and homogeneity based on the spatial distribution of the gray level intensities of the textures. [42] In addition, the number of bright spots is applied as the fifth parameter, which is analyzed using the image processing tool in MATLAB.

Starting from the phase transitions for pure SSY solution, Figure 6.10 shows the five parameters mentioned above as a function of SSY concentration for one representative droplet. Variations in the magnitude of parameters are caused by the transition in phases, which induces changes in the textural features of the images. Therefore, the concentrations at which the abrupt changes are observed indicate the phase transition concentrations. The asterisks represent the abrupt changes obtained by finding the top five abrupt changes in the 1st derivative of the curve. Each parameter provides five transition concentrations. The vertical dotted lines indicate the SSY concentrations at which distinct change in the texture is captured by the human eye. The dotted lines from left to right represent transitions A-E, respectively, which are indicated by inset A-E. The observations for each transition

are described in the top right table of Figure 6.10. As shown in Figure 6.10, the transitions of A, C-E can be successfully detected by the five parameters, indicated by the consistency with the phase transition concentrations determined by the human eye. To be mentioned, the structural patterns inside each bright spot, such as the bipolar and radial configurations at the early stage of appearance, generate both bright and dark regions within one bright spot (image A), which requires the

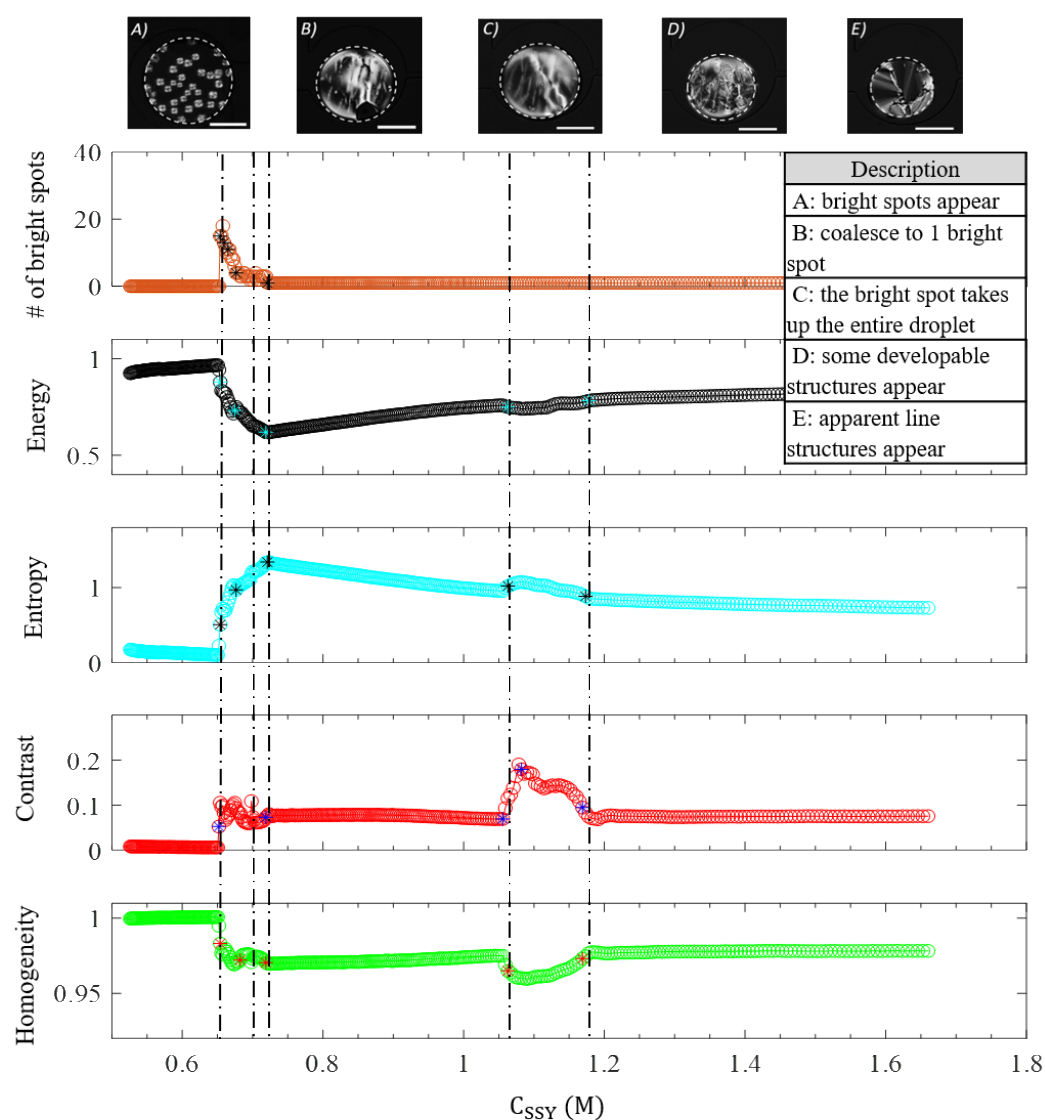


Figure 6.10 Computed parameters from the textures of pure SSY as a function of SSY concentration. The asterisks indicate the concentrations for phase transitions identified by image analysis. The 5 vertical dotted lines show the phase transitions identified by the human eye. The corresponding polarizing images are indicated as inset A-E, respectively. The table summarizes the observations for each transition.

algorithm to be intelligent enough to properly group all the small bright regions together and segment them as a single bright spot. In this work, the number of bright spots is determined by counting the number of white regions with areas above a threshold value in the droplet without the intelligent group. Therefore, the number of bright spots is not accurate and can not be used to fit the nucleation and growth model. However, it is robust to capture the occurrence of the bright spots, shown by the sharp increase in the magnitude from zero to a certain value. And in this case, it also captures the coalescence to one homogenous bright spot indicated by reaching to one at high SSY concentrations.

To test the efficiency and robustness of the image analysis technique in identifying the phase transitions, the same procedures are performed for the rest of 39 droplets. There are 26 good droplets out of 40. The bad ones are either due to the failure in the droplet production or inappropriate wetting. Figure 6.11 shows the five parameters as a function of SSY concentration for all 26 droplets. The asterisks indicate the SSY concentrations at abrupt changes in the magnitude of the parameters identified by the same method as described above. The number of bright spots, energy, and entropy all detect a transition at 0.66 M, at which birefringence is first observed, as shown by inset A) in Figure 6.10. The value of the concentration is determined by averaging the concentrations at the first abrupt change over all 26 droplets. Both energy and entropy detect a second sharp transition at 0.71M, at which the coalesced one bright spot takes up the volume of the droplet as shown by inset C) in Figure 6.10. These two detected concentrations are consistent with the concentrations at I to I+N and I+N to N phase transitions, respectively, determined

from the literature as summarized in Table 6.1, and the optical textures also show agreement. [28] These three parameters are less effective for detecting transition D and E. Conversely, a wide distribution of peak concentrations is observed in both contrast and homogeneity between SSY concentrations of 0.9 M and 1.3 M as

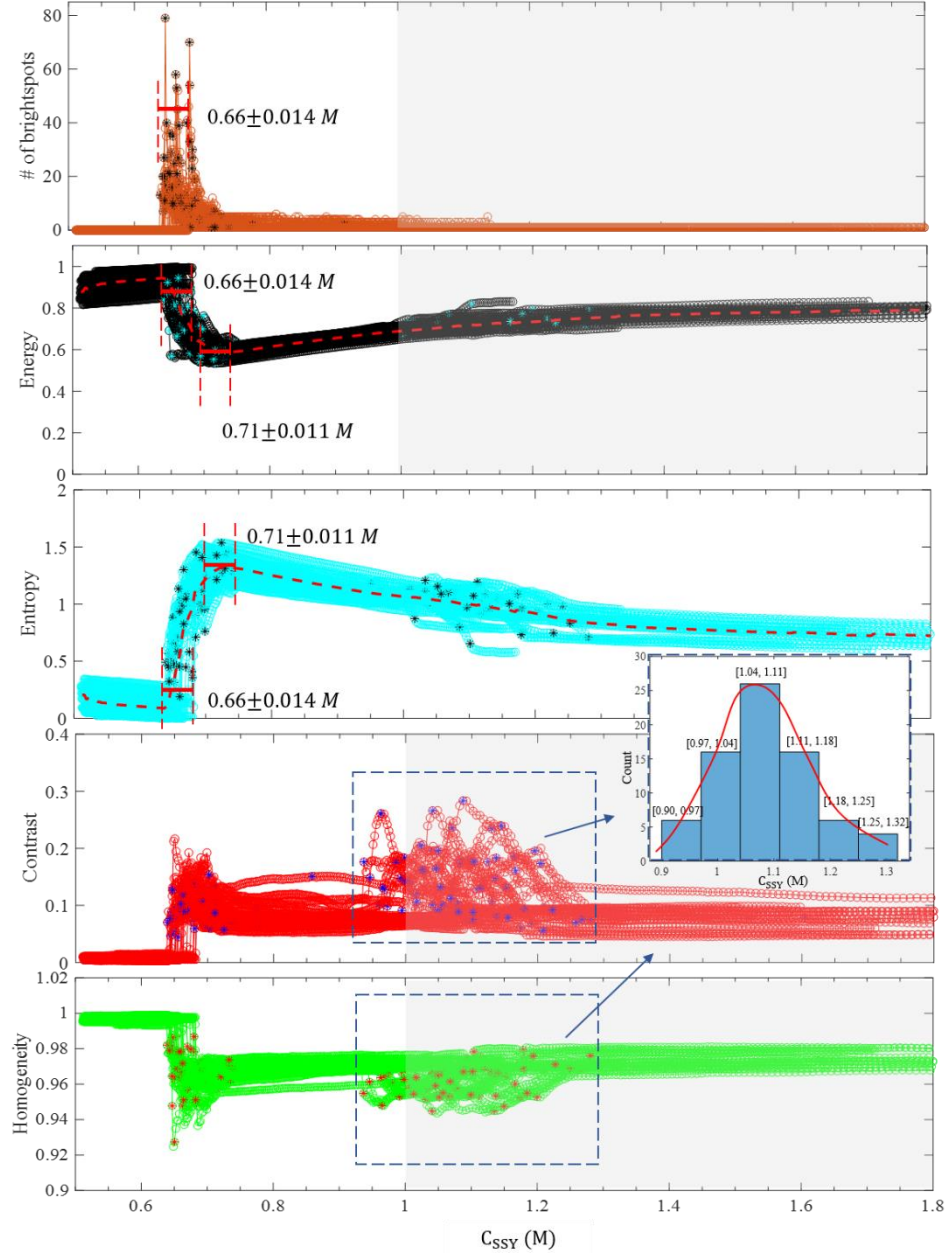


Figure 6.11 Computed parameters from the textures of pure SSY as a function of SSY concentration for 26 droplets. The asterisks indicate the concentrations for phase transitions identified by image analysis. Inset indicates the distribution of peak concentrations between SSY concentrations of 0.9 to 1.3M as highlighted by the dashed rectangles.

highlighted by the dashed rectangles. The distribution is plotted in the inset, showing a bell-like shape close to the Gaussian distribution indicated by the red line, which is drawn to guide the eyes. Concentrations between 1.04 M and 1.11 M show the maximum occurrence, which is close to the concentration at columnar (C) phase determined from the literature as tabulated in Table 6.1. In addition, concentrations at transition D and E fall in the concentration range of 0.9M to 1.3M and show the same optical textures as that of N+C and C phases observed in the

Table 6.1 Identified transition concentrations by statistical parameters compared with that determined by literature.

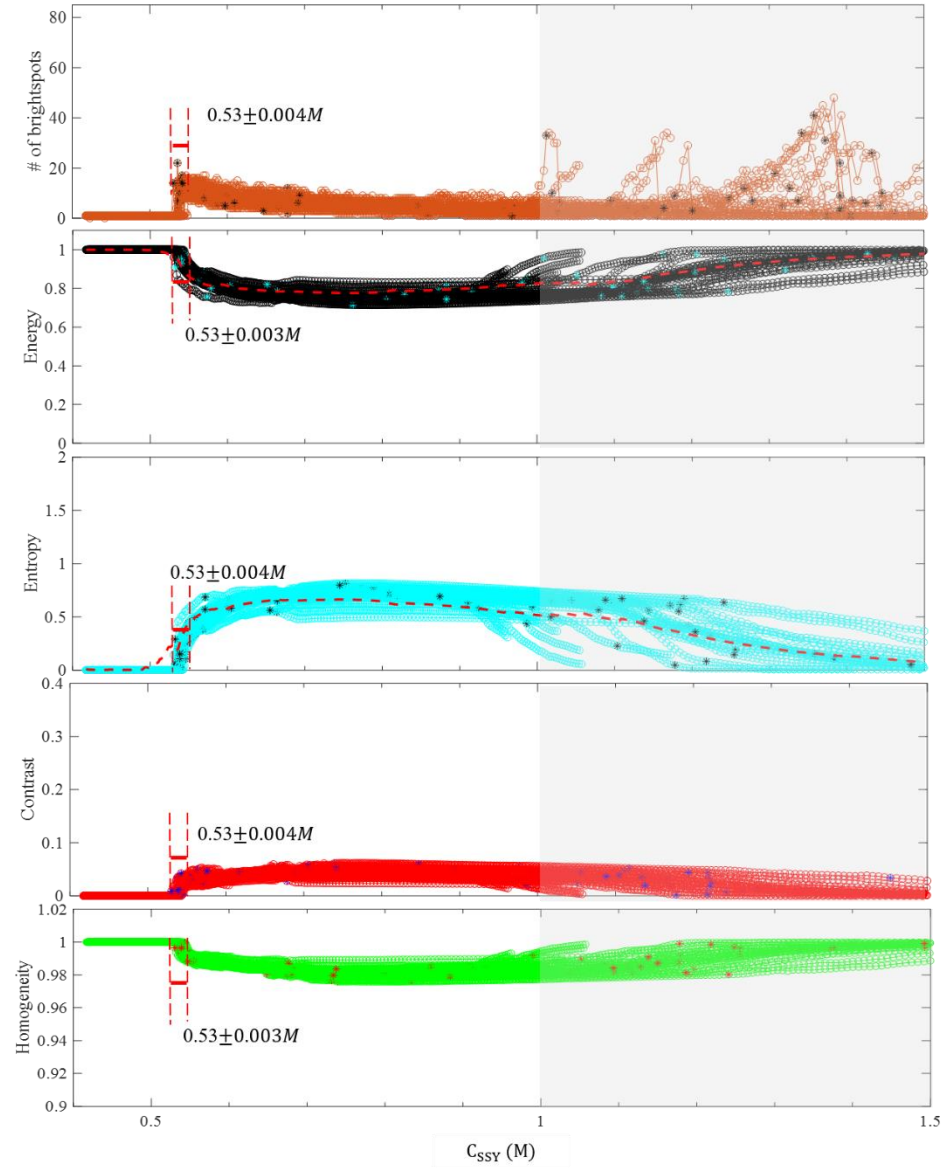
Image Analysis C_{SSY} (M)	Literature C_{SSY} (M) [15]	Literature LC phases [15]
0.66	0.67	I+N
0.71	0.71	N
0.9 – 1.3	0.91	N+C
	0.95	C
	1.39	Crystal

literature, respectively. [28] The wide distribution in peak concentration could first be due to the less confidence in the concentration measurements at concentrations larger than 1M, indicated by the gray shaded area. In addition, SSY at concentrations between 0.9 M and 1.3 M is approaching to the columnar and crystal phases, which are more kinetically controlled. The dehydration rate of the droplets may not be slow enough to capture these phase transitions. Even though the I+N and N phase transitions also involve the nucleation and growth mechanism, it can be clearly seen in Figure 6.11 that their time scales are different from the N+C and C phases. The dehydration time scale of the droplets needs to be properly tuned to

match the growth rate in order to capture the target phase transitions. In addition, a better fitting to the Gaussian distribution can be obtained by increasing the statistics, which is the number of droplets. We have designed a microfluidic channel with more than 100 droplet traps, therefore, it is feasible. Overall, we have shown that the five parameters are able to detect the phase transitions of I to I+N and I+N to N accurately. Different timescales for transitions of N+C and C phases are observed. In addition, the developed algorithm can perform the phase identification automatically, which significantly improves the efficiency.

For SSY with PEG systems, the five computed parameters as a function of SSY concentration for all good droplets are plotted as shown in Figure 6.12 a) and b) for $\xi = 43$ and 6, respectively, which are chosen as the representative cases for the two different mechanisms as discussed previously. The parameters are plotted in the same y-scale as Figure 6.11 for the ease of magnitude comparison. For $\xi = 43$ (Figure 6.12a), a sharp transition is detected by all five parameters at 0.53 M, which falls in the concentration range of I to I+N phase transition determined by the literature. [28] The peak value of the number of bright spots is roughly 3 times smaller than that of the pure SSY. In addition, instead of a sharp decrease, a much less degree of decrease in the magnitude is observed, suggesting less number of bright spots at I to I+N phase transition and less extent of coalescence as the concentration increases, which are consistent with the visual observation shown by images 7-12 in Figure 6.9. As droplet shrinking, the bright spots move close to each other as shown by images 9-12 in Figure 6.9, and the black and white regions in the bright spots (image 12) make the segmentation even harder. Therefore there is a

large variation in the magnitude of the number of bright spots especially at high SSY concentrations. After approximately 0.55M, insignificant change in the magnitude of the GLCM parameters suggests less variation in the textures during the phase transitions, which is consistent with the optical observation that the bright spots stop to coalesce at some point and maintain the same texture as droplet shrinking. In addition, when concentration is larger than 0.8M, SSY starts to



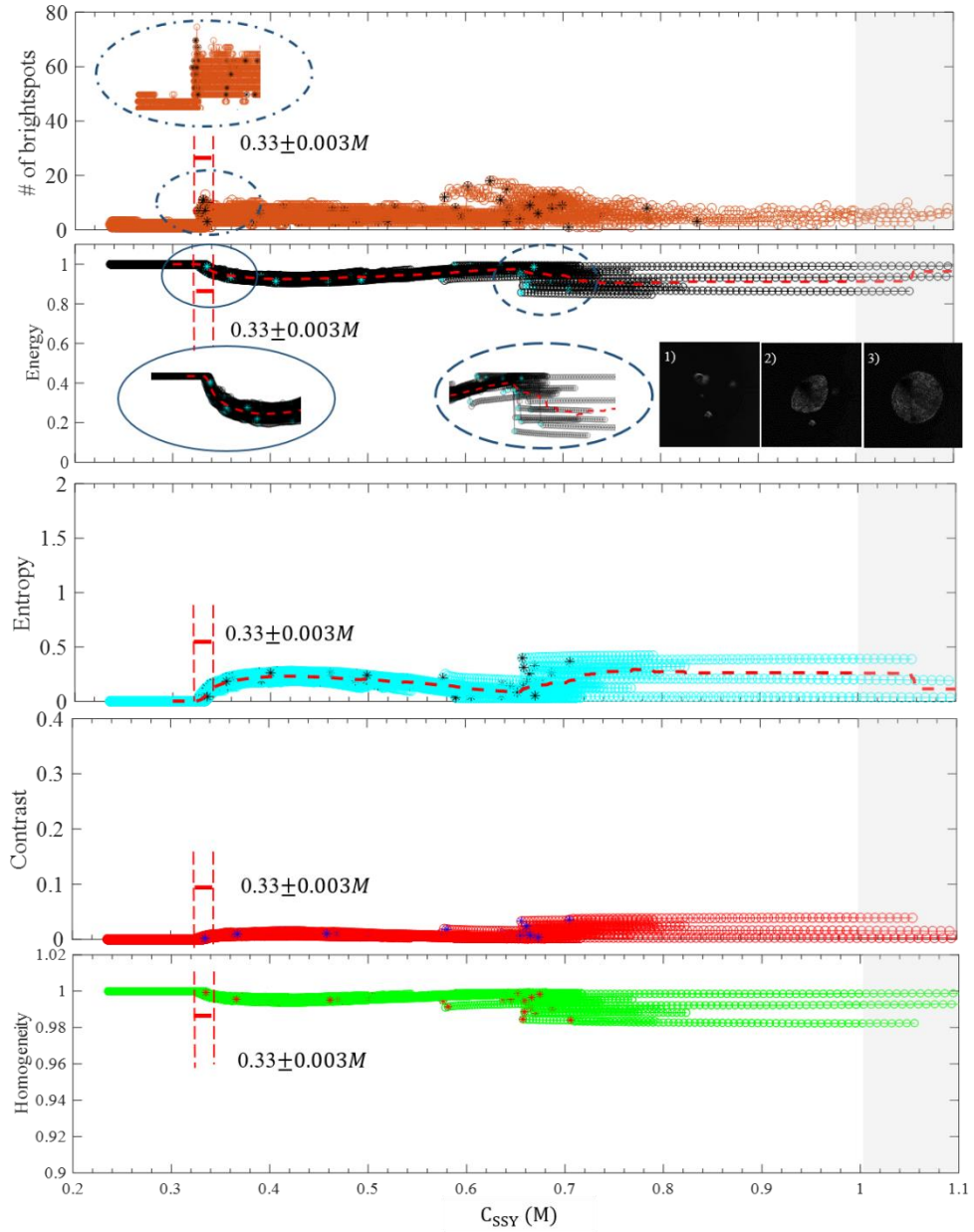


Figure 6.12 Computed statistical parameters from the textures for SSY with PEG: a) $\xi = 43$, b) $\xi = 6$. In b), the insets illustrate the zoom in of the circled regions. Image 1-3 show the transition of PEG crystallization, which induces the change in the magnitude of all five parameter at approximately $0.68M$ to $0.70M$.

crystallize, at which the droplet completely dehydrates and appears to be black, thus there is a sudden increase or decrease to the initial value in the four GLCM parameters.

For $\xi = 6$ (Figure 6.12b), a sharp transition is detected by all five parameters at 0.33M, which falls in the concentration range of I to I+C phase transition determined by the literature. [28] The number of bright spots barely changes as SSY concentration increases. An even smaller extent of change in the GLCM parameters are observed, which is consistent with the optical observations that the bright spots barely change in both size and quantity after appearance, so does the textures of the image as shown by images 13-16 in Figure 6.9. The insets show the magnified images of the circled regions for a clearer visualization. At approximately 0.68 M to 0.70 M, a transition is observed in all five parameters. This is due to the crystallization of PEG, which causes the small bright spots dramatically grow in size and expand to the entire drop as illustrated by image 1-3.

Overall, we have demonstrated that the image analysis technique is able to identify the I to I+N and I to I+C phase transitions for SSY with PEG and the distinct difference in the magnitude of the five parameters can be applied to differentiate the mechanisms. In the future, more intelligent segmentation algorithm can be applied for accurate counting of the number of bright spots, which could be applied as a potential tool of to differentiate the phase transition mechanisms and determine the concentrations at which the bright spots coalesce to one continuous phase for pure SSY and the concentration at which the bright spots stop to coalesce for $\xi = 43$.

6.4 Conclusions:

In this chapter, we have demonstrated that the phase transitions of SSY with and without additives can be quantified using the droplet-based microfluidic device implemented with crossed-polarized microscopy with significantly improved compositional resolution. Less than a milliliter of dilute SSY solution is required to establish the phase diagram, demonstrating the potential of the microfluidic device to quantify phase transitions of materials with limited availability. The results show that salts reduce C_{I+N} by the electrostatic screening of the inter and intra-aggregate repulsive interactions. PEG decreases the phase transition concentration through depletion attraction and the effect can be augmented by increasing PEG concentration or the molecular weight of PEG. Ludox shows no effect on C_{I+N} , but promotes the formation of larger birefringent regions. Especially, Ludox-TMA promotes the formation of nematic regions from the center of the droplet, which may be caused by the confinement of SSY within the network of the Ludox-TMA. The addition of SSY significantly reduces the volume fraction of Ludox at gelation. The mechanism requires further investigation. In addition, we have demonstrated that the image analysis technique, GLMC, is a potential method to identify the phase transitions and transition concentrations, and differentiate the phase transition mechanisms induced with PEG. In the future, a more intelligent segmentation algorithm could be developed for accurate counting of the number of bright spots, which will be a strong parameter for differentiating the transition mechanisms. This microfluidic approach can be potentially extended to investigate protein crystallization under various formulation conditions.

6.5 *Reference*

1. McPherson A, Gavira JA (2014) Introduction to protein crystallization. *Acta Crystallogr Sect F, Struct Biol Commun* 70:2
2. Yang MX, Shenoy B, Distler M, Patel R, McGrath M, Pechenov S, Margolin AL (2003) Crystalline monoclonal antibodies for subcutaneous delivery. *Proc Natl Acad Sci U S A* 100:6934–6939
3. Basu SK, Govardhan CP, Jung CW, Margolin AL (2004) Protein crystals for the delivery of biopharmaceuticals. *Expert Opin Biol Ther* 4:301–317
4. Merkle HP, Jen A (2002) A crystal clear solution for insulin delivery. *Nat Biotechnol* 20:789–790
5. Hekmat D (2015) Large-scale crystallization of proteins for purification and formulation. *Bioprocess Biosyst Eng.* 38 (7): 1209-31.
6. Rayment I (2002) Small-Scale Batch Crystallization of Proteins Revisited: An Underutilized Way to Grow Large Protein Crystals. *Structure* 10:147–151
7. Zheng B, Roach LS, Ismagilov RF (2003) Screening of protein crystallization conditions on a microfluidic chip using nanoliter-size droplets. *J Am Chem Soc* 125:11170–11171
8. Chen DL, Gerdtz GJ, Ismagilov RF (2005) Using microfluidics to observe the effect of mixing on nucleation of protein crystals. *J Am Chem Soc* 127:9672–9673
9. Gerdtz CJ, Tereshko V, Yadav MK, Dementieva I, Collart F, Joachimiak A, Stevens RC, Kuhn P, Kossiakoff A, Ismagilov RF (2006) Time-Controlled Microfluidic Seeding in nL-Volume Droplets To Separate Nucleation and Growth Stages of Protein Crystallization. *Angew Chem Int Ed Engl* 45:8156
10. Zheng B, Tice JD, Roach LS, Ismagilov RF (2004) A Droplet-Based, Composite PDMS/Glass Capillary Microfluidic System for Evaluating Protein Crystallization Conditions by Microbatch and Vapor-Diffusion Methods with On-Chip X-Ray Diffraction. *Angew Chem Int Ed Engl* 43:2508
11. Linsenmeier M, Kopp MRG, Stavakis S, de Mello A, Arosio P (2021) Analysis of biomolecular condensates and protein phase separation with microfluidic technology. *Biochim Biophys Acta - Mol Cell Res* 1868:118823

12. Echalié A, Glazer RL, Fülöp V, Geday MA (2004) Assessing crystallization droplets using birefringence. *Acta Crystallogr D Biol Crystallogr* 60:696–702
13. Rubinsztein-Dunlop H, Gibson U, Singer W (2004) Manipulation and growth of birefringent protein crystals in optical tweezers. *Opt Express*, Vol 12, Issue 26, pp 6440–6445
14. Shiyanovskii S V., Lavrentovich OD, Schneider T, Ishikawa T, Smalyukh II, Woolverton CJ, Niehaus GD, Doane KJ (2007) Lyotropic Chromonic Liquid Crystals for Biological Sensing Applications. *Molecular Crystals and Liquid Crystals*. 434(1): 259–587.
15. Shiyanovskii S V., Schneider T, Smalyukh II, Ishikawa T, Niehaus GD, Doane KJ, Woolverton CJ, Lavrentovich OD (2005) Real-time microbe detection based on director distortions around growing immune complexes in lyotropic chromonic liquid crystals. *Phys Rev E - Stat Nonlinear, Soft Matter Phys* 71:020702
16. Lydon J (2004) Chromonic mesophases. *Curr Opin Colloid Interface Sci* 8:480–490
17. Bobrov Y, Cobb C, Lazarev P, Bos P, Bryant D, Wonderly H (2000) 47.4: Lyotropic Thin Film Polarizers. *SID Symp Dig Tech Pap* 31:1102–1105
18. Tam-Chang SW, Helbley J, Carson TD, Seo W, Iverson IK (2006) Template-guided organization of chromonic liquid crystals into micropatterned anisotropic organic solids. *Chem Commun* 0:503–505
19. Nazarenko VG, Boiko OP, Anisimov MI, Kadashchuk AK, Nastishin YA, Golovin AB, Lavrentovich OD (2010) Lyotropic chromonic liquid crystal semiconductors for water-solution processable organic electronics. *Appl Phys Lett* 97:263305
20. Park HS, Lavrentovich OD. (2012) Lyotropic Chromonic Liquid Crystals: Emerging Applications. *chromonic-liquid-crystals-emerging-applications*. Liquid crystals beyond displays: chemistry, physics, and applications. 449–84.
21. Lydon J (1998) Chromonic liquid crystal phases. *Curr Opin Colloid Interface Sci* 3:458–466
22. *Physico-Chemical Principles of Color Chemistry*.
23. Nastishin YA, Liu H, Shiyanovskii S V., Lavrentovich OD, Kostko AF, Anisimov MA (2004) Pretransitional fluctuations in the isotropic phase of a

lyotropic chromonic liquid crystal. *Phys Rev E - Stat Physics, Plasmas, Fluids, Relat Interdiscip Top* 70:9

24. Park HS, Kang SW, Tortora L, Nastishin Y, Finotello D, Kumar S, Lavrentovich OD (2008) Self-Assembly of Lyotropic Chromonic Liquid Crystal Sunset Yellow and Effects of Ionic Additives. *J Phys Chem B* 112:16307–16319
25. Tam-Chang SW, Helbley J, Iverson IK (2008) A Study of the Structural Effects on the Liquid-Crystalline Properties of Ionic Perylenebis(dicarboximide)s Using UV–Vis Spectroscopy, Polarized Light Microscopy, and NMR Spectroscopy. *Langmuir* 24:2133–2139
26. Yu LJ, Saupe A (1982) Deuteron Resonance of D₂O of Nematic Disodium Cromoglycate-Water Systems. *Molecular Crystals and Liquid Crystals*. 80 (1): 129-34
27. Demus D, Goodby J, Gray GW, Spiess H -W., Vill V (1998) Handbook of Liquid Crystals. Fundamentals High Regular Weight Liquid Crystal. 207-69.
28. Park HS, Kang SW, Tortora L, Kumar S, Lavrentovich OD (2011) Condensation of Self-Assembled Lyotropic Chromonic Liquid Crystal Sunset Yellow in Aqueous Solutions Crowded with Polyethylene Glycol and Doped with Salt. *Langmuir* 27:4164–4175
29. Kostko AF, Cipriano BH, Pinchuk OA, Ziserman L, Anisimov MA, Danino D, Raghavan SR (2005) Salt Effects on the Phase Behavior, Structure, and Rheology of Chromonic Liquid Crystals. *J Phys Chem B* 109:19126–19133
30. Tortora L, Park HS, Kang SW, Savaryn V, Hong SH, Kaznatcheev K, Finotello D, Sprunt S, Kumar S, Lavrentovich OD (2010) Self-assembly , condensation, and order in aqueous lyotropic chromonic liquid crystals crowded with additives. *Soft Matter* 6:4157–4167
31. Simon KA, Sejwal P, Gerecht RB, Luk YY (2007) Water-in-water emulsions stabilized by non-amphiphilic interactions: Polymer-dispersed lyotropic liquid crystals. *Langmuir* 23:1453–1458
32. Horowitz VR, Janowitz LA, Modic AL, Heiney PA, Collings PJ (2005) Aggregation behavior and chromonic liquid crystal properties of an anionic monoazo dye. *Phys Rev E - Stat Nonlinear, Soft Matter Phys* 72:041710
33. Edwards DJ, Jones JW, Lozman O, Ormerod AP, Sinyureva M, Tiddy GJT (2008) Chromonic Liquid Crystal Formation by Edicol Sunset Yellow†. *J Phys Chem B* 112:14628–14636

34. Joshi L, Kang SW, Agra-Kooijman DM, Kumar S (2009) Concentration, temperature, and pH dependence of sunset-yellow aggregates in aqueous solutions: An x-ray investigation. *Phys Rev E - Stat Nonlinear, Soft Matter Phys* 80:041703
35. Eccher J, Sampaio AR, Viscovini RC, Conte G, Westphal E, Gallardo H, Bechtold IH (2010) Image processing as a tool for phase transitions identification. *J Mol Liq* 153:162–166
36. Sastry SS, Kumar S, Kumari TV, Mallika K, Sankara Rao BG, Tiong HS (2012) Liquid crystal parameters through image analysis. *Liquid Crystals*. 39(12): 1527-37.
37. Farinha A, Flores FC, Sampaio AR, Kimura NM, Freire FCM (2022) Phase transition detection in liquid crystal analysis by mathematical morphology. *J Mol Liq* 345:117015
38. Sastry SS, Rao BGS, Mahalakshmi KB, Mallika K, Rao CN, Tiong HS (2012) Image Analysis Studies for Phase Transitions of Ferroelectric Liquid Crystals. *ISRN Condens Matter Phys* 2012:1–8
39. Bleier BJ, Anna SL, Walker LM (2018) Microfluidic Droplet-Based Tool to Determine Phase Behavior of a Fluid System with High Composition Resolution. *J Phys Chem B* 122:4067–4076
40. Sunset Yellow FCF Dye content 90 2783-94-0. <https://www.sigmaaldrich.com/US/en/product/aldrich/465224>. Accessed 29 Mar 2022
41. Prasad Sk, Nair GG, Hegde G, Jayalakshmi V. (2007) Evidence of Wormlike Micellar Behavior in Chromonic Liquid Crystals: Rheological, X-ray, and Dielectric Studies. *The Journal of Physical Chemistry B*. 111(33): 9741-6.
42. Albregtsen F (2008) Statistical Texture Measures Computed from Gray Level Cooccurrence Matrices.
43. Elshinawy MY, Badawy AHA, Abdelmageed WW, Chouikha MF (2011) Detection of normal mammograms based on breast tissue density using GLCM features. *Proc 8th IASTED Int Conf Biomed Eng Biomed* 2011 370–377
44. Doi M (1981) Molecular dynamics and rheological properties of concentrated solutions of rodlike polymers in isotropic and liquid crystalline phases. *J Polym Sci Polym Phys Ed* 19:229–243
45. Paul C.Hiemenz TPL (2007) *Polymer Chemistry* (2nd Edition). 608

46. Kulkarni S, Thareja P (2017) Suspensions of titania nanoparticle networks in nematic liquid crystals: rheology and microstructure. 56(10): 825-40.
47. Landman J, Paineau E, Davidson P, Bihannic I, Michot LJ, Philippe AM, Petukhov A V., Lekkerkerker HNW (2014) Effects of Added Silica Nanoparticles on the Nematic Liquid Crystal Phase Formation in Beidellite Suspensions. J Phys Chem B 118:4913–4919
48. Marlow JB, McCoy TM, Ho CQ, De Campo L, Knott R, Bell TDM, Tabor RF (2019) Tuning the structure, thermal stability and rheological properties of liquid crystal phases via the addition of silica nanoparticles. Phys Chem Chem Phys 21:25649–25657

Chapter 7: Quantification of phase separation of a globular protein induced by polyethylene glycol

7.1 *Introduction*

Subcutaneous injection requires therapeutic proteins to be formulated at high concentrations (typically > 100 mg/mL). However, it is challenging to achieve such high concentrations and remain stable against degradation. [1] Ultrafiltration using tangential flow filtration (TFF) is the most common technique to concentrate the therapeutic proteins solutions. However, the elevated concentration results in a drastic increase in viscosity, which can induce pressure increase and membrane fouling during ultrafiltration. [2, 3] High protein concentrations also enhance the intermolecular interactions, which promote protein aggregation and cause physical protein instabilities. [4] Lyophilization is another approach to generate high concentration proteins with enhanced conformational stability. However, long reconstitution time limits the application of lyophilization formulations, which also requires additional steps and costs to remove salts and detergents. [5, 6] Protein solutions concentrated by chemical precipitation can lead to protein denaturation and provide low recovery. [7]

Liquid-liquid phase separation (LLPS) has been proposed as a potential approach to concentrate protein solutions, generating a protein-poor upper layer and protein-rich dense layer. [8] However, the increased attractive protein-protein interactions (PPI) in the dense phase may promote protein aggregation and induce undesired instability. Studies have been conducted to optimize the formulation conditions, such as pH, excipients, and temperature to enhance the stability of

concentrated protein solutions produced from LLPS. [8–11] In addition, LLPS has been widely applied to study the solubility and stability of protein solutions under various formulation conditions. [12–14] Therefore, being able to accurately quantify the phase separation of protein solutions as a function of formulation factors is essential for the development of therapeutic proteins. However, the limited availability of the therapeutic proteins hinders the effective characterization of the phase transitions.

Droplet-based microfluidic technologies have been developed for analyzing the phase separation of biomolecular systems due to their advantages of simple fabrication, small sample volume, rapid sample mixing, compartmentalization of samples, long-time storage and on-chip detection [15, 16] The microfluidic device applied in this work has been shown to be able to quantify LLPS of complex aqueous mixtures of organics and salts with a small sample volume and high compositional resolution. [17] In addition, polyethylene glycol (PEG) is a common precipitating agent for proteins. PEG-induced LLPS has been applied to determine the colloidal stability [13, 18] and conduct solubility screening [19–21] of protein solutions.

Therefore, in this chapter, we apply the droplet-based microfluidic device to quantify the phase separation of a globular protein, bovine serum albumin (BSA), induced by the presence of PEG. Turbidity observed in the droplet is used as the sensing method to signify the onset of phase separation. The effects of molecular weight and concentration of PEG on the phase separation are systematically investigated. The discrepancy between the microfluidic and macroscopic results

suggests that the observed turbidity may not be due to LLPS but to PEG-induced precipitation, which is kinetically controlled and depends on the time- and length-scale. Overall, the outcome of this chapter suggests that when applying the microfluidic device to quantify processes that are kinetically controlled, the effects of time and length scales need to be considered.

7.2 *Materials and Methods*

7.2.1 *Materials*

Bovine Serum Albumin (BSA) is purchased from Sigma-Aldrich (Catalog No.: A7030). Polyethylene glycol (PEG) with molecular weight of 600 g/mol, 1.5 kg/mol and 4 kg/mol are obtained from Sigma-Aldrich (St. Louis, MO). 100 kg/mol PEG is obtained from Polysciences Inc. (Warminster, PA). Stock solutions of BSA and PEG are made by mixing a known mass of solute with the deionized water (18.2 M Ω ·cm) at a known volume in a volumetric flask and are allowed to dissolve overnight. Then the stock solutions are mixed in different mass ratios to provide sample solutions with various PEG/BSA compositions. The mass ratio of PEG to BSA is defined as ξ . For macroscopic experiments, stock solutions of BSA and PEG with various molecular weights are prepared at high concentrations. Then the stock solutions are mixed to reach target concentrations. Samples are gently mixed on the roller at room temperature ($22 \pm 1^\circ\text{C}$) for 20 min before observations are taken.

7.2.2 *Methods*

The phase transition of BSA induced by PEG is quantified using the droplet-based microfluidic device. Chapter 2 discusses the details for device fabrication and droplet generation. 2wt% span 80 is added to the mineral oil to provide proper wetting and reduce interfacial tension for droplet production. 40 aqueous droplets containing dilute and well-mixed sample solutions are generated in the microfluidic channel and are surrounded by mineral oil. The dehydration process of all 40 droplets is monitored under a Nikon Ti-U microscope under bright field conditions (10 \times mag, 0.65 $\mu\text{m}/\text{pixel}$) by taking sequential images at every 2 min. At each time point, the entire device is automatically scanned in a zig-zag path across the device (Figure 2.1), taking an image of every droplet. The droplet diameter is analyzed using the image processing method developed in MATLAB. The diameter is used to calculate the droplet volume based on Eqn. (2.1) in Chapter 2, which is then converted to the concentration of solute based on mass balance. Details of the droplet dehydration process and volume calculation can be found in Chapter 2. The increasing solute concentration is accurately tracked inside each droplet. The complete dehydration takes about 18 – 24 h under the current lab conditions, minimizing concentration gradient inside the droplet. The dehydration process is conducted at room temperature ($22 \pm 1^\circ\text{C}$.)

7.3 Results

Figure 7.1 shows the dehydration process of a typical droplet containing dilute BSA and 4 kg/mol PEG solution observed under the bright field microscope in the microfluidic device as an example. Images are taken at every 2 min and the entire dehydration process takes approximately 18 - 24 h under the current lab conditions. Images in Figure 7.1 are at various time points for the same droplet, illustrating the droplet shrinking and the evolution of optical change. Initially, the

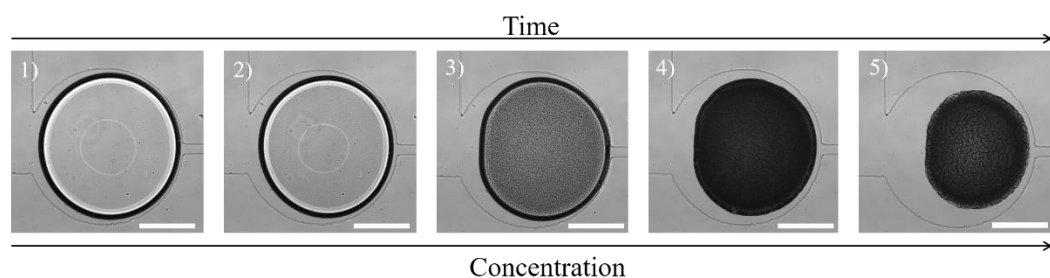


Figure 7.1 A typical dehydration process of a droplet containing dilute BSA with PEG obtained through the bright field microscope in the microfluidic device. White bars are equivalent to 200 μm . The droplet shrinks in size and the concentration of solute increases. The first observation of the occurrence of turbidity (image 2) indicates the onset of transition. Turbidity increases through the shrinking process.

droplet contains dilute BSA/ PEG solution and appears clear (image 1). As water partitions through the oil phase and then the PDMS device, the droplet decreases in size, and the concentration of both solutes increases. The first observation of the optical change is seen as turbidity inside the droplet as image 2. Turbidity increases as solutes are concentrated in the shrinking droplet (image 3-4). When the droplet deviates from the pancake shape, indicated by the loss of circular projection, the volume and concentration cannot be determined accurately. Image 5 shows the final state of the droplet, which is completely dried out.

To determine the BSA concentration at which the optical change is first observed, the pixel intensities of the droplet center, I_{center} , and the channel,

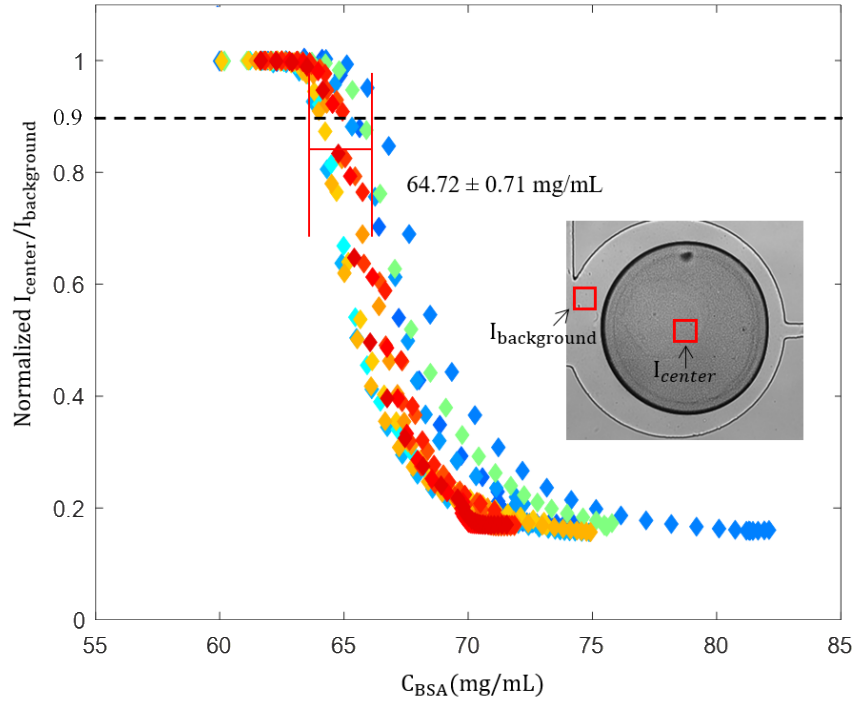


Figure 7.2 Normalized ratio of I_{center} to $I_{background}$ as a function of BSA concentration for BSA with 1500 g/mol PEG at $\xi = 2.1$. Each color represents the dehydration result of one good droplet out of 40. The phase separation concentration for each droplet is defined as the BSA concentration at which the intensity ratio equals 0.9, obtained by linear interpolation of the continuous data. The phase separation concentration is determined as 64.72 ± 0.71 mg/mL by averaging the results of all good droplets.

$I_{background}$, are analyzed, illustrated by the inset in Figure 7.2. Figure 7.2 shows

the ratio of I_{center} to $I_{background}$, normalized by the ratio of the first image

$$\left(\frac{I_{center(i)}}{I_{background(i)}} / \frac{I_{center(1)}}{I_{background(1)}} \right), \text{ as a function of BSA concentration for BSA with}$$

1500 g/mol PEG as an example. The curves show the results for all droplets

considered acceptable out of the 40 traps. Unacceptable droplets are either formed

during the droplet generation or have bad wetting sticking to the channel surface

during the shrinking process. Each color represents a single dehydration experiment

of one droplet. The BSA concentration at which the ratio of I_{center} to $I_{background}$ equals 0.9 is defined as the concentration at which the optical change is first observed, which is linearly interpolated from the continuous data points. The transition concentration is determined as 64.72 ± 0.71 mg/mL by averaging the results over all good droplets for the BSA and PEG system shown in Figure 7.2. Similar results and variation seen for other systems.

Figure 7.3 a shows the phase diagram of BSA and 4 kg/mol PEG measured in the microfluidic device. Each dashed line indicates one dehydration experiment involving 40 droplets of a constant mass ratio of PEG to BSA, ξ . The squares represent the initial solute concentrations. As the droplet shrinks, the concentrations of both BSA and PEG increase, indicated by moving along the dashed line. The circles represent the solute concentrations at which the optical change is first observed and the error bar shows the uncertainty over all good droplets. The transition concentration of BSA decreases as more PEG is added into the system except for $\xi = 0.4$, which initial concentrations are higher than that of other values of ξ . The initial concentrations of each dehydration experiment is chosen so that the transition happens at the point where the droplet diameter is larger than the height of the channel, 100 μm , to maintain the pancake shape volume valid, and also to ensure that the dehydration time required to reach the transition is less than 24 h for experimental efficiency. The initial concentrations happen to decrease with increasing PEG concentration, except for $\xi = 0.4$. The different trend of dependence on PEG concentration observed at $\xi = 0.4$ suggests that the initial solute concentrations could have an impact on the transition concentration and will be

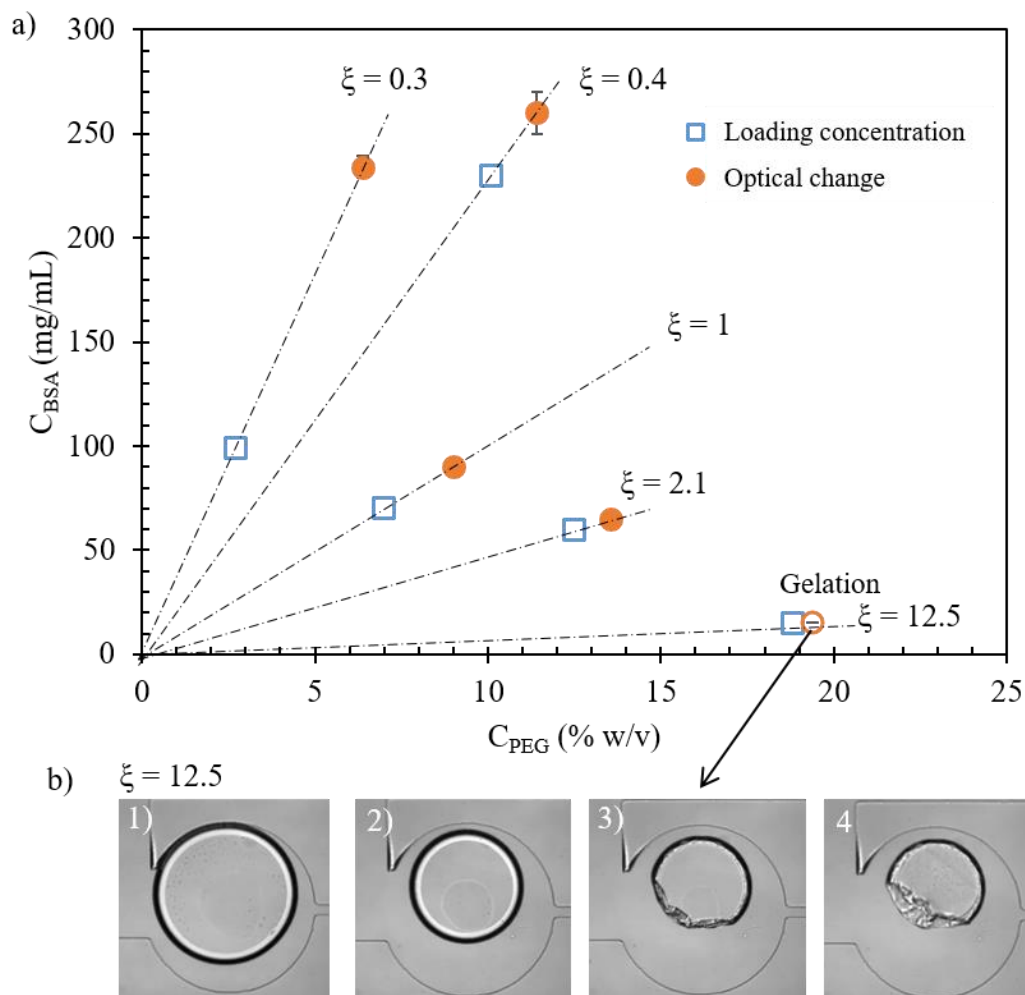


Figure 7.3 a) Phase diagram for BSA and 4 kg/mol PEG generated via the microfluidic experiments. Each dashed line represents one dehydration experiment with a constant mass ratio of BSA to PEG, defined as ξ . The squares and circles represent the loading solute concentrations and the concentrations at which optical change occurs. At $\xi = 12.5$, the droplet gelled (open circle). b) Dehydration sequence of a droplet at $\xi = 12.5$. The droplet is gelled (image 3) and no optical change is observed throughout the dehydration process.

investigated in the later section. At high PEG concentration, $\xi = 12.5$, the mixture of BSA and PEG gelled at approximately 30 min after loading into the device, illustrated by the wrinkled droplet surface shown in Figure 7.3b image 3. No turbidity is observed in the droplet throughout the dehydration process as shown in Figure 7.3b.

Figure 7.4 shows the BSA concentration as a function of the molecular weight of PEG at $\xi = 2.1$. The squares and circles represent the initial and transition BSA concentrations, respectively. The BSA concentration at optical change (transition concentration) shows no dependence on the molecular weight of PEG, except for 100 kg/mol PEG, which has a much lower initial concentration. The

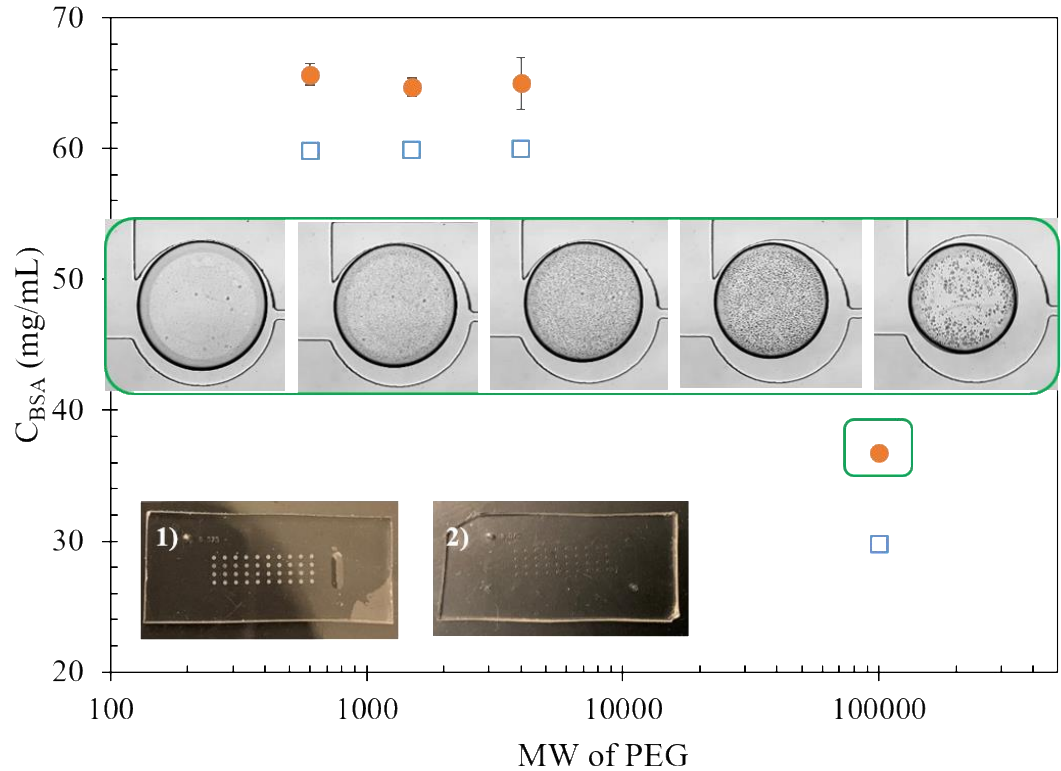


Figure 7.4 BSA concentration as a function of molecular weight (MW) of PEG at $\xi = 2.1$. The inset shows the dehydration sequence of a typical droplet containing BSA with 100 kg/mol PEG. Small droplets occur and coalesce into larger droplets during the dehydration process. Images 1 and 2 show the microfluidic device for PEG of MWs other than 100 kg/mol and 100 kg/mol PEG, respectively.

reason to start with a decreased initial solute concentration for 100 g/mol PEG is that at $\xi = 2.1$ with 60 mg/mL of BSA, the concentration of 100 kg/mol PEG needs to be 28 mg/mL (~27wt%), which exceeds its solubility and forms gel. Figure 7.4 suggests that the initial solute concentrations and the molecular weight could impact the phase transition concentration. In addition, the transition mechanism for

100 kg/mol PEG is different from the other three molecular weights. Instead of the appearance of turbidity similar to Figure 7.1, a large number of small droplets occur inside the microfluidic droplet and coalesce into larger sizes as droplet shrinking, which is illustrated by the inset in Figure 7.4. The droplets for the other three molecular weights appear to be opalescent after transition when observed by the eyes (image 1 Figure 7.4), while the droplets for 100 kg/mol PEG are relatively clear (image 2 Figure 7.4), suggesting a different mechanism. The results indicate that the initial solute concentration could have impacts on both the transition concentration and the mechanism of the transition.

Figure 7.5 illustrates the BSA concentration at the optical change (or transition), $C_{t,BSA}$, as a function of the initial BSA concentration, $C_{i,BSA}$ for BSA with 1.5 kg/mol PEG at $\xi = 2.1$. $C_{t,BSA}$ increases with $C_{i,BSA}$. This is consistent with the previous observations that for 4 kg/mol PEG, $\xi = 0.4$, which has the largest

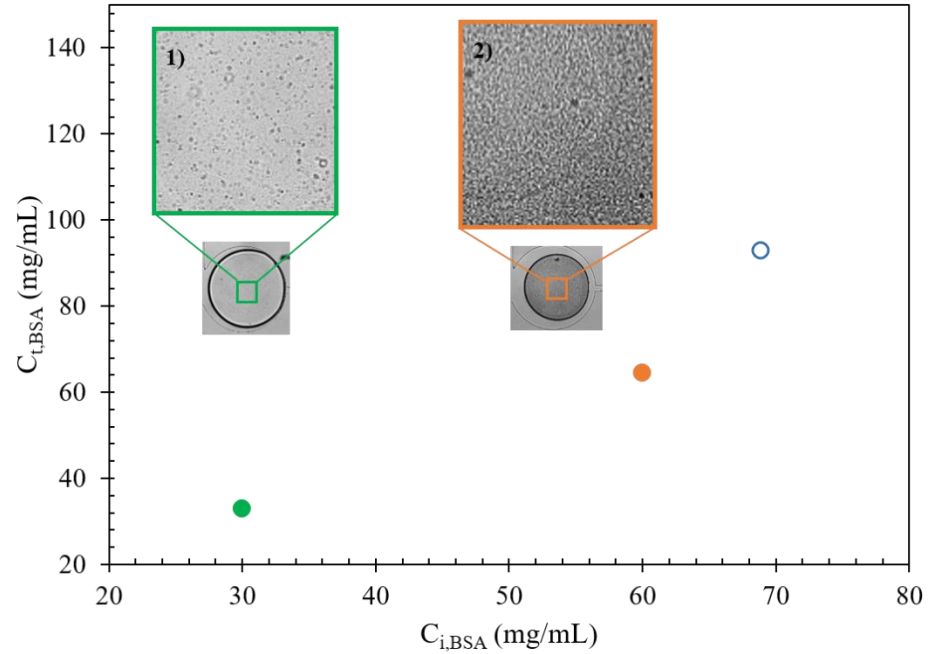


Figure 7.5 $C_{t,BSA}$ as a function of $C_{i,BSA}$ for BSA with 1.5 kg/mol PEG at $\xi = 2.1$. Images 1 and 2 show the frame where the optical change is first observed.

$C_{i,BSA}$, shows the highest $C_{t,BSA}$. Also 100 k/mol PEG, which has the lowest $C_{i,BSA}$, exhibits the lowest $C_{t,BSA}$ compared to the other three MWs. In addition, $C_{i,BSA}$ shows the impact on the phase transition mechanism. At $C_{i,BSA} = 30$ mg/mL, less turbidity is observed as shown by the occurrence of the small droplets (Figure 7.5 image 1) similar to that seen for 100 kg/mol PEG in the inset of Figure 7.4, which also starts with the same value of $C_{i,BSA}$. As $C_{i,BSA}$ increases to 60 mg/mL, the droplets appear to be turbid at the transition (Figure 7.5 image 2), which is similar to that observed in Figure 7.1. At $C_{i,BSA} = 69$ mg/mL, no optical change is observed up to nearly 95 mg/mL, indicated by the open circle. The PEG concentration is correlated with BSA concentration by ξ , therefore the initial solute concentration is linearly depends on the BSA concentration. Overall, the initial solute concentration is an essential parameter that affects both the transition concentration and mechanism of the BSA and PEG systems. Two distinct transition mechanisms are observed: one involves the dramatic increase in the turbidity, and the other one shows the occurrence of small droplets and coalescence during the concentrating process.

The microfluidic results are compared with macroscopic experiments as shown in Figure 7.6, in which BSA and 1.5 kg/mol PEG at $\xi = 2.1$ are shown as an example. The circle indicates the transition concentration determined in the microfluidic device from Figure 7.4. The triangles denote the compositions of macroscopic samples with solute concentrations below, equal, and above the microfluidic results. No turbidity is observed in all three samples, illustrated by the clear single-phase solution in the glass vial shown in the inset. The same

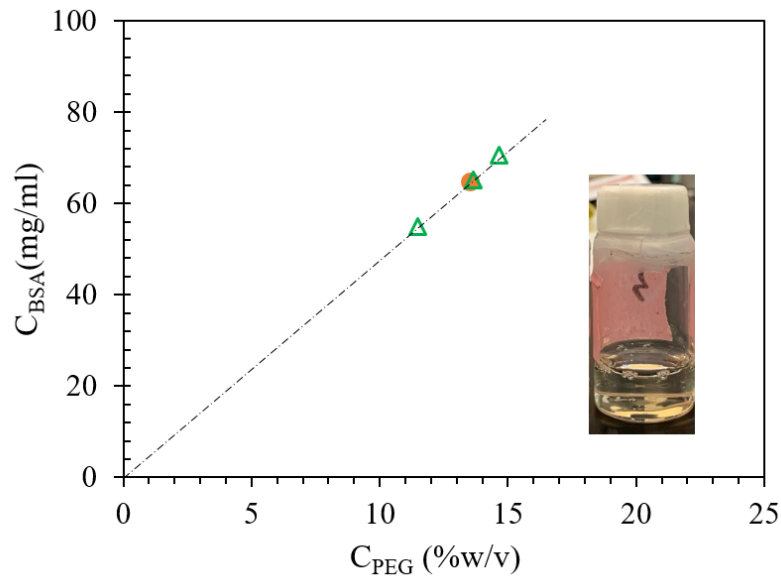


Figure 7.6 Comparisons between microfluidic results (circle) and macroscopic experiment (triangles) for BSA with 1.5 kg/mol PEG at $\xi = 2.1$ as an example. All three macroscopic samples show clear single phase solutions as illustrated by the inset.

inconsistency between microfluidic and macroscopic results is observed for BSA with PEG of other molecular weights and different values of ξ , that neither phase separation nor opalescence is observed in the macroscopic samples with solute concentrations equal to or higher than the transition concentration determined by the microfluidic device. Finally, even though a different transition mechanism is observed for 100 kg/mol in the microfluidic droplets, macroscopic samples exhibit a single-phase solution. The macroscopic samples maintain as a single-phase even after a week stored at room temperature.

7.4 Discussion

Two distinct transition mechanisms are observed in the microfluidic shrinking droplets. One mechanism involves a drastic increase in turbidity. The other mechanism shows the occurrence of small droplets, which coalesce as water

evaporates. Studies have been conducted to quantify the LLPS of protein solutions in the droplet-based microfluidic devices, where two visually different liquid phases are observed in the droplet at phase separation. The inner phase involves small droplets with clear interfaces, which coalesce as water evaporates, and is surrounded by the outer phase. [16, 22] This is similar to the second mechanism observed in this work. It is known that PEG also induces protein precipitation, where the solution appears to be opalescent. [21, 23, 24] This is similar to the first mechanism observed in this work. The droplets after transition are visually opalescent (Figure 7.4 image 1). Therefore, we propose that the occurrence of turbidity inside the droplets indicates the onset of PEG-induced protein precipitation and the appearance of small droplets with clear interfaces signifies the LLPS.

Protein precipitation is a kinetically controlled process, which means that the time scale and the length scale have considerable effects on the measured results, thus may contribute to the discrepancies between the microfluidic and macroscopic results observed in this work. The dehydration rate of the microfluidic droplet is considered to be slow to ensure homogeneity of the sample solution. However, it might not be slow enough to achieve thermodynamic equilibrium. The macroscopic samples are allowed to mix for 20 min. This incubation time may cause variation in the protein precipitation. In addition, the length scale of the microfluidic droplet is approximately two orders of magnitude smaller than that of the macroscopic glass vial. The turbidity observed in the micrometer droplet may not be detected by macroscopic samples. Toth *et al.* demonstrated that the initial protein concentration

and the type of PEG show impact on the protein precipitation [25], which is also observed in this work. Finally, the oil-water interface of the microfluidic shrinking droplet could cause depletion of PEG to the interface and may affect the calculated concentration in the droplet. The discrepancies observed for the LLPS require further investigation.

7.5 Conclusion

In this chapter, the droplet-based microfluidic device is applied to quantify the phase separation of BSA induced by PEG. The initial solute concentrations have been shown to have considerable effects on the transition concentration and the transition mechanisms. Two distinct mechanisms are observed: one involves a drastic increase in turbidity, which is similar to protein precipitation. The other one shows the appearance of small droplets with clear interfaces, which is consistent with LLPS. The discrepancies between the microfluidic and macroscopic results for BSA and PEG systems of protein precipitation may result from the difference in the time and length scales. The inconsistency for the LLPS systems requires further investigation. In addition, this chapter presents the application limitation of the developed microfluidic device. When using this novel tool to quantify processes that are time and length scale sensitive, extreme care should be taken.

7.6 *Reference*

1. Shire SJ, Shahrokh Z, Liu J (2004) Challenges in the development of high protein concentration formulations. *J Pharm Sci* 93:1390–1402
2. Holstein M, Hung J, Feroz H, Ranjan S, Du C, Ghose S, Li ZJ (2020) Strategies for high-concentration drug substance manufacturing to facilitate subcutaneous administration: A review. *Biotechnol Bioeng* 117:3591–3606
3. Arakawa T, Ejima D, Akuta T (2017) Protein aggregation under high concentration/density state during chromatographic and ultrafiltration processes. *Int J Biol Macromol* 95:1153–1158
4. Shire SJ (2009) Formulation and manufacturability of biologics. *Curr Opin Biotechnol* 20:708–714
5. Cao W, Krishnan S, Ricci MS pee., Shih LY, Liu D, Gu JH u., Jameel F (2013) Rational design of lyophilized high concentration protein formulations-mitigating the challenge of slow reconstitution with multidisciplinary strategies. *Eur J Pharm Biopharm* 85:287–293
6. Sheen H, Ali-Khan Z (2005) Protein sample concentration by repeated loading onto SDS-PAGE. *Anal Biochem* 343:338–340
7. Virgen-Ortíz JJ, Ibarra-Junquera V, Osuna-Castro JA, Escalante-Minakata P, Mancilla-Margalli NA, Ornelas-Paz JDJ (2012) Method to concentrate protein solutions based on dialysis-freezing-centrifugation: enzyme applications. *Anal Biochem* 426:4–12
8. Bramham JE, Davies SA, Podmore A, Golovanov AP (2021) Stability of a high-concentration monoclonal antibody solution produced by liquid-liquid phase separation. *InMAbs*. (Vol. 13, No.1, p. 1940666).
9. Bye JW, Platts L, Falconer RJ (2014) Biopharmaceutical liquid formulation: a review of the science of protein stability and solubility in aqueous environments. *Biotechnol Lett* 36:869–875
10. Kheddo P, Tracka M, Armer J, Dearman RJ, Uddin S, Van Der Walle CF, Golovanov AP (2014) The effect of arginine glutamate on the stability of monoclonal antibodies in solution. *Int J Pharm* 473:126
11. Johnson HR, Lenhoff AM (2013) Characterization and suitability of therapeutic antibody dense phases for subcutaneous delivery. *Mol Pharm* 10:3582–3591
12. Raut AS, Kalonia DS (2016) Pharmaceutical Perspective on Opalescence

and Liquid-Liquid Phase Separation in Protein Solutions. *Mol Pharm* 13:1431–1444

13. Wang Y, Latypov RF, Lomakin A, Meyer JA, Kerwin BA, Vunnum S, Benedek GB (2014) Quantitative evaluation of colloidal stability of antibody solutions using PEG-induced liquid-liquid phase separation. *Mol Pharm* 11:1391–1402
14. Jion AI, Goh LT, Oh SKW (2006) Crystallization of IgG1 by mapping its liquid-liquid phase separation curves. *Biotechnol Bioeng* 95:911–918
15. Linsenmeier M, Kopp MRG, Stavrakis S, de Mello A, Arosio P (2021) Analysis of biomolecular condensates and protein phase separation with microfluidic technology. *Biochim Biophys Acta - Mol Cell Res* 1868:118823
16. Kopp MRG, Linsenmeier M, Hettich B, Prantl S, Stavrakis S, Leroux JC, Arosio P (2020) Microfluidic Shrinking Droplet Concentrator for Analyte Detection and Phase Separation of Protein Solutions. *Anal Chem* 92:5803–5812
17. Bleier BJ, Anna SL, Walker LM (2018) Microfluidic Droplet-Based Tool to Determine Phase Behavior of a Fluid System with High Composition Resolution. *J Phys Chem B* 122:4067–4076
18. Wang Y, Lomakin A, Latypov RF, Laubach JP, Hideshima T, Richardson PG, Munshi NC, Anderson KC, Benedek GB (2013) Phase transitions in human IgG solutions. *J Chem Phys* 139:121904
19. Gibson TJ, Mccarty K, Mcfadyen IJ, Cash E, Dalmonte P, Hinds KD, Dinerman AA, Alvarez JC, Volkin DB (2011) Application of a high-throughput screening procedure with PEG-induced precipitation to compare relative protein solubility during formulation development with IgG1 monoclonal antibodies. *J Pharm Sci* 100:1009–1021
20. Li L, Kantor A, Warne N (2013) Application of a PEG precipitation method for solubility screening: A tool for developing high protein concentration formulations. *Protein Sci* 22:1118
21. Scannell MJ, Hyatt MW, Budyak IL, Woldeyes MA, Wang Y (2021) Revisit PEG-Induced Precipitation Assay for Protein Solubility Assessment of Monoclonal Antibody Formulations. *Pharm Res* 38:1947–1960
22. Bremer A, Mittag T, Heymann M (2020) Microfluidic characterization of macromolecular liquid–liquid phase separation. *Lab Chip* 20:4225–4234

23. Oeller M, Sormanni P, Vendruscolo M (2021) An open-source automated PEG precipitation assay to measure the relative solubility of proteins with low material requirement. *Sci Reports* 2021 111 11:1–10
24. Hofmann M, Winzer M, Weber C, Gieseler H (2018) Limitations of polyethylene glycol-induced precipitation as predictive tool for protein solubility during formulation development. *J Pharm Pharmacol* 70:648–654
25. Tóth J, Kardos-Fodor A, Halász-Péterfi S, Gyenis J. The effects of the operational parameters on the characteristics of protein microparticles. In *The 2006 Spring National Meeting* 2006 Apr 24.

Chapter 8: Conclusions

In this thesis, the droplet-based microfluidic device is incorporated with various sensing methods to investigate the physical properties of high concentration protein solutions. Droplets containing dilute sample solutions are generated in the device and dehydrate with time while being continuously monitored. Solutes are concentrated in the droplets as water evaporates. Small sample volumes are required to generate data with high compositional resolution, covering a wide range of parameter space. The results provide a novel tool to better characterize the formulations for protein candidates and provide complimentary work for computational approaches.

In Chapters 3-5, the droplet-based microfluidic device is combined with multiple particle tracking microrheology (MPT) to quantify the viscosity of protein solutions as concentration increases. In Chapter 3, the proof of concept is demonstrated by quantifying the viscosity-concentration curve for two globular proteins. Only a few microliters of sample is needed to cover nearly a decade increase in concentration (up to 400 mg/mL) and several orders of magnitude increase in viscosity, providing data with high compositional resolution. The measured results show agreement with macroscopic experiments and are consistent with the classical theoretical model.

In Chapter 4, the microfluidic device is expanded to quantify the viscosity of protein solutions in a multi-component system. The viscosity of a globular protein is quantified as a function of ionic strength and pH besides the protein concentration. The results demonstrate that the microfluidic approach is able to

provide high compositional resolution data covering a multi-parameter space. The continuous nature of data is able to provide operating regimes for different formulation requirements and has the potential to provide complimentary work for computational studies. The microfluidic tool can better screen and optimize the formulation conditions and provide insights into the intermolecular mechanisms of concentrated protein solutions.

In Chapter 5, the effects of multiple excipients on the viscosity of a concentrated antibody solution are investigated under various solution conditions using the microfluidic device. The effectiveness of both excipients depends on the solution conditions. Synergistic effects between the two excipients are observed. The results show the potential of the developed microfluidic approach to test the novel excipients and assess the impacts of multiple excipients, providing guidance for developing biopharmaceutical formulations.

In Chapter 6, the droplet-based microfluidic device is implemented with polarizing microscopy, and birefringence is applied as the sensing method to characterize the phase transitions of a lyotropic liquid crystal. The variations in the textural structure of the birefringent domains signify the phase transitions, which are quantified with significantly improved compositional resolution and are consistent with the macroscopic and literature results. The effects of various additives on the phase transitions are investigated, providing insights into the underlying mechanism of self-assembly of the lyotropic liquid crystal. In addition, the results demonstrate that the standard image processing technique can be applied to identify the phase transitions automatically. This microfluidic approach with

optical polarization can be potentially applied to characterize the crystallization of the protein solutions under various formulation conditions.

In Chapter 7, turbidity is combined with the droplet-based microfluidic device as the sensing method to investigate the phase separation of a globular protein induced by polyethylene glycol. Phase separation is investigated at different PEG/protein ratios, initial concentrations, and molecular weights of PEG. Two phase separation mechanisms are observed. The results indicate that the loading concentration of solutes could have an impact on the phase separation concentration and mechanism. Inconsistency between the microfluidic and macroscopic approaches and the optical observation suggest that protein precipitation may be observed instead of the liquid-liquid phase separation. The inherent dehydration time scale and the length scale of the microfluidic device may cause application limitations on the kinetically controlled processes.

In conclusion, this thesis demonstrates a novel droplet-based microfluidic approach incorporated with various sensing methods to study the physical properties of concentrated protein solutions under various formulation conditions with small sample volumes and high compositional resolution. This approach can be applied to screen the candidate formulations during the early development stage and help the formulation scientists to design and optimize the formulation conditions for high concentration protein solutions to achieve desired physical properties. The high compositional resolution data has the potential to provide complimentary work for computational modeling of viscosity prediction.